Comprehensive Vibration Assessment Program for the Reactor Vessel Internals

Revision 0

Non-Proprietary

November 2014

Copyright ⓒ 2014

Korea Electric Power Corporation &

Korea Hydro & Nuclear Power Co., Ltd

All Rights Reserved

REVISION HISTORY

Revision	Date	Page	Description
0	November 2014	All	First Issue

This document was prepared for the design certification application to the U.S. Nuclear Regulatory Commission and contains technological information that constitutes intellectual property.
Copying, using, or distributing the information in this document in whole or in part is permitted only by the U.S. Nuclear Regulatory Commission and its contractors for the purpose of reviewing design certification application materials. Other uses are strictly prohibited without the written permission of Korea Electric Power Corporation and Korea Hydro & Nuclear Power Co., Ltd.

ABSTRACT

The Advanced Power Reactor 1400 (APR1400) reactor vessel internals (RVI) are designated as non-prototype Category I, per Regulatory Guide 1.20 (Reference 1), with Palo Verde Unit 1, Westinghouse System 80 RVI as the valid prototype. The Palo Verde Unit 1 RVI and the APR1400 RVI are substantially the same with regard to arrangement, design, size, and operating conditions.

The comprehensive vibration assessment program (CVAP) for the APR1400 RVI consists of analysis program and inspection program. The vibration analysis provides the theoretical evidence of the structural integrity of the RVI, serves as the basis for the inspection program, and is divided into three parts: calculation of hydraulic loads or forcing functions, analysis of the structures to determine their modal characteristics, and calculation of the responses. This report presents the analysis methodologies for calculating the dynamic responses of the RVI to the flow-induced hydraulic loads. The results of the analysis for the flow-induced loads show that the maximum predicted stresses are below the alternating stress intensities causing fatigue failure.

The inspection program is implemented in lieu of vibration measurement program for the APR1400 RVI. The inspection program consists of pre-hot functional inspection and post-hot functional inspection of the RVI. The duration of the hot functional test is established to provide reasonable assurance that the 10^6 cycles of vibration occur before the post-hot functional inspection. A detailed inspection is performed for major bearing surfaces, contact surfaces, welds, and maximum stress locations identified in the analysis program. The visual inspections are compared before and after pre-core tests to provide reasonable assurance that there is no sign of abnormal wear or contact for any of the RVI.

Through the CVAP, the structural integrity of the APR1400 RVI is verified for flow-induced vibration prior to commercial operation.

The vibration assessments of the steam generator internals and the piping systems attached to the reactor coolant system are provided in Appendix A and Appendix B, respectively.

TABLE OF CONTENTS

1 INTRODUCTION 1

2 DESCRIPTION AND CLASSIFICATION OF THE REACTOR VESSEL INTERNALS 2

2.1 General Arrangement and Flow Conditions 2

2.2 Classification of the Reactor Vessel Internals in Accordance with the Comprehensive Vibration Assessment Program 8

2.3 Summary of the Valid Prototype CVAP 16

3 VIBRATION AND STRESS ANALYSIS PROGRAM 18

3.1 General Methodology 18

3.1.1 Hydraulic Loads 18

3.1.2 Structural Analysis 19

3.2 Calculation of the Forcing Function 21

3.2.1 Analytical Method 21

3.2.2 Core Support Barrel 21

3.2.3 Upper Guide Structure 28

3.2.4 Lower Support Structure 36

3.2.5 In-Core Instrument Nozzle Assembly 39

3.2.6 Core Shroud 44

3.2.7 Inner Barrel Assembly 47

3.3 Calculation of the Structural Response 50

3.3.1 Core Support Barrel 51

3.3.2 Upper Guide Structure 57

3.3.3 Tube Bank Assembly 60

3.3.4 Lower Support Structure 64

3.3.5 In-Core Instrument Nozzle Assembly 68

3.3.6 Core Shroud 72

3.3.7 Inner Barrel Assembly 76

3.4 Evaluation of the Results 80

3.5 Bias Errors and Uncertainties of the Analysis 81

3.6 Adverse Flow Effects 82

4 INSPECTION PROGRAM 83

5 CONCLUSIONS 86

6 REFERENCES 87

APPENDIX A VIBRATION ASSESSMENT FOR THE STEAM GENERATOR INTERNALS.....A1

APPENDIX B VIBRATION ASSESSMENT FOR THE REACTOR COOLANT SYSTEM PIPING AND THE PIPING ATTACHED TO THE STEAM GENERATOR.....B1

LIST OF TABLES

TABLE 2-1 COMPARISON OF THE DESIGN AND ARRANGEMENT OF THE VALID PROTOTYPE AND APR1400 RVI 9
TABLE 2-2 COMPARISON OF DIMENSIONS OF THE VALID PROTOTYPE AND APR1400 11
TABLE 2-3 NORMAL OPERATION DESIGN DATA OF THE VALID PROTOTYPE AND APR1400 12
TABLE 2-4 NATURAL FREQUENCIES OF THE VALID PROTOTYPE AND APR1400 13
TABLE 2-5 PREDICTED AND MEASURED STRESSES OF THE VALID PROTOTYPE 17
TABLE 3-1 MULTIPLYING FACTOR ON PUMP-INDUCED PRESSURES ON THE CSB 24
TABLE 3-2 TEMPERATURE ADJUSTMENT FACTOR FOR THE PSD LOADS ON THE CSB 24
TABLE 3-3 PUMP-INDUCED LOADS ON THE UGS TUBE BANK 30
TABLE 3-4 COHERENCE LENGTHS FOR THE UGS COMPONENTS 33
TABLE 3-5 PUMP-INDUCED LOADS ON THE LSS 37
TABLE 3-6 VORTEX SHEDDING LOADS ON THE ICI NOZZLE ASSEMBLY 41
TABLE 3-7 MULTIPLIERS OF LOADS ON THE ICI NOZZLE ASSEMBLY 42
TABLE 3-8 PUMP-INDUCED LOADS ON THE ICI NOZZLE ASSEMBLY 42
TABLE 3-9 PUMP-INDUCED LOADS ON THE CORE SHROUD 45
TABLE 3-10 PUMP-INDUCED LOADS ON THE IBA 48
TABLE 3-11 NATURAL FREQUENCIES OF THE CSB 52
TABLE 3-12 MAXIMUM STRESSES OF THE CSB FOR PUMP PULSATION LOADS 53
TABLE 3-13 MAXIMUM DISPLACEMENTS AND STRESSES OF THE CSB FOR RANDOM TURBULENCE LOADS 53
TABLE 3-14 MODAL ANALYSIS RESULTS OF THE UGS ASSEMBLY 58
TABLE 3-15 MAXIMUM DEFLECTIONS OF THE UGS FLANGES 58
TABLE 3-16 MODAL ANALYSIS RESULTS OF THE UGS TUBE BANK 61
TABLE 3-17 MAXIMUM STRESSES OF THE UGS TUBE BANK TO PUMP PULSATION LOADS 62
TABLE 3-18 MAXIMUM STRESSES OF THE UGS TUBE BANK TO RANDOM TURBULENCE LOADS 62
TABLE 3-19 NATURAL FREQUENCIES OF THE LSS 65
TABLE 3-20 MAXIMUM STRESS INTENSITIES OF THE LSS 66
TABLE 3-21 MODAL ANALYSIS RESULTS OF THE ICI NOZZLE ASSEMBLY 69
TABLE 3-22 MAXIMUM STRESS INTENSITIES OF THE ICI NOZZLE ASSEMBLY 70
TABLE 3-23 MAXIMUM STRESS INTENSITIES OF THE CORE SHROUD 74
TABLE 3-24 MODAL ANALYSIS RESULTS OF THE IBA 77

TABLE 3-25 MAXIMUM STRESS INTENSITIES OF THE IBA 78
TABLE 3-26 HIGH CYCLE FATIGUE EVALUATION FOR MAXIMUM STRESS REGIONS 80
TABLE 3-27 MAXIMUM STRESS INTENSITIES AND FATIGUE USAGE FACTORS 80
TABLE 4-1 REQUIRED TEST DURATION FOR CVAP 84
TABLE 4-2 CVAP TEST CONDITIONS FOR THE APR1400 85
TABLE A.3-1 THERMAL-HYDRAULIC DESIGN DATA FOR STEADY-STATE FULL-POWER OPERATIONS A9
TABLE A.3-2 MATERIALS OF MOISTURE SEPARATOR ASSEMBLY AND STEAM DRYER ASSEMBLY A16
TABLE A.3-3 SUMMARY OF THE VIBRATION AND STRESS ANALYSES A24

LIST OF FIGURES

FIGURE 2-1 GENERAL ARRANGEMENT OF THE RVI 4
FIGURE 2-2 CSB ASSEMBLY 5
FIGURE 2-3 UGS ASSEMBLY 6
FIGURE 2-4 FLOW PATHS IN THE RV 7
FIGURE 2-5 GENERAL ARRANGEMENT OF THE VALID PROTOTYPE 14
FIGURE 2-6 UGS ASSEMBLY OF THE VALID PROTOTYPE 15
FIGURE 3-1 SUMMARY OF ANALYTICAL METHODOLOGY 20
FIGURE 3-2 DEFINITIONS OF PUMP AZIMUTHAL LOCATIONS FOR THE CSB 25
FIGURE 3-3 REGIONS FOR PRESSURE PSD ON THE CSB 26
FIGURE 3-4 PRESSURE PSD ON THE CSB 27
FIGURE 3-5 ORIENTATION OF PUMP-INDUCED LOADS ON THE UGS ASSEMBLY 34
FIGURE 3-6 PRESSURE PSD ON THE UGS ASSEMBLY 35
FIGURE 3-7 ORIENTATION OF PUMP-INDUCED LOADS ON THE LSS 38
FIGURE 3-8 PRESSURE PSD ON THE LSS 38
FIGURE 3-9 PRESSURE PSD ON THE ICI NOZZLE ASSEMBLY 43
FIGURE 3-10 PRESSURE PSD ON THE CORE SHROUD 46
FIGURE 3-11 PRESSURE PSD ON THE IBA 49
FIGURE 3-12 AXISYMMETRIC MODEL OF THE CSB 54
FIGURE 3-13 TYPICAL MODE SHAPES OF THE CSB 55
FIGURE 3-14 LUMPED MASS BEAM MODEL OF THE CSB 56
FIGURE 3-15 LUMPED MASS BEAM MODEL OF THE UGS ASSEMBLY 59
FIGURE 3-16 FINITE ELEMENT MODEL OF THE UGS TUBE BANK 63
FIGURE 3-17 FINITE ELEMENT MODEL OF THE LSS 67
FIGURE 3-18 FINITE ELEMENT MODEL OF THE ICI NOZZLE ASSEMBLY 71
FIGURE 3-19 CORE SHROUD 75
FIGURE 3-20 FINITE ELEMENT MODEL OF THE IBA 79
FIGURE A.2-1 STEAM GENERATOR UPPER INTERNALS A3
FIGURE A.2-2 MOISTURE SEPARATOR ASSEMBLY A4
FIGURE A.2-3 STEAM DRYER ASSEMBLY A5
FIGURE A.2-4 FLOW PATHS OF SECONDARY SIDE FLUID IN THE STEAM GENERATOR A6
FIGURE A.3-1 COMPARISON OF EMPIRICAL NORMALIZED PSD EQUATION WITH FIELD-MEASURED DATA A10
FIGURE A.3-2 PRESSURE PSD FOR THE INSIDE OF THE MOISTURE SEPARATOR A11
FIGURE A.3-3 CFD MODEL OF THE STEAM GENERATOR UPPER INTERNALS A12

FIGURE A.3-4 PRESSURE PSD FOR THE MOISTURE SEPARATOR ASSEMBLY A13
FIGURE A.3-5 PRESSURE PSD FOR THE STEAM DRYER ASSEMBLY A14
FIGURE A.3-6 FINITE ELEMENT MODEL OF THE MOISTURE SEPARATOR ASSEMBLY A17
FIGURE A.3-7 NATURAL FREQUENCIES OF THE MOISTURE SEPARATOR ASSEMBLY A18
FIGURE A.3-8 MODE SHAPES OF THE MOISTURE SEPARATOR ASSEMBLY A19
FIGURE A.3-9 FINITE ELEMENT MODEL OF THE STEAM DRYER ASSEMBLY A20
FIGURE A.3-10 NATURAL FREQUENCIES OF THE STEAM DRYER ASSEMBLY A21
FIGURE A.3-11 MODE SHAPES OF THE STEAM DRYER ASSEMBLY A22
FIGURE B.2-1 ACOUSTIC RESONANCE FOR FLOW PAST STANDOFF PIPE B2
FIGURE B.2-2 FLOW PAST A CLOSED SIDE BRANCH B2
FIGURE B.3-1 LOCATIONS OF RCS ACOUSTIC INSTRUMENTATION B14

ACRONYMS AND ABBREVIATIONS

ASME	American Society of Mechanical Engineers
APR	Advanced Power Reactor
BPF	blade passing frequency
CEA	control element assembly
CFD	computational fluid dynamics
CSB	core support barrel
CVAP	comprehensive vibration assessment program
FAP	fuel alignment plate
GSSS	guide structure support system
GTE	guide tube extension
HFT	hot functional test
IBA	inner barrel assembly
ICI	in-core instrumentation
ID	inner diameter
KEPCO	Korea Electric Power Corporation
KHNP	Korea Hydro & Nuclear Power Co., Ltd
LSS	lower support structure
OD	outer diameter
PSD	power spectral density
RCP	reactor coolant pump
RCS	reactor coolant system
RMS	root mean square
ROK	Republic of Korea
RG	Regulatory Guide
RS	rotating speed
RV	reactor vessel
RVI	reactor vessel internals
SG	steam generator
SKNPP	Shin-Kori Nuclear Power Plant
SRSS	square root of the sum of the squares
SRV	safety relief valve
TS	Trade Secret
UGS	upper guide structure
UGSSP	upper guide structure support plate

1 INTRODUCTION

A comprehensive vibration assessment program (CVAP) has been developed for the reactor vessel internals (RVI) of the Advanced Power Reactor 1400 (APR1400) in accordance with Regulatory Guide (RG) 1.20 (Reference 1). The APR1400 RVI are classified as non-prototype Category I, with Palo Verde Unit 1, Westinghouse System 80 RVI as the valid prototype.

The CVAP for the APR1400 RVI consists of the analysis program and inspection program to verify the structural integrity of the RVI prior to commercial operation. This report presents a description of the CVAP and classification of the RVI (Section 2), the results of the vibration and stress analysis program (Section 3), and a description of the inspection program (Section 4).

A number of 1000 MWe reactors with non-prototype RVI whose valid prototype is Palo Verde Unit 1 are currently operating in the Republic of Korea (ROK). No adverse flow effects on the RVI of the reactors due to flow-induced vibrations have been reported. In addition, the Shin-Kori Nuclear Power Plant Unit 3, one of the APR1400 reactors under construction in the ROK, recently finished a hot functional test including the CVAP without any abnormality.

The vibration assessments of the steam generator internals and the piping systems attached to the reactor coolant system (RCS) are provided in Appendix A and Appendix B, respectively.

2 DESCRIPTION AND CLASSIFICATION OF THE REACTOR VESSEL INTERNALS

2.1 General Arrangement and Flow Conditions

The reactor vessel internals (RVI) consist of the core support structures and internal structures. The core support structures are the structures or parts of structures that are designed to provide direct support or restraint of the core within the reactor vessel (RV). The internal structures are all structures within the RV other than the core support structures, fuel assemblies, control element assemblies (CEAs), and instrumentations. The components of the RVI are divided into two major parts: the core support barrel (CSB) assembly and the upper guide structure (UGS) assembly. Although the flow skirt functions as an integral part of the coolant flow path, it is separated from the RVI and fixed to the bottom head of the RV. The general arrangement of the APR1400 reactor is shown in Figure 2-1.

The major structural member of the RVI is the CSB assembly. The CSB assembly consists of the CSB, lower support structure (LSS), in-core instrumentation (ICI) nozzle assembly, and core shroud. The CSB assembly is shown in Figure 2-2.

The CSB is a right circular cylinder that includes a heavy external ring flange at the top end and an internal ring flange at the lower end. The CSB is supported from a ledge on the RV. The CSB supports the LSS upon which the fuel assemblies rest. Four alignment keys that are 90 degrees apart are shrunk-fitted into the flange of the CSB. The RV closure head and flange, and the UGS assembly flange are slotted in locations corresponding to the alignment key locations to provide alignment between these components in the RV flange region. The upper section of the CSB contains two outlet nozzles that interface with internal projections on the RV outlet nozzles to minimize leakage of coolant from inlet to outlet.

Since the weight of the CSB is supported at its upper end, it is possible for coolant flow to induce vibrations in the structure. Therefore, amplitude-limiting devices, or snubbers, are installed on the outside of the CSB near the bottom end. The snubbers consist of six equally-spaced lugs around the circumference of the CSB and act as a tongue-and-groove assembly with the mating lugs on the RV. Minimizing the clearance between the tongue-and-groove assembly limits the amplitude of vibration. During assembly, as the RVI are lowered into the RV, the RV lugs engage with the CSB lugs in an axial direction. Radial and axial expansions of the CSB are accommodated, but lateral movement of the CSB is restricted. The lower flange of the CSB supports, secures, and positions the LSS and is attached to the LSS by means of a welded flexural connection.

The LSS provides support for the core by means of support beams that transmit the load to the CSB lower flange. The LSS and ICI nozzle assembly position and support the fuel assemblies, core shroud, and ICI nozzles. The structure is a welded assembly consisting of a short cylinder, support beams, bottom plate, ICI nozzles, and ICI nozzle support plate.

The LSS is made up of a short cylindrical section enclosing an assemblage of grid beams arranged in an egg-crate fashion. The outer ends of the beams are welded to the cylinder. The fuel assembly locating pins are attached to the top of the beams. The locating pins in the beams provide orientation for the lower ends of the fuel assemblies. The bottoms of the main support beams are welded to an array of plates that contain flow holes to provide proper flow distribution. The plates also provide support for the ICI nozzles, support columns, and ICI nozzle support plate. The cylinder guides the main coolant flow and limits the core shroud bypass flow by means of holes located near the base of the cylinder. The ICI nozzle support plate provides lateral support for the ICI nozzles. The plate is provided with flow holes for the requisite flow distribution.

The core shroud provides an envelope for the core and limits the amount of coolant bypass flow. The core shroud consists of a welded vertical assembly of plates designed to channel the coolant through the core. Circumferential rings and top and bottom end plates provide lateral support. The rings are attached to the vertical plates by means of full-length welded ribs and horizontal braces. A small gap is provided between

the core shroud outer perimeter and the core support barrel in order to provide upward coolant flow in the annulus, thereby minimizing thermal stresses in the core shroud.

The UGS assembly aligns and laterally supports the upper end of the fuel assemblies, maintains the CEA spacing, holds down the fuel assemblies during operation, prevents fuel assemblies from being lifted out of position during a severe accident condition, and protects the CEAs from the effects of coolant cross flow in the upper plenum. The UGS assembly consists of the UGS barrel assembly and the inner barrel assembly (IBA) (Figure 2-3).

The UGS barrel assembly consists of the UGS support barrel, fuel alignment plate (FAP), UGS support plate, and CEA guide tubes. The UGS support barrel consists of a right circular cylinder welded to a ring flange at the upper end and to a circular plate (UGS support plate) at the lower end. The flange, which is a supporting member for the entire UGS assembly, seats on its upper side against the RV head during operation. The lower side of the flange is supported by the hold-down ring, which seats on the CSB upper flange. The UGS flange and the hold-down ring engage the CSB alignment keys by means of four accurately machined and located keyways equally spaced at 90-degree intervals.

This system of keys and slots provides an accurate means of aligning the core with the closure head and thereby with the CEA drive mechanisms. The FAP is positioned below the UGS support plate by cylindrical CEA guide tubes. These tubes are attached to the UGS support plate and the FAP by rolling the tubes into the holes in the plates and welding. The FAP is designed to align the lower ends of the CEA guide tubes that in turn locate the upper ends of the fuel assemblies. The FAP also has four equally spaced slots on its outer edge that engage with lugs protruding from the core shroud to provide alignment. The CEA guide tubes bear the upward force on the fuel assembly hold-down devices. This force is transmitted from the FAP through the CEA guide tubes to the UGS barrel support plate.

The IBA limits cross flow and provides guidance of the CEAs. The IBA consists of a top plate welded to a right circular barrel open at the bottom and an assemblage of large vertical tubes connected by vertical plates in a grid pattern welded to the inside of the barrel. The IBA is held in position by continuous weld between the barrel flange and the top surface of the UGS barrel upper flange. Guides for the CEA extension shafts are provided by the top plate of the IBA. The tubes and connecting plates within the IBA are furnished with multiple holes to permit hydraulic communication.

The hold-down ring provides axial force on the flanges of the UGS assembly and the CSB assembly in order to prevent movement of the structures under hydraulic forces. The hold-down ring is designed to accommodate the differential thermal expansion between the RV and the RVI in the RV ledge region.

The flow skirt is a right circular cylinder, perforated with flow holes, and reinforced with two stiffening rings. The flow skirt is used to reduce inequalities in core inlet flow distributions and to prevent formation of large vortices in the lower plenum. The flow skirt is supported by nine equally spaced machined sections that are welded to the bottom head of the RV.

The main coolant from the four RV inlet nozzles flows down to the flow skirt through the annulus between the RV and the CSB and flows upward through the core support region and the reactor core. Finally, it exits through two reactor outlet nozzles. A portion of this flow bypasses to cool the RVI and the CEAs. The reactor coolant flow path is depicted in Figure 2-4.

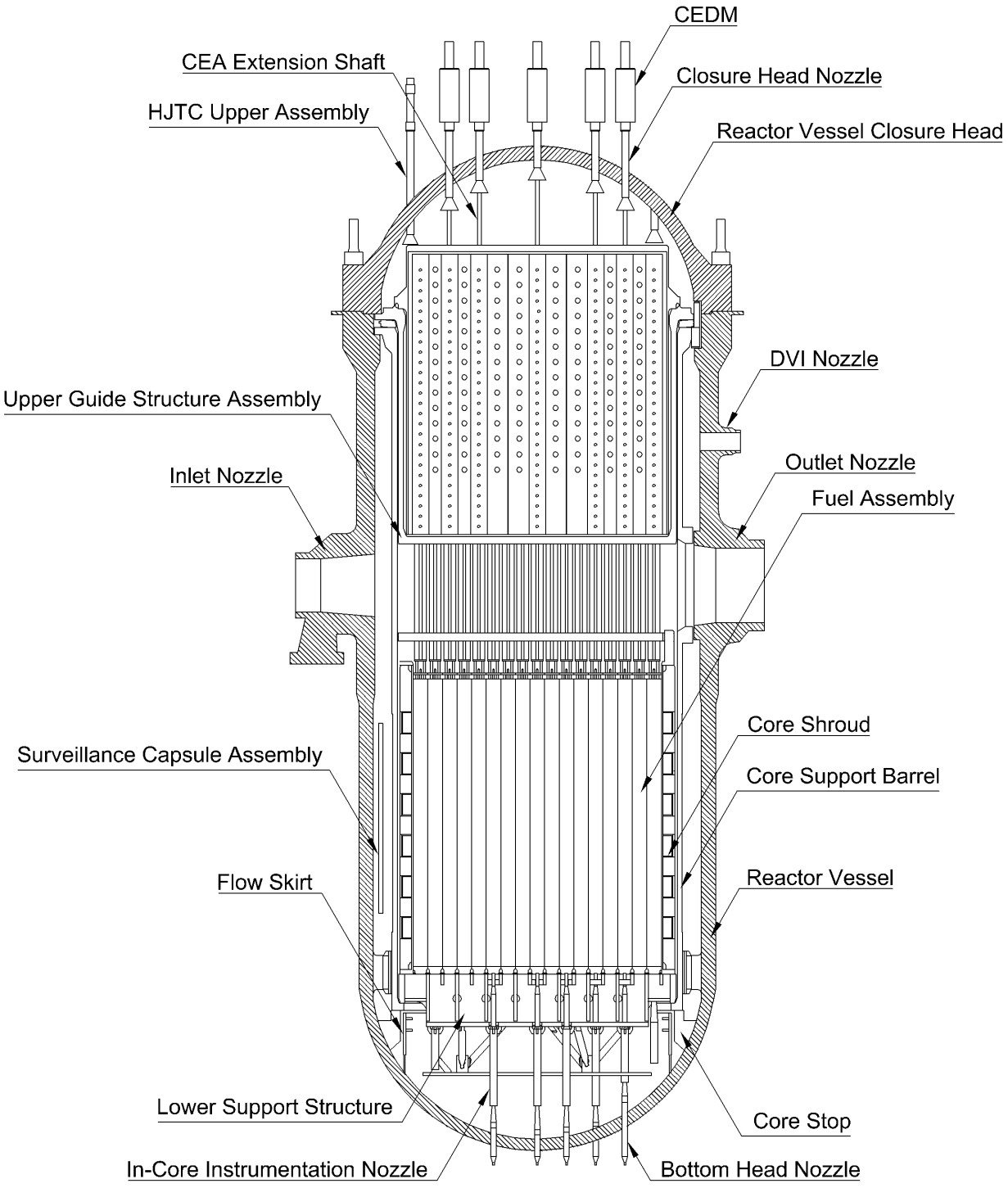

Figure 2-1 General Arrangement of the RVI

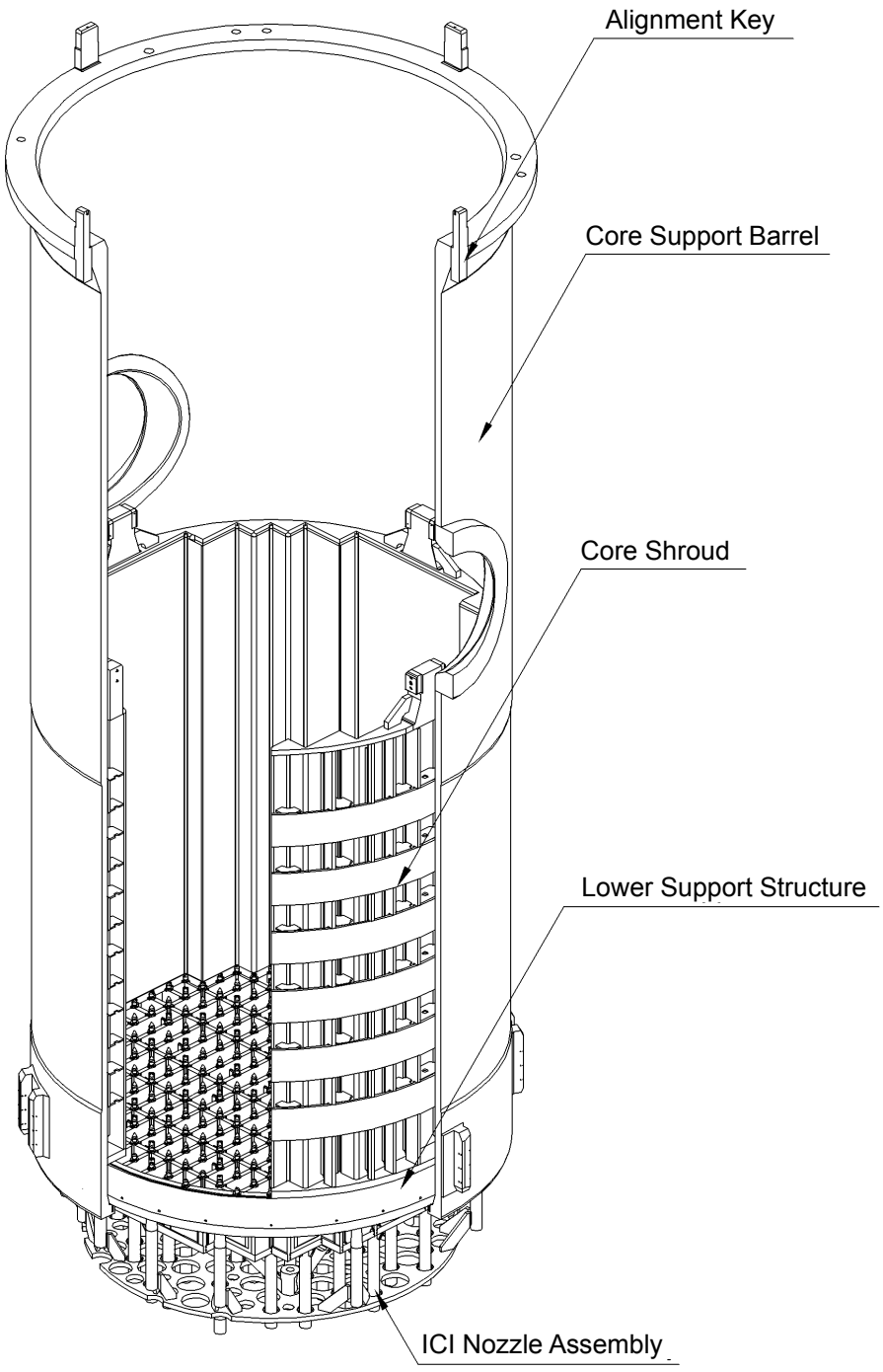

Figure 2-2 CSB Assembly

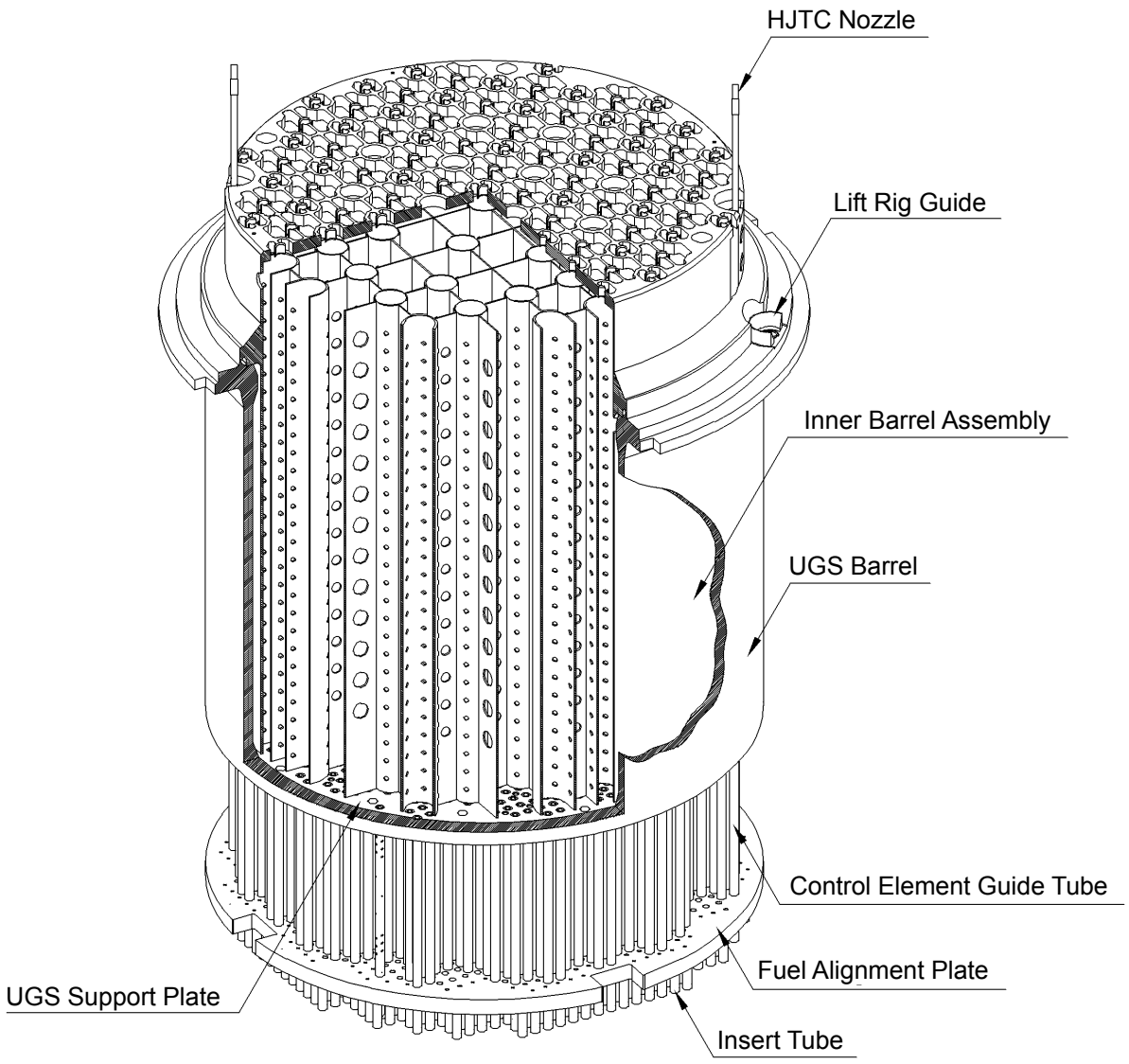

Figure 2-3 UGS Assembly

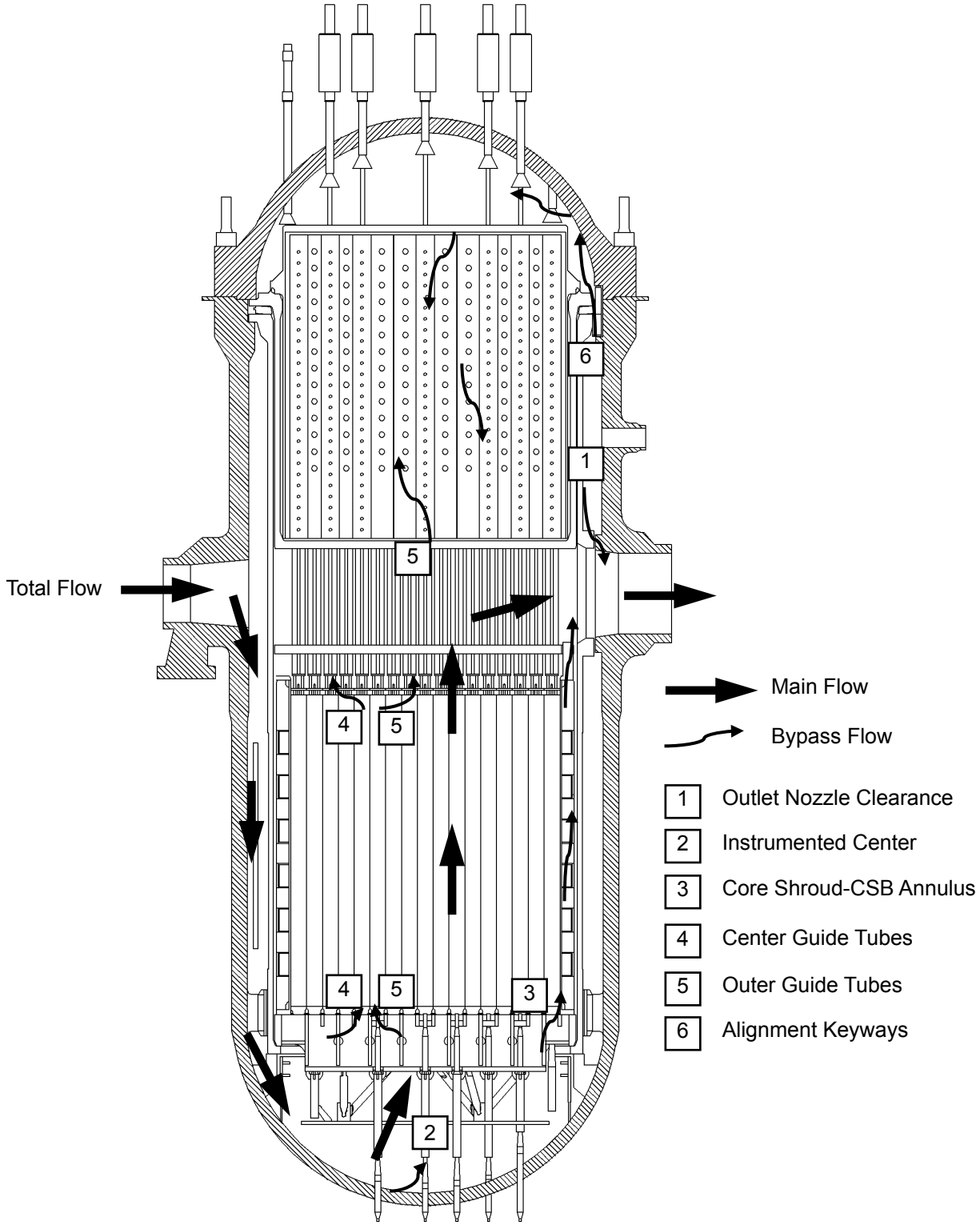

Figure 2-4 Flow Paths in the RV

2.2 Classification of the Reactor Vessel Internals in Accordance with the Comprehensive Vibration Assessment Program

The RG 1.20 (Reference 1) classifies non-prototype Category I RVI as follows:

> "Non-prototype, Category I" reactor internals are those configurations that have substantially the same arrangement, design, size, and operating conditions as a specified "valid prototype," for which nominal differences in arrangement, design, size, and operating conditions have been shown (by test or analysis) to have no significant effect on the vibratory response and excitation of those reactor internals important to safety.

Based on this classification and the rationales provided below, the APR1400 RVI are classified as non-prototype Category I, with Palo Verde Unit 1, Westinghouse System 80 RVI, as the valid prototype.

Tables 2-1 and 2-2 provide a comparison of the designs, arrangements, and dimensions of the valid prototype RVI and the APR1400 RVI. Table 2-3 provides a comparison of operating conditions of the reactors. These tables show that the APR1400 RVI have substantially the same designs, arrangement, size, and operating conditions as those of the valid prototype RVI. Figure 2-5 shows the general arrangement of the valid prototype reactor while Figure 2-1 shows the APR1400 RVI. Also, the flow condition of the APR1400 shown in Figure 2-4 is the same as that of the valid prototype.

The nominal difference between the valid prototype and APR1400 RVI is the IBA, which replaces the CEA shroud of the valid prototype. The purpose of the IBA and the CEA shroud is to guide the CEAs. Their tubes and webs are both made from Type 304 stainless steel.

The CEA shroud of the valid prototype reactor consists of an array of vertical round tubes that are arranged in a square grid pattern as shown in Figure 2-6. The tubes are joined by welded vertical plates called webs between adjacent tubes. The CEA shroud is mounted on eight pads on the UGS support plate and is held in position by eight tie rods that are threaded in the UGS support plate at their lower end. At their upper end, the pre-tensioned tie rods are held by nuts which bear on eight plugs in the tops of eight CEA shroud tubes.

Since the global modes of vibration of the CEA shroud may cause lateral deflection of the outer tubes and webs and may contribute to high stresses, four snubbers are added to the CEA shroud to limit such lateral deflection. The snubber consists of three pieces. A snubber block assembly is shop welded into the three outermost shroud tubes on each of the four sides of the CEA shroud. A flange block assembly is field installed on the UGS barrel flange by pins and bolts. A hard shim is field fitted to the snubber block to provide controlled clearance with the sides of the slot in the flange block. The completed snubber assembly allows radial and axial differential motion between the CEA shroud and the UGS barrel but restricts lateral or tangential motion of the CEA shroud.

The IBA tubes and webs of the APR1400 reactor (see Figure 2-3) are arranged in the same square grid pattern as the CEA shroud of the valid prototype. Instead of eight tie rods and four snubbers to provide support for the tubes and webs, all the outer tubes of the IBA are welded to the IBA cylinder and flange, and the IBA flange is welded to and mounted on the UGS flange to reduce vibration due to flow-induced and seismic loads. A flexure type welding method is applied to the junction between the IBA and UGS flanges to allow radial thermal expansion. To guide all the 4-finger and 12-finger CEA extension shafts, the IBA upper cylinder and top plate are welded to the IBA flange. The IBA upper flange and top plate have the same configuration as the guide structure support system (GSSS), shown in Figure 2-6, of Palo Verde Units 2 and 3 whose valid prototype is also Palo Verde Unit 1.

The design of the IBA does not cause any difference in the flow from the valid prototype reactor in the main and bypass flow of the APR1400 reactor, as depicted in Figure 2-4, because the IBA has the same configuration of tubes and webs as the CEA shroud of the valid prototype. The IBA integrates all of the

parts that limit vibration of the CEA shroud of the valid prototype with a welding engagement method. In addition, the IBA is located in the upper plenum, which is not on the main flow path. The detailed response analyses of the IBA show that the structural integrity of the IBA is maintained for flow-induced loads as described in Subsections 3.2.7 and 3.3.7.

There are minor differences in some areas. The CSB and UGS flanges, and the upper guide structure support plate (UGSSP) and the FAP of the APR1400 are thicker than those of the valid prototype. The design of stiffeners for the core shroud vertical plate and the ICI nozzles for APR1400 are changed from the valid prototype. In addition, there are small differences in the size and arrangement of the RVI between the APR1400 and the valid prototype such as the number of CEA guide tubes and flow holes in the FAP.

The natural frequencies of the APR1400 (see Tables 3-11, 3-14, and 3-21) are compared with the corresponding measured frequencies and predicted values of the valid prototype (Reference 4). As shown in Table 2-4, the frequencies of the APR1400 in the analyses agree with those of the valid prototype in all areas of the RVI.

Table 2-1 Comparison of the Design and Arrangement of the Valid Prototype and APR1400 RVI

Valid Prototype	APR1400
Core Support Barrel	
A. Right circular cylinder, three sections, supported by heavy external flange top end, heavy internal flange bottom end.	A. Right circular cylinder, three sections, supported by heavy external flange top end, heavy internal flange bottom end.
B. Two outlet nozzles through barrel.	B. Two outlet nozzles through barrel.
C. Top flange seats on RV ledge, and has four alignment keys attached.	C. Top flange seats on RV ledge, and has four alignment keys attached.
D. Bottom flange supports LSS, fuel, and core shroud.	D. Bottom flange supports LSS, fuel, and core shroud.
E. Top flange supports UGS assembly.	E. Top flange supports UGS assembly.
F. Six amplitude limiting devices (snubbers) attached to lower barrel.	F. Six amplitude limiting devices (snubbers) attached to lower barrel.
Lower Support Structure	
A. Made up of interlocked grid beams with surrounding short cylinder and perforated bottom plates attached to the bottoms of the beams.	A. Made up of interlocked grid beams with surrounding short cylinder and perforated bottom plates attached to the bottoms of the beams.
B. Fuel support pins are attached to the top end of the grid beams.	B. Fuel support pins are attached to the top end of the grid beams.
C. The core shroud assembly is attached to the top of the LSS cylinder.	C. The core shroud assembly is attached to the top of the LSS cylinder.
D. The LSS cylinder rests on and is attached to the CSB bottom (internal) flange.	D. The LSS cylinder rests on and is attached to the CSB bottom (internal) flange.

Table 2-1 Comparison of the Design and Arrangement of the Valid Prototype and APR1400 RVI (Continued)

Valid Prototype	APR1400
Upper Guide Structure	
A. Right circular cylinder supported by a heavy external flange type end, and heavy plate attached to bottom end.	A. Right circular cylinder supported by a heavy external flange top end, and heavy plate attached to bottom end.
B. Heavy plate in "A" is perforated with flow holes and guide tubes.	B. Heavy plate in "A" is perforated with flow holes and guide tubes.
C. A second heavy perforated plate supports the bottom ends of the guide tubes.	C. A second heavy perforated plate supports the bottom ends of the guide tubes.
D. This second heavy plate in "C" engages with guide lugs on the core shroud.	D. This second heavy plate in "C" engages with guide lugs on the core shroud.
E. The guide tubes are welded to the two heavy plates above.	E. The guide tubes are welded to the two heavy plates above.
CEA Shroud Assembly / Inner Barrel Assembly	
A. A series of large diameter tubes are connected together by full length webs.	A. A series of large diameter tubes are connected together by full length webs.
B. All welded construction.	B. All welded construction.
C. N/A	C. The shroud tube and web assembly is connected to an external cylinder.
D. The tube and web assembly is supported by the UGS support plate via tie rods and incorporates four interlocking snubbers to the upper UGS.	D. The tube, web, and cylinder assembly is supported by the UGS upper flange.
E. Material - Austenitic Stainless Steel	E. Material - Austenitic Stainless Steel

Table 2-2 Comparison of Dimensions of the Valid Prototype and APR1400

Component	Valid Prototype	APR1400
Core support barrel:		
Length, mm (in)	9,734.6 (383-1/4)	9,715.5 (382-1/2)
Diameter (ID), mm (in)	3,987.8 (157)	3,987.8 (157)
Thickness upper, mm (in)	76.2 (3)	76.2 (3)
Thickness middle, mm (in)	66.7 (2-5/8)	66.7 (2-5/8)
Thickness lower, mm (in)	76.2 (3)	76.2 (3)
Outlet nozzles, (quantity)	2	2
Outlet nozzles diameter (ID), mm (in)	1,184.3 (46-5/8)	1,184.3 (46-5/8)
Snubbers, (quantity)	6	6
Lower support structure:		
Cylinder height, mm (in)	412.8 (16-1/4)	412.8 (16-1/4)
Cylinder diameter (OD), mm (in)	3,970.3 (156-5/16)	3,970.3 (156-5/16)
Main beams, (quantity)	16	16
Beam thickness, mm (in)	44.5 (1-3/4)	44.5 (1-3/4)
Beam height, mm (in)	669.9 (26-3/8)	669.9 (26-3/8)
Upper guide structure:		
Length, mm (in)	4,924.4 (193-7/8)	4,924.4 (193-7/8)
Diameter flange (OD), mm (in)	4,559.3 (179-1/2)	4,559.3 (179-1/2)
Diameter barrel (OD), mm (in)	3,962.4 (156)	3,962.4 (156)
Barrel thickness, mm (in)	76.2 (3)	76.2 (3)
CEA guide tubes (quantity)	804	820
FAP diameter, mm (in)	3,962.4 (156)	3,962.4 (156)
Plate thickness, mm (in)	114.3 (4-1/2)	139.7 (5-1/2)

Table 2-3 Normal Operation Design Data of the Valid Prototype and APR1400

Design Data	Valid Prototype	APR1400
RV design pressure, kg/cm²A (psia)	175.8 (2,500)	175.8 (2,500)
RV normal operating pressure, kg/cm²A (psia)	158.2 (2,250)	158.2 (2,250)
Normal operating coolant inlet temperature, °C (°F)	296.1 (565)	290.6 (555)
Normal operating coolant outlet temperature, °C (°F)	327.3 (621.2)	323.9 (615)
Design temperature, °C (°F)	343.3 (650)	343.3 (650)
Normal operating coolant flow rate, L/min (gpm)	1,687,000 (445,600)	1,689,000 (446,300)
Mechanical design coolant flow rate(with core), L/min (gpm)	1,965,000 (519,124)	1,943,000 (513,200)
Mechanical design coolant flow rate(without core), L/min (gpm)	2,066,000 (545,860)	2,112,000 (557,900)
Reactor coolant pump frequency (Hz)	20	20
Reactor coolant pump blade passing frequency (Hz)	120	120

Table 2-4 Natural Frequencies of the Valid Prototype and APR1400

TS

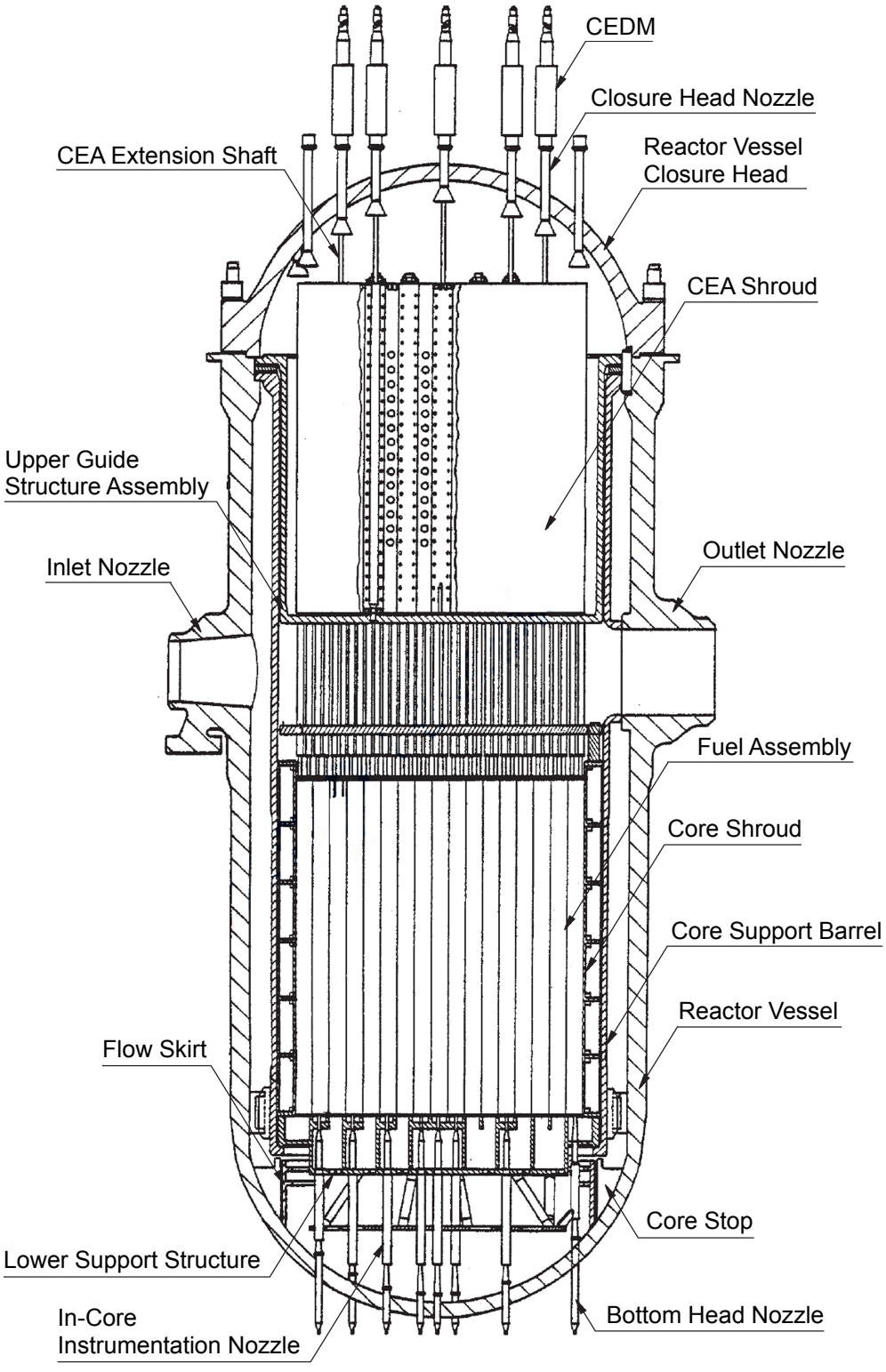

Figure 2-5 General Arrangement of the Valid Prototype

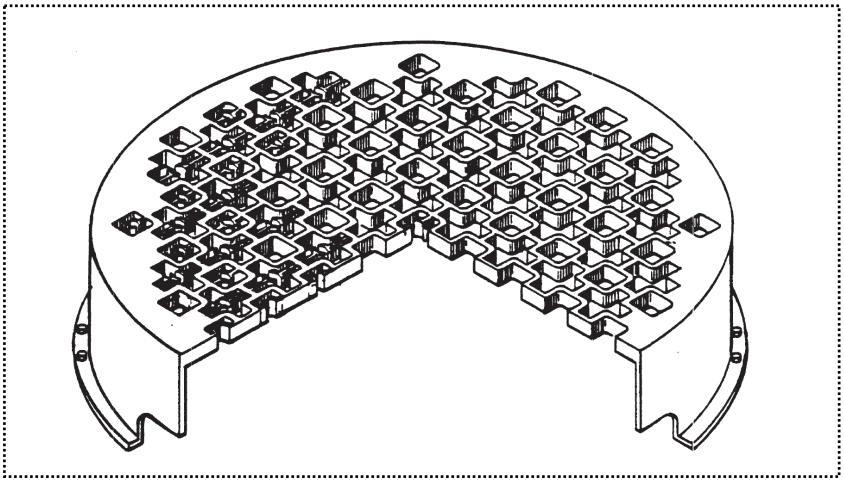

GSSS applied to Palo Verde Units 2 and 3

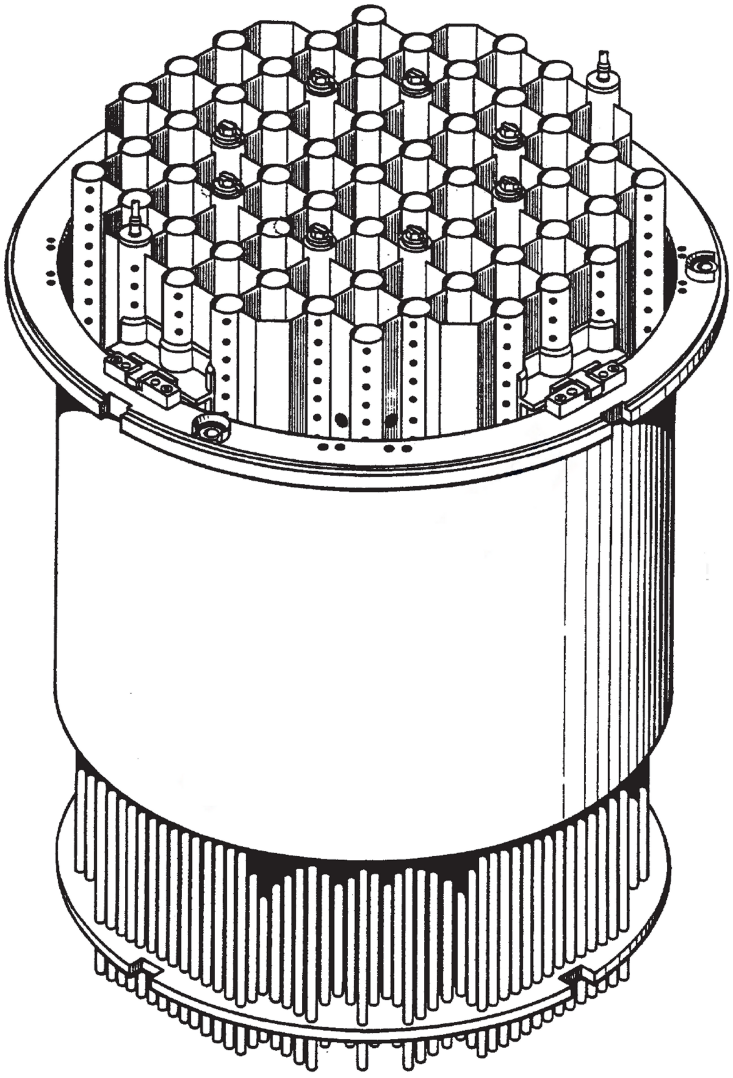

Figure 2-6 UGS Assembly of the Valid Prototype

2.3 Summary of the Valid Prototype CVAP

The CVAP of the valid prototype is summarized in this section, and details are provided in "A Comprehensive Vibration Assessment Program for Palo Verde Nuclear Generating Station Unit 1" (Reference 4).

Analyses were completed for the flow-induced loads of the two safety-related assemblies, the CSB assembly (CSB and LSS) and the UGS assembly (see Figures 2-2 and 2-3). Maximum predicted stresses, summarized in Table 2-5, are alternating stress intensities due to flow-induced dynamic loads predicted for CVAP test conditions corresponding to normal operation.

Based on the results of the analyses, the measurement program was developed. The purpose of this program was to obtain data on both random and deterministic excitation (pressure) and structural response (displacement, strain, and acceleration). Instrumentation, consisting of pressure transducers, strain gages, accelerometers, and displacement transducers, was used for each assembly. A test was completed at the steady-state and transient (pump startup and shutdown) conditions corresponding to normal and part loop operation. The pre-core flow test of approximately 1,200 hours was completed to provide reasonable assurance that the components were subjected to more than 10^6 cycles of vibration before inspection. Data were acquired to compare with the predicted values of hydraulic forcing functions and structural responses. In all cases, the measured values of stress were less than the acceptance limits. The evaluation of the test data showed that the measured stresses were less than the predicted values listed in Table 2-5.

The pre-core inspection of the RVI was performed before initiation and after completion of all pre-core flow tests. In both cases, the RVI were positioned to permit visual inspection of the specified locations. Major load-bearing surfaces, contact surfaces, welds, maximum stress locations identified in the analysis program, and the CVAP instrumentation, mountings, and conduits were examined. A photographic record was made for all observations. The baseline stage was completed to establish a foundation on which to compare the results of the post-stage after the RVI were subjected to the hot functional test vibration, which exceeded the required number of cycles of vibration.

A comparison of the baseline stage surface conditions with the post stage surface conditions indicated that with the exception of damage to the CEA shroud and damage and debris from the reactor coolant pumps, no abnormal flow-induced vibration had occurred and no reduction in the structural integrity of the RVI and the RV had occurred. There were indications of normal amounts of relative thermal growth between the RVI and RV at the flange surfaces, and there were indications of contact between surfaces at the snubbers, guide lugs, and alignment keys.

Damage to the CEA shroud was evaluated, and modifications were made to the RVI to maintain the structural adequacy of the CEA shroud (Reference 7). A baseline stage visual inspection was performed on the modified RVI, along with a vibration measurement program and an analysis program. The results of a post stage visual inspection revealed no evidence of unacceptable motion, excessive or undue wear or deviation from the predicted results of the analysis program. Reactor coolant pump debris was found in the RV and removed. The results of the visual inspection for the valid prototype are presented in detail in Reference 4.

The evaluation of the comparisons of analytical predictions, test measurements, and visual inspection results led to the conclusion that the RVI for the valid prototype are structurally adequate and acceptable for long-term operation. Measured response strains were all smaller than the predicted values, resulting in fatigue margins of safety, which were more than adequate. The methods employed in the various phases (analysis, test, and inspection) of the CVAP of the valid prototype were valid and sufficient to meet the requirements of RG 1.20.

Table 2-5 Predicted and Measured Stresses of the Valid Prototype (Reference 4)

TS

3 VIBRATION AND STRESS ANALYSIS PROGRAM

3.1 General Methodology

The methodology used to calculate the dynamic responses of the RVI to flow-induced loads is divided into the following three parts and summarized in Figure 3-1:

- Calculation of hydraulic loads (or forcing functions)
- Analysis of the structures to determine their modal characteristics (e.g., frequencies, mode shapes)
- Calculation of the dynamic response (e.g., displacement, strain, stress)

The flow-induced dynamic loads are classified as periodic(deterministic) or random loads. The periodic and random loads are assumed to be uncorrelated and caused by independent sources. The hydraulic loads can thus be calculated separately for the periodic and random sources of excitation as shown in Figure 3-1. A description of both the periodic and random loads includes information on their magnitudes, frequencies, and spatial distributions.

The RVI and the fluid surrounding them are dynamically coupled with the dynamic response of the structure influencing the fluid pressure distribution. The coupling results in an additional inertial force on the structure. The added force appears analytically as a mass, proportional to fluid density, and added to the mass of the structure. With the use of the “hydrodynamic mass”, the calculation of the hydraulic load can be uncoupled from the calculation of the response. The modal characteristics of the structure in the fluid can then be established by including the hydrodynamic added mass and solving the set of equations that describe the free vibration force balance on the structure.

The structural response to the hydrodynamic loads is a function of the type of load (periodic or random), its magnitude, frequency and spatial distribution and modal characteristics of the structure. The response is the sum of the responses due to periodic and random loads and is calculated using the procedure shown in Figure 3-1.

3.1.1 Hydraulic Loads

The periodic loads acting on the RVI of primary interest are caused by pump-induced pressure fluctuations. The pressure fluctuations (pulsations) are due to harmonic variations in fluid pressure caused by the reactor coolant pump (RCP). The pulsations propagate throughout the system as acoustic waves, independent of the fluid velocity (flow rate). The pulsations occur at harmonics of the pump rotating speed (RS) and blade passing frequency (BPF). A combination of mathematical analysis and the valid prototype CVAP test is used to compute the magnitudes and distributions of the periodic loads caused by the pulsations. For operations with more than one pump, the principle of superposition is used to account for the pump azimuthal locations and the phasing between pumps. The phasing between pumps is chosen to provide the maximum pressure fluctuations acting on the components.

The random loads are generated by flow turbulence. Random loads include turbulent buffeting of the structures which is a function of crossflow velocity, and turbulence-induced variations in parallel flow over the surface of structures. Because of the random nature of the loads, statistical methods are used to define both their magnitude and frequency content in the form of power spectral densities (PSDs). Spatial distributions are described by specifying areas and/or lengths over which these loads can be considered coherent. All random loads are assumed to be stationary and ergodic. Pressure PSD representations, in the form of pressure squared per unit frequency versus frequency, are derived from the valid prototype CVAP test data. Appropriate adjustments are made to derive the design hydraulic loads.

3.1.2 Structural Analysis

The natural frequencies and mode shapes of the RVI are determined using finite element models or multiple degrees of freedom lumped mass models. The choice of a particular method depends on the complexity of the structure and the nature of the hydraulic loads.

Dynamic equilibrium of the structure is described by a force balance, which includes mass dependent inertial forces, resistive forces due to velocity dependent damping, and restoring forces, which are related to structural stiffness and displacement. Inertial forces are described by mass times the unknown accelerations. In air, the mass is the structural mass, while for the in-water case, a hydrodynamic mass is added to the structural mass. This hydrodynamic mass is determined by analytical means, from the valid prototype CVAP test data, and equations in the relevant literature. The hydrodynamic mass, being dependent on fluid density, varies with temperature and results in variations in structural frequency with coolant temperature. Structural stiffness depends on material properties, geometry, and boundary conditions. The resulting set of equations is solved for the modal frequencies and corresponding mode shapes.

The dynamic response of any particular assembly is the sum of the responses to the periodic and random loads. In either case, the response is a function of the magnitude of each load, its frequency and spatial distribution and the modal frequencies and corresponding mode shapes of the assembly. The functional relationships between the response and these factors vary depending on whether the excitation is periodic or random.

For periodic loads, the loads and responses have the same harmonic variation with time. The amplitude of the response, for any particular mode, is inversely proportional to the difference between the squares of the modal and forcing frequencies and directly proportional to the modal participation factor and applied loads.

The response to random loads is calculated using statistical methods developed for analyzing random vibrations. The product of the load, expressed as a PSD, and the frequency response characteristics or transfer function, is integrated over a frequency range to obtain the mean square value (root mean square [RMS] value squared) of the response. Spatial variations in the loads are accounted for by performing this integration over the area on which the loads are coherent.

The total response due to hydraulic loads is the sum of the periodic and random contributions.

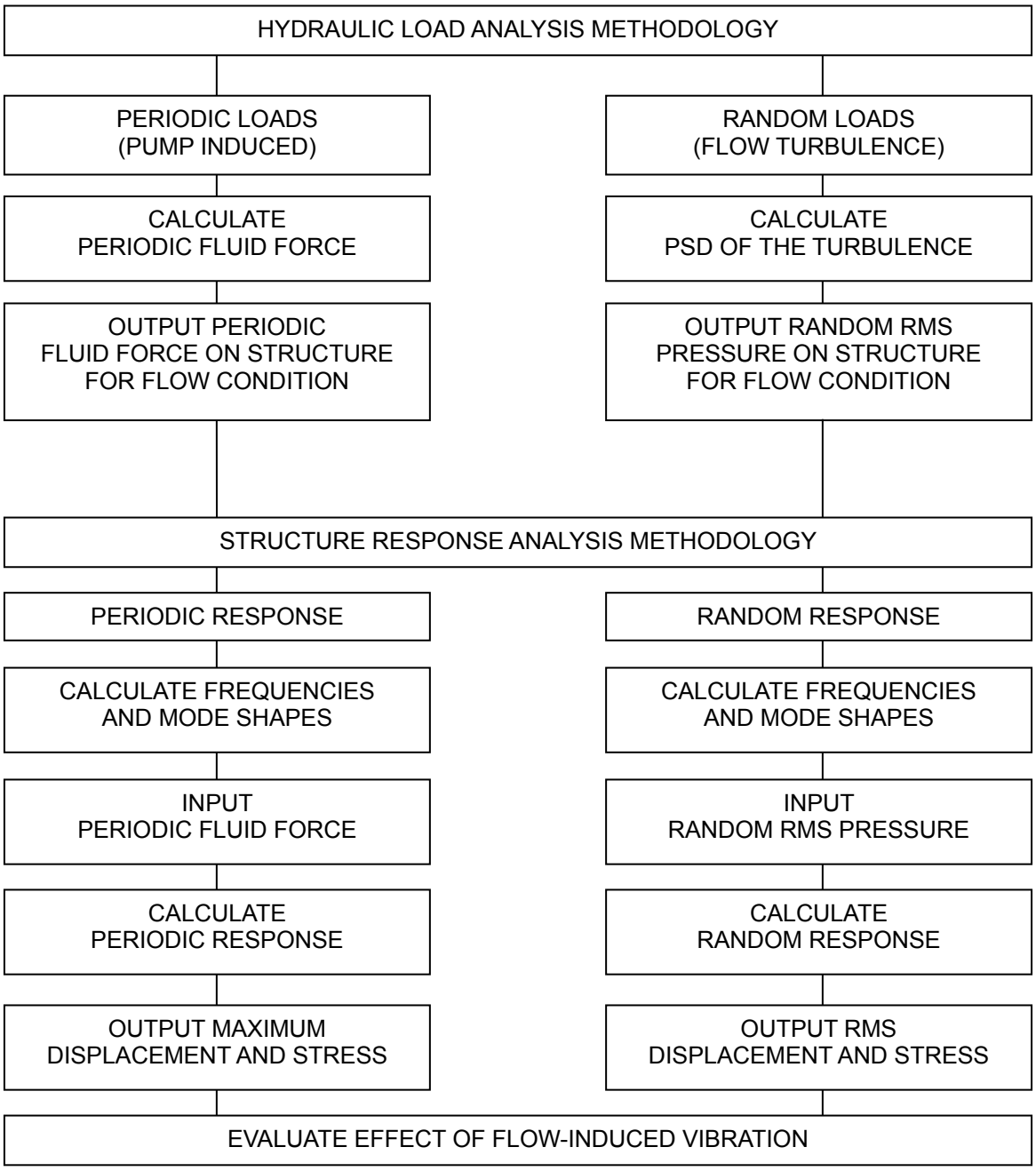

Figure 3-1 Summary of Analytical Methodology

3.2 Calculation of the Forcing Function

3.2.1 Analytical Method

The analytical method that is used to calculate the forcing function assumes that hydraulic forcing functions, that are associated with steady and transient operating conditions, are separated into periodic and random components.

Periodic loads of primary interest are those that are caused by pump-induced pressure fluctuations. The forces are acoustic, and occur at the harmonics of the pump rotor speed and blade passing frequency, which is independent of flow rate.

Flow-induced random loads are primarily due to turbulence. The magnitudes of these forces are normally proportional to the kinetic head ($\rho V^2/2$) and the loads occur over a broad range of frequencies.

Methods for developing the periodic and random loads of the hydraulic forcing function are discussed in Subsection 3.2. Where complex flow path configurations or wide variations in pressure distribution are involved, the hydraulic forcing functions are formulated using a combination of analytical and empirical methods. The empirical methods include data obtained from plant tests.

The only transients considered important are the ones caused by pump startup and shutdown for the CVAP. These transients cause variations, with time, in flow rate and pump rotor and blade passing frequencies, which could affect both the magnitude and frequency of the flow-induced loads and the structural response.

The magnitude and frequency of the periodic loads caused by pump pressure pulsations are independent of fluid velocity and are thus unaffected by transient variations in flow rate. The increase or decrease in pump rotational frequency with time, however, causes changes in the frequency of propagation of these pulsations. In some cases, the changes result in a momentary resonance condition between the force and the structure. However, the duration of the resonance is short compared to the response time of the structure, and the resonance does not result in any significant amplification of the response.

The magnitude of the random forces is proportional to kinetic head while its frequency content depends, to some extent, on flow velocity. The power spectral densities for the random loads are in general wide band, with the maximum frequency at least equal to the maximum frequency at which the structure has a significant response. Thus, any minor variations in frequency content do not change the response.

Based on this evaluation, any difference in the magnitudes and frequencies of the flow-induced loads from their steady state values due to transient changes in flow rate and pump rotational frequencies should have no significant effect on the structural response. Consequently, the magnitudes of the transient flow-induced loads are assumed to be equal to their steady-state values, either before or after the transient, and the loads are assumed to occur at frequencies equal to their steady-state values.

3.2.2 Core Support Barrel

An analysis based on an idealized hydrodynamic model (References 2 and 3) is used to obtain the relationship between RCP pulsation in the inlet ducts and the periodic pressure fluctuations on the CSB. The model represents the annulus of coolant between the CSB and the RV. In deriving the governing hydrodynamic differential equation for the above model, the fluid is taken to be compressible and inviscid. The equations of motion and continuity are linearized. The excitation on the hydraulic model is harmonic with the frequencies of excitation corresponding to pump rotational speeds and blade passing frequencies. The result of the hydraulic analysis is used to define the forced response, natural frequencies and natural modes of the hydrodynamic model.

Figure 3-2 shows azimuthal locations in the model developed to obtain the pressure fluctuations on the CSB due to the operation of pumps. The idealized model represents the annulus of coolant between the CSB and the RV. The radii r_1 and r_2 correspond to the outer radius of the CSB and inner radius of the RV, respectively. The length, L, corresponds to the length of the annulus between the CSB and RV. The area bounded by z_1 and z_2 in the vertical direction and θ_1 and θ_2 in the circumferential direction corresponds to the area of the inlet duct and is located at the position of an inlet duct.

From equations of motion, continuity equation, and equation of state, the desired acoustic wave equation is derived. The solution describes the pressure in the downcomer annulus as a function of space and time. In cylindrical coordinates, the wave equation can be written as follows:

$$\frac{\partial^2 P}{\partial r^2}+\frac{1}{r}\frac{\partial P}{\partial r}+\frac{1}{r^2}\frac{\partial^2 P}{\partial \theta^2}+\frac{\partial^2 P}{\partial z^2}=\frac{1}{C_0^2}\frac{\partial^2 P}{\partial t^2}$$

Where:

P = fluctuating pressure
C_0 = reference velocity of sound
t = time

To solve the wave equation, the following boundary conditions are applied:

- The inner vertical wall is considered to be rigid
- The outer vertical wall is considered to be rigid except at the location of the pump inlets where the radial pressure gradient is described.
- The top of the cylinder is considered to be a rigid surface.
- The bottom of the cylinder is considered to be an open surface.

The boundary conditions of the wave equation give a complete description of the problem. The final solution defines the spatial distribution of pressure on the CSB.

Analytical predictions of periodic forcing functions are based on the inlet duct pressure pulsation of 6,895 Pa (1 psi) and one pump operation for simplicity. Calculations are performed for all CVAP test condition temperatures. Results for multiple pump operation are obtained by superposition of the results of one pump and are presented as the maximum amplitude for six pump forcing frequencies, which are the pump rotor, twice the rotor, blade passing frequency, twice, three times and four times the blade passing frequency. Final results are obtained using the multiplying factor given in Table 3-1.

The pressure distributions for multiple pumps can be obtained by superimposing pressure distributions for one pump; the peak pressure for N pumps (N = 2, 3, 4) is N times the pressure for one pump. The resulting pressure distribution is equivalent to N times the pump pressure distribution of one pump. Since superposition holds for multiple pumps and the phases between pumps are unknown, the assumption that all pumps are in phase results in the maximum value of pressure.

The random hydraulic forcing function on the CSB assembly is developed from the valid prototype CVAP test data (Reference 4). The resulting equation for the wide-band white-noise force PSD is expressed as:

$$S_F(\omega) = S_P(\omega) \cdot N \cdot A_C^2$$

Where:

$S_F(\omega)$ = force power spectral density [N^2/Hz (lbf^2/Hz)]

$S_P(\omega)$ = pressure power spectral density $[(N/m)^2/Hz(psi^2/Hz)]$
N = ratio of total surface area to coherence area = A_S/A_C
A_C = coherence area of turbulent pressure fluctuations $[m^2(in^2)]$
A_S = total surface area of component $[m^2(in^2)]$

As shown in Figure 3-3, the surface of the CSB is divided into two regions: Region 1 indicates a portion of cylinder with inlet pipe centerline where relatively larger turbulence load is expected due to high velocity jet impingement. Region 2 corresponds to the rest where the fluid velocity and resulting turbulence intensity is smaller than Region 1.

Figures 3-4 presents RMS pressure PSD on the CSB at 260.0°C(500°F) for each region defined in Figure 3-3. These are derived from the valid prototype CVAP test data (Reference 4). For various temperatures, the pressure PSD in Figures 3-4 is adjusted by the temperature adjustment factor given in Table 3-2 as follows:

$$PSD(T) = PSD[260.0℃(500°F)] \times FTT(T)$$

Where:

$PSD[260.0℃(500°F)]$ = Values read from Figure 3-4
FTT(T) = temperature adjustment factor from Table 3-2

The coherence area is defined as follows:

$$A_C = (D_{RV} - D_{CSB})^2$$

Where:

D_{RV} = inner diameter of RV
D_{CSB} = outer diameter of CSB

Table 3-1 Multiplying Factor on Pump-Induced Pressures on the CSB

TS

Table 3-2 Temperature Adjustment Factor for the PSD Loads on the CSB

TS

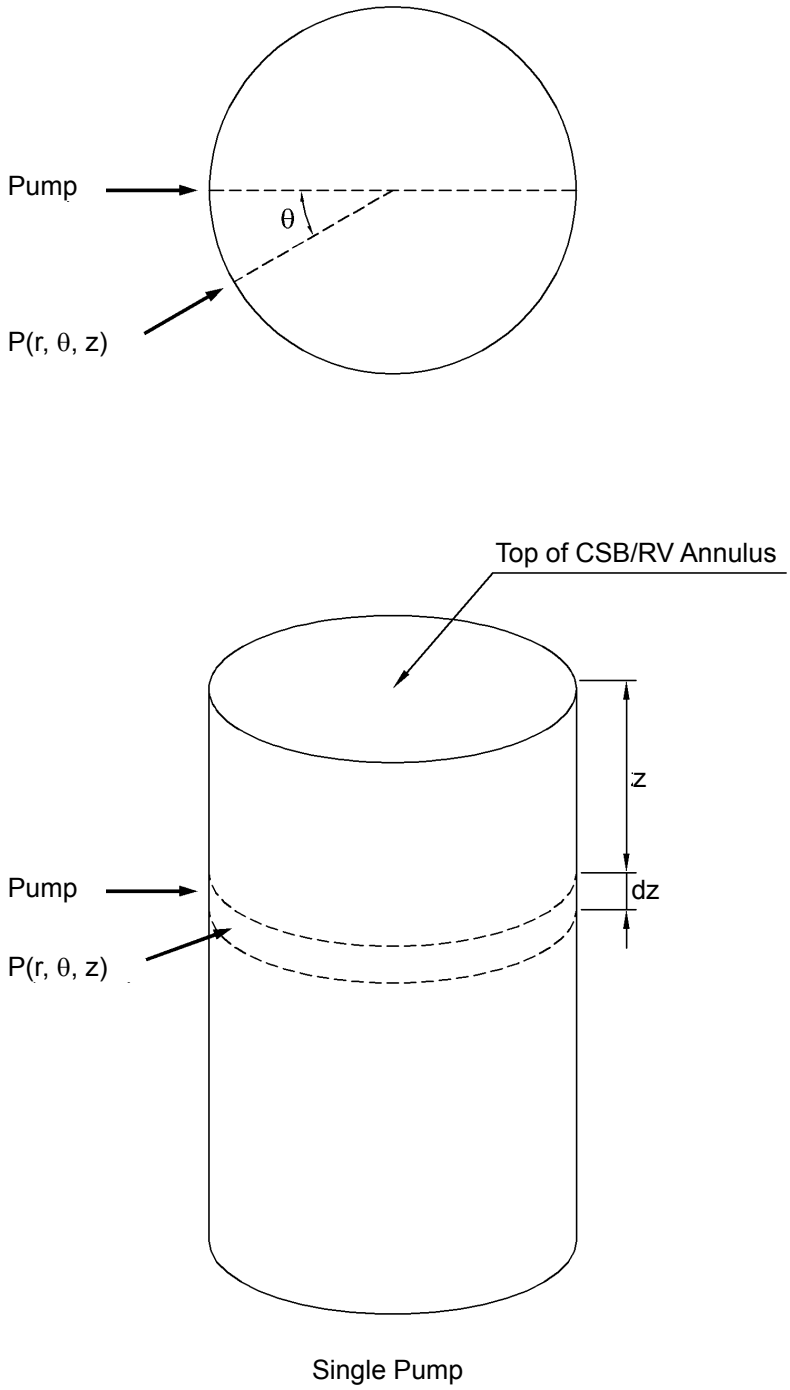

Figure 3-2 Definitions of Pump Azimuthal Locations for the CSB

Figure 3-3 Regions for Pressure PSD on the CSB

Figure 3-4 Pressure PSD on the CSB

3.2.3 Upper Guide Structure

The most significant dynamic force on the upper guide structure (UGS) assembly is the flow-induced forces on the tube bank. The periodic components of these forces could be due to pressure pulsations at harmonics of the pump rotor and blade passing frequency and possible vortex shedding caused by crossflow over the tubes. A series of tests on full size tubes at reactor pressure and temperature conditions indicated no evidence of periodic vortex shedding at the Reynolds Number and turbulence levels expected in the tube bank. Thus the only significant periodic force is that due to pump pulsations. Reactor vibration monitoring test data from the valid prototype (Reference 4) are used to determine the magnitude of these pulsations at the forcing frequencies. To consider coupling effects, pump pulsation loads on the fuel alignment plate (FAP), UGS support plate (UGSSP) and UGS barrel are also computed.

Pump-induced loads on the components are derived at two conditions as follows.

- With the axis of the pressure wave perpendicular to the component
- With the axis of the pressure wave parallel to the component

Figure 3-5 shows the two conditions for the pump-induced loads.

When the sound pressure wave axis is perpendicular to the axis of the component, the pressure pulsation is calculated using the following equation assuming that the pump-induced acoustic pulsation is expressed in terms of the independent propagation of sinusoidal components:

[ ] TS

When the pressure wave axis is parallel to the axis of the component, as shown in Figure 3-5, and the magnitude of the one-half wave length can be comparable to the diameter of the component (such as the FAP), the pump-induced load on the component can be sizable.

The fluctuating pressure, P_{MAX}, is a measure of the pump-induced pressure load acting on one face of the component. Thus, the hydraulic load is provided in maximum pressure pulsation on the surface of the component with the multiplying factor for conservatism included:

[ ] TS

The one-half wave length for the pressure fluctuation is determined as follows:

[ ] TS

Maximum design pump-induced loads on the FAP, UGSSP, and CEA guide tubes are presented in Table 3-3 for six forcing frequencies that are derived from the measured data at UGSSP and CEA guide tube in the valid prototype CVAP (Reference 4). The loads represent peak loads for the four-pump operation condition. These loads are applicable to the pre-core and the post-core conditions. Since the mode shapes of the pressure fluctuations are not well defined, the more adverse of the two types of load (perpendicular and parallel) is to be used for sizing the UGS components.

Pressures were measured on the CEA guide tube in the valid prototype CVAP program (Reference 4). These test results are used to derive the pressure PSD for the UGS. Figure 3-6 shows the pressure PSD for the FAP, UGSSP, UGS barrel, and CEA guide tubes at 260.0°C (500°F).

The relevant coherence lengths are shown in Table 3-4. Since the pressure PSDs are based on 260.0°C (500°F), adjustment is made for other temperatures using the factors in Table 3-2 by using the methodology described in Subsection 3.2.2.

The coherence area, A_C, for the turbulence pressure fluctuations on the UGS components is given by:

$$A_C = L_x L_z$$

Where:

L_x = lateral coherence length
L_z = axial coherence length

Table 3-3 Pump-Induced Loads on the UGS Tube Bank

TS

Table 3-3 Pump-Induced Loads on the UGS Tube Bank (Continued)

TS

Table 3-3 Pump-Induced Loads on the UGS Tube Bank (Continued)

TS

Table 3-4 Coherence Lengths for the UGS Components

TS

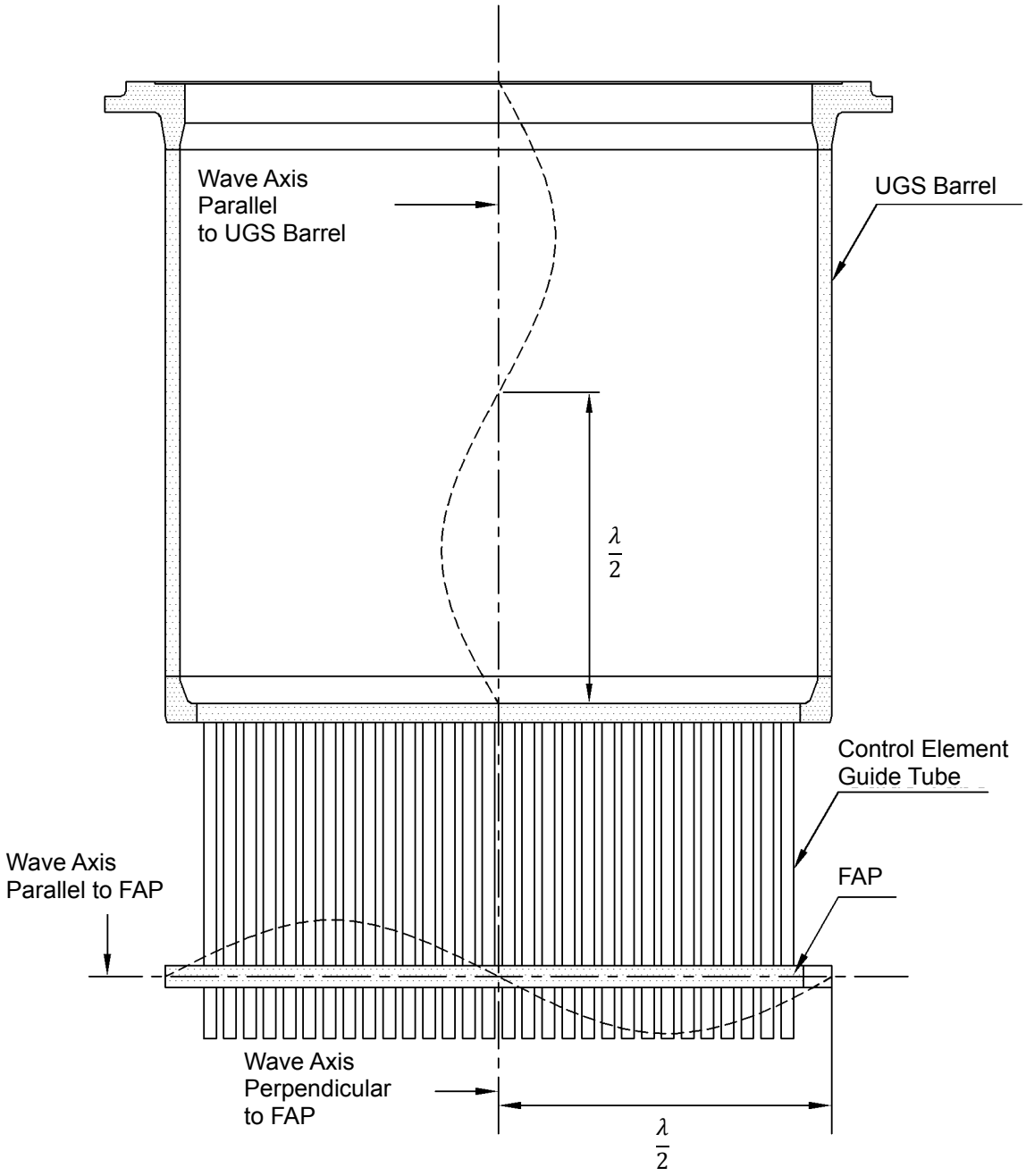

Figure 3-5 Orientation of Pump-Induced Loads on the UGS Assembly

Figure 3-6 Pressure PSD on the UGS Assembly

3.2.4 Lower Support Structure

The derivation of pump-frequency-related loads is accomplished using the valid prototype I CVAP test data (Reference 4) which were obtained at the ICI guide tube location. The pressure fluctuation acting on the LSS components is calculated using the methodology described in Subsection 3.2.3. The pump-induced loads on the LSS components are given in Table 3-5 at the six forcing frequencies. Since the mode shapes of the pressure fluctuations are not well defined, the more adverse of the two orientations of load (perpendicular and parallel to bottom plate), as shown in Figure 3-7, is to be used for sizing the LSS components.

Measured pressures from the valid prototype CVAP test data are used to derive the pressure PSD for the LSS components. Random forcing functions are presented in Figure 3-8 at 260.0°C (500°F). For other temperatures, the pressure PSD in Figure 3-8 is multiplied by the temperature adjustment factor given in Table 3-2.

The coherence area, A_C, is conservatively taken to be:

$$A_C = L_x L_z$$

Where:

L_x = lateral coherence length = pitch of LSS beams
L_z = axial coherence length = depth of LSS beams

Table 3-5 Pump-Induced Loads on the LSS

TS

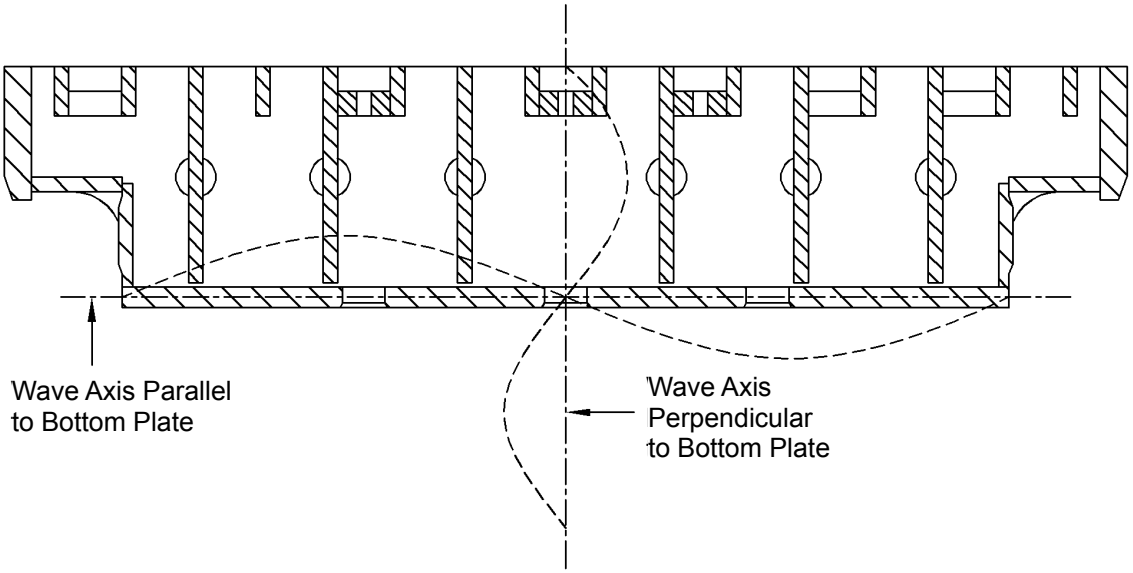

Figure 3-7 Orientation of Pump-Induced Loads on the LSS

TS

Figure 3-8 Pressure PSD on the LSS

3.2.5 In-Core Instrument Nozzle Assembly

The most significant flow-induced loading on the ICI nozzle assembly is on the instrument tubes and the skewed beam supports for the instrument plate. These structures are excited by periodic and/or random flow-induced forces. The periodic component of this loading is due to pump-related pressure fluctuations and vortex shedding caused by crossflow.

Assuming that regular vortex shedding occurs, the vortex shedding forces are expressed as:

$$F = C\frac{\rho V^2}{2}\sin(2\pi f_{VS}t)\,A_p$$

Where:

C = lift/drag coefficients
V = approach velocity
ρ = fluid density
f_{VS} = vortex shedding frequency = $St\frac{V}{D}$
St = Strouhal number
D = tube diameter
A_p = projected or frontal area
t = time

The magnitude of the drag coefficient and the Strouhal number are taken in a conservative way. The lift coefficient is taken to be equal to the drag coefficient. The maximum force is computed for the maximum value of $\sin(2\pi f_{VS}t)$ = 1.0.

$$F_{MAX} = C\frac{\rho V^2}{2}A_p$$

Vortex shedding frequencies and force on the ICI guide tube and support columns are provided in Table 3.2-6. Calculations were made for the outermost ICI tube, which is subjected to the full impact of the high approach velocities from the flow skirt. For other temperatures, Table 3-7 can be used to adjust the relevant loads.

Pump-induced periodic loads on the ICI guide tubes and support columns are given in Table 3-8 for the four-pump operation conditions, which are calculated using the methodology described in Subsection 3.2.3.

The random turbulence forcing function is derived from the valid prototype CVAP test data (Reference 4), is shown in Figure 3-9 at 260.0°C (500°F), and is applied over every ICI guide tube and support column. When required for other temperatures, the pressure PSD is adjusted using Table 3-7.

The coherence area, A_C, is taken to be:

$$A_C = L_\theta L_z$$

Where:

L_θ = circumferential coherence length = $\pi D/4$
L_z = axial coherence length = $D/2$
D = outside diameter of the ICI guide tube and support column

The coherence area of the ICI guide tube is: $A_C = \frac{\pi D^2}{8}$

Table 3-6 Vortex Shedding Loads on the ICI Nozzle Assembly

TS

Table 3-7 Multipliers of Loads on the ICI Nozzle Assembly

TS

Table 3-8 Pump-Induced Loads on the ICI Nozzle Assembly

TS

TS

Figure 3-9 Pressure PSD on the ICI Nozzle Assembly

3.2.6 Core Shroud

The periodic loads on the vertical panels of the core shroud are derived from the valid prototype CVAP test data (Reference 4). Table 3-9 shows maximum pump-induced lateral loads for the four-pump operation conditions. The loads correspond to the pressure wave and are parallel to the plane of the vertical panels. Half-wave lengths are also presented in Table 3-9.

The random turbulence load is derived from the valid prototype CVAP test data (Reference 4). Figure 3-10 shows the pressure PSD for the core shroud vertical panel at 260.0°C (500°F). This PSD applies over the entire inside surface of the core shroud. For other temperatures, the PSD in Figure 3-10 is adjusted by using the temperature adjustment factors in Table 3-2 and the method described in Subsection 3.2.2.

The coherence area, A_C, is taken to be:

$$A_C = L_x L_z$$

Where:

L_x = circumferential coherence length = horizontal width of core shroud panels
L_z = axial coherence length = minimum gap between outermost fuel rod and inner surface of panel

Table 3-9 Pump-Induced Loads on the Core Shroud

TS

Figure 3-10 Pressure PSD on the Core Shroud

3.2.7 Inner Barrel Assembly

The pump-induced maximum lateral loads on the panels and the cylinders of the inner barrel assembly (IBA) are provided in Table 3-10 for the cases in which the axis of the pressure fluctuations is parallel to the plane of the vertical panels. Loads are defined for each of pump-forcing frequency for a range of operating temperatures for four-pump operation conditions. The load values represent maximum values. Table 3-10 also provides the one-half wave lengths, λ/2, for the pressure fluctuations.

The flow-induced random turbulence loads on the surfaces of the IBA at T= 260.0°C (500°F) are presented in Figure 3-11. The PSD in Figure 3-11 should be adjusted for different temperatures by using the temperature adjustment factors in Table 3-2 with the method described in Subsection 3.2.2.

The coherence area, A_C, for the turbulence pressure fluctuations on the surfaces (vertical plates and tubes) is given by:

$$A_C = L_\theta L_z$$

Where:

L_θ = circumferential coherence length = perimeter of tube cell
L_z = axial coherence length = diameter of vertical tubes
= diagonal width of “square” tube cells

The coherence area, A_C, for the turbulence pressure fluctuations on the upper cylinder is given by:

$$A_C = L_\theta L_z$$

Where:

L_θ = circumferential coherence length = perimeter of upper cylinder / 4
L_z = axial coherence length
= maximum radial gap between outer diameter of upper cylinder and inner diameter of vessel head

The coherence area, A_C, for the top plate is given by:

$$A_C = L_x L_y$$

Where:

L_x, L_y = lateral coherence length

Table 3-10 Pump-Induced Loads on the IBA

TS

Figure 3-11 Pressure PSD on the IBA

3.3 Calculation of the Structural Response

The finite element models of the APR1400 RVI components are developed to predict the structural responses to the dynamic hydraulic loads and estimate possible vibrations. These models are developed with a consideration of the characteristics of the loads such as directions of the loads and coherence areas of random turbulence loads.

The modal analyses are performed to determine the dynamic characteristics of the structures and obtain the modal responses for the dynamic analyses.

The pump pulsation analysis is performed through the harmonic analysis because the loads are periodic. The responses of the RVI components for pump pulsation loads are calculated for the forcing frequencies of 20, 40, 120, 240, 360, and 480 Hz, respectively, in Subsection 3.2. In addition, the RVI response analysis is performed to the extent of [ ]^{TS} from the six pump frequencies to account for the Type 1 and Type 2 loss of load events, respectively. The Type 1 loss of load event is defined as a [ ]^{TS} pump overspeed condition where turbine generator controls function properly during a loss of load event and the Type 2 loss of load event is defined as a [ ]^{TS} pump overspeed condition where turbine generator controls do not function during a loss of load event. The analyses are performed by considering the response of the model in terms of the in-phase response and the out-of-phase response. The complete response to each forcing frequency is the square root of the sum of the squares (SRSS) of the in-phase and out-of-phase responses. The total response is obtained by summation of the responses for all forcing frequencies.

The response for the random turbulence loads is obtained through the statistical approach because the random turbulence loads cannot be estimated using the deterministic method. The random vibration analysis is performed using the PSD curve described in Subsection 3.2. The analyses are carried out under hot and cold normal operating conditions, and Type 1 and Type 2 loss of load events that consider pump overspeed conditions. The maximum responses are calculated by multiplying by 3.0 to account for statistical uncertainties.

The structural materials of the RVI components are Type 304 austenitic stainless steel. The material properties of this austenitic stainless steel used for the RVI modeling are determined based on Part D, Section II of Reference 10. The structural damping of [ ]^{TS} is used for the response analyses.

3.3.1 Core Support Barrel

The natural frequencies and mode shapes of the CSB are obtained using the axisymmetric shell model shown in Figure 3-12. The structure is fixed at the CSB upper flange to determine the beam modes and frequencies. The shell modes and frequencies are found by considering the upper flange fixed and the lower flange pinned. Generalized masses, based on mode shapes and the mass matrix, are calculated for each CSB mode of vibration. Modal participation factors, based on the mode shapes and the predicted periodic forcing functions, are calculated for each mode and forcing function. The frequencies in water are computed using a continuum approach to the hydrodynamic effects. The natural frequencies of the CSB under the in-air and the in-water conditions at 290.6°C (555°F) are presented in Table 3-11. The typical beam and shell mode shapes of the CSB are shown in Figure 3-13.

The normal mode method in “Dynamic Stress Analysis of Axisymmetric Structures under Arbitrary Loading” (Reference 6) is used to obtain the structural responses of the CSB for the periodic forcing functions described in Subsection 3.2.2. The small deflection theory is applicable to the CSB, which is assumed to be a thin shell. Since the governing equation of the CSB is linear, the superposition of responses for various loading is applicable to the CSB. After the response of each forcing frequency is calculated, total responses of the CSB for pump pulsation loads are algebraically summed by superimposing the responses of the forcing frequencies. The maximum stresses of the CSB are shown in Table 3-12.

The CSB responses for normal operating random pressure fluctuations (see Subsection 3.2) caused by turbulence flow in the coolant annulus between the RV and CSB are calculated using the commercial finite element program, ANSYS (Reference 5). The lumped mass beam model is used as shown in Figure 3-14 to determine the CSB responses for the random excitation. The stiffness and mass distribution of the lumped mass beam model are determined using the cross sectional properties. The nodes are spaced based on the coherence length in axial dimensions. The model uses the equivalent density including the added mass to account for the presence of water, and finally the natural frequency is adjusted to the modal analysis results by a rotational spring at the upper flange. The PSD is used for input of random turbulence loads. Two PSDs of the random pressure fluctuations in Figures 3-3 and 3-4 are applied. One of them is applied to the inlet nozzle region (PSD #2 for Region 2) and the other is applied to the remainder (PSD #1 for Region 1) of the CSB as shown in Figure 3-14. The random vibration analysis is performed using the modal analysis results in water at the temperatures of 37.8°C (100°F) and 290.6°C (555°F). The maximum displacements and stresses for random pressure fluctuations caused by turbulence flow are summarized in Table 3-13.

Table 3-11 Natural Frequencies of the CSB

TS

Table 3-12 Maximum Stresses of the CSB for Pump Pulsation Loads

TS

Table 3-13 Maximum Displacements and Stresses of the CSB for Random Turbulence Loads

TS

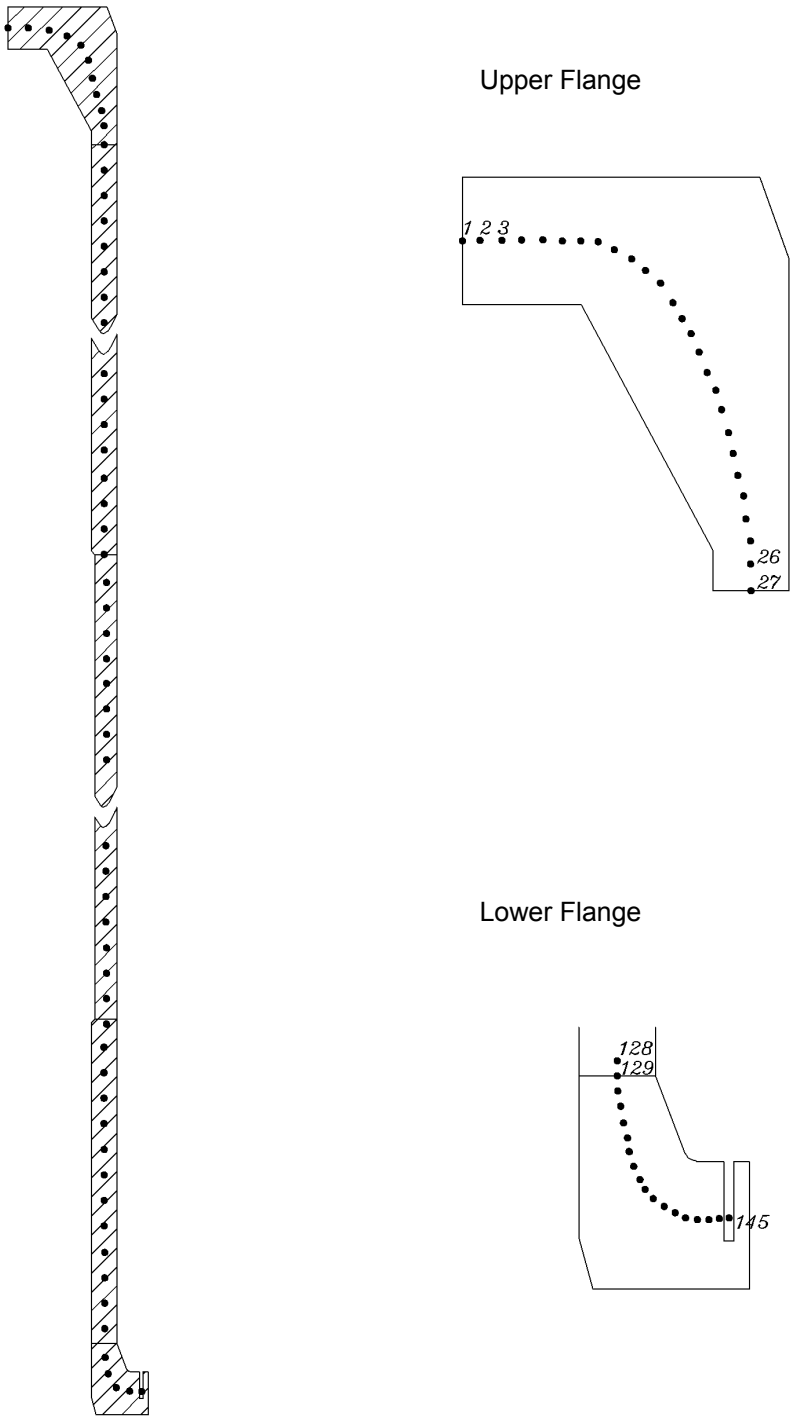

Figure 3-12 Axisymmetric Model of the CSB

Figure 3-13 Typical Mode Shapes of the CSB

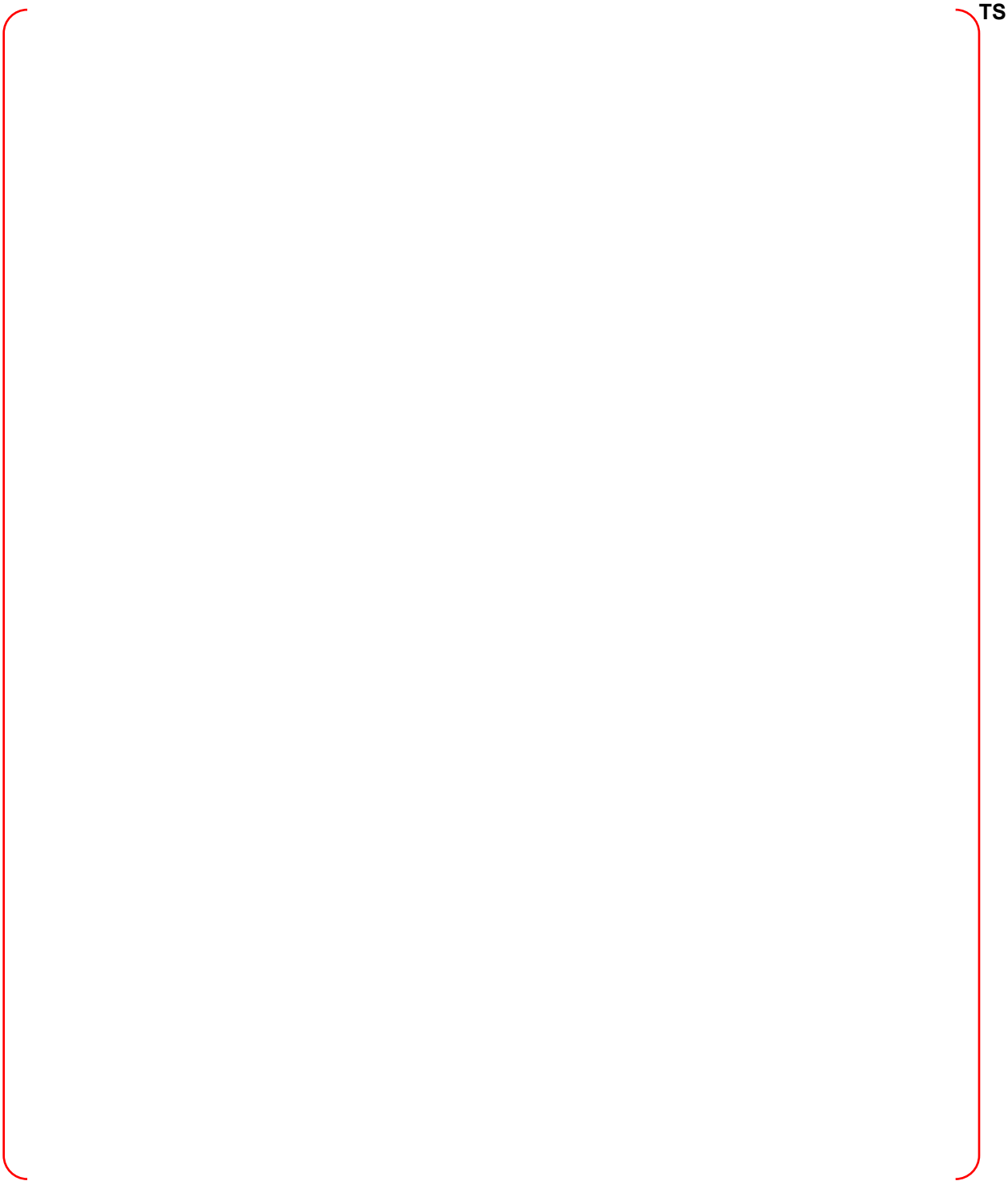

Figure 3-14 Lumped Mass Beam Model of the CSB

3.3.2 Upper Guide Structure

The upper guide structure (UGS) assembly consists of the UGS barrel, IBA, and tube bank. The individual structural analyses of the IBA and the tube bank are presented in Subsections 3.3.7 and 3.3.3, respectively. This section presents the method of obtaining the behavior of the UGS assembly including a consideration of the interaction between the components. The analytical model of the UGS assembly is developed as a lumped mass beam model using the ANSYS finite element program (Reference 5), and shown in Figure 3-15. This model consists of lumped masses and beam elements. The stiffness and mass distribution of the lumped mass beam model are determined using the cross sectional properties of the structure. The spacing between nodes is chosen to consider the coherence length specified for random loads. The CSB is also included in the model by boundary conditions. The hydrodynamic couplings are included in the model to account for the annulus effects between the CSB and UGS and between the UGS and IBA, as shown in Figure 3-15.

The UGS model contains a rotational spring. The stiffness of the spring is determined to match the first natural frequency of the UGS model with the CVAP result for the valid prototype. The nodes of the IBA model include added masses for the weight of contained water of the IBA. The moment of inertia of the IBA model is determined to match the first natural frequency obtained from the modal analysis of the detailed IBA model (see Subsection 3.3.7). The nodes of the tube bank model also include added masses for the weight of contained water of CEA guide tubes. The FAP and tube extensions are represented as a concentrated mass in the model. The rotation of the FAP around the out-of-the-plane axis is controlled by a rotational spring.

The modal analysis is performed using this model, and then the dynamic response analyses for pump pulsation and random turbulence loads are performed for the UGS assembly. The natural frequencies and modal characteristics of this model are provided in Table 3-14.

The pump pulsation response analysis is performed using the harmonic analysis by applying the pump pulsation pressure loads to the inner surface of the UGS barrel, and the outer surfaces of the IBA and the CEA guide tubes in the tube bank (see Subsection 3.2.3).

The stress analyses for random turbulence loads are performed using the PSD in Figure 3-6. The PSDs in Figure 3-6 are applied to the UGS barrel, IBA, and the CEA guide tubes in the tube bank.

The maximum deflections at the UGS flanges due to the random turbulence and pump pulsation analyses are summarized in Table 3-15.

Table 3-14 Modal Analysis Results of the UGS Assembly

TS

Table 3-15 Maximum Deflections of the UGS Flanges

TS

TS

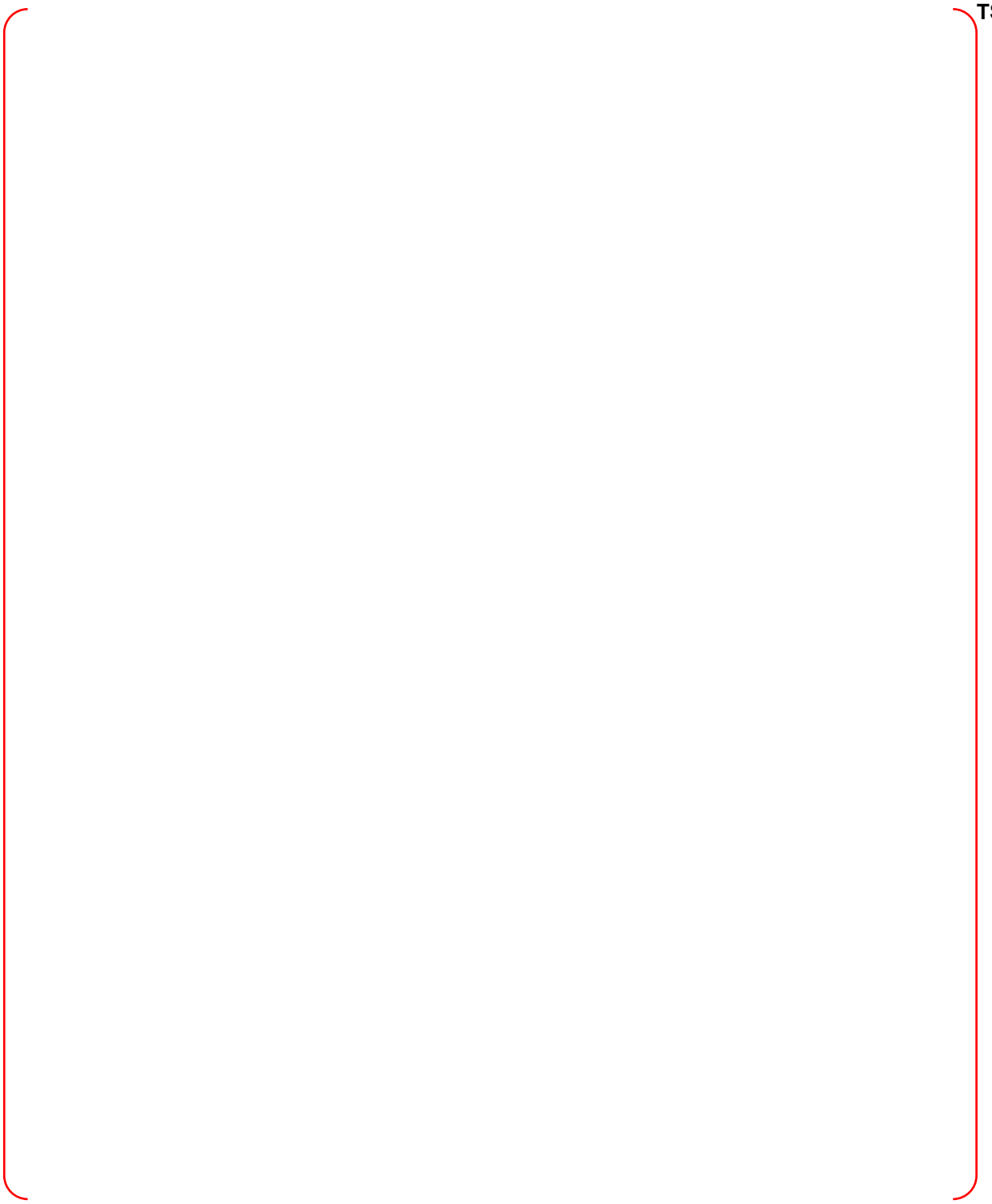

Figure 3-15 Lumped Mass Beam Model of the UGS Assembly

3.3.3 Tube Bank Assembly

The tube bank assembly consists of the UGS support plate (UGSSP) having a [ ]^{TS} thick flat plate, CEA guide tubes, FAP having a [ ]^{TS} thick flat plate, and the guide tube extensions (GTEs). The half symmetric finite element model of the tube bank assembly is generated using the ANSYS finite element program (Reference 5) and shown in Figure 3-16. For the finite element modeling, beam elements are used to define the CEA guide tubes including the GTEs. The stiffness and mass distribution of the beam elements are determined using the cross sectional properties. The spacing between nodes is determined to be sufficiently close to appropriately represent the mode shapes of the CEA guide tubes. To account for the hydrodynamic effect, the model uses the equivalent density including the added mass. Shell elements are used to represent the FAP and the UGSSP with many flow holes. The tube bank assembly is supported at the periphery of the UGSSP by the UGS lower flange. All degrees of freedom except one rotational degree of freedom are fixed at the intersection of the UGSSP and the UGS lower flange. One rotational degree of freedom of each node at the fixed position is connected to a rotational spring, which simulates the boundary condition of the UGS barrel and lower flange.

The modal characteristics of the tube bank assembly are determined before the dynamic response analyses for random turbulence loads and pump pulsation loads. The modal characteristics including natural frequencies of the tube bank assembly are summarized in Table 3-16.

The harmonic response analysis is performed using the pump pulsation loads described in Subsection 3.2.3. The pump pulsation loads are applied to all shell elements in the UGSSP and FAP, and all of the guide tubes. The pump pulsation loads on the guide tubes are specified in the lateral direction parallel to the plane of symmetry by applying the loads to the projected area of the tube associated with each node. During Type 1 and Type 2 loss of load events, the magnitudes of the pressure loads do not change, but the frequencies change. The frequency range of Type 1 loss of load event vary [ ]^{TS} the nominal forcing frequency, and the frequency range of Type 2 loss of load event vary [ ]^{TS} the nominal forcing frequency. The dynamic responses of the tube bank assembly for the periodic pump pulsation loads are summarized in Table 3-17.

The random vibration analysis is performed using the PSD loads described in Subsection 3.2.3. The PSD loads in Figure 3-6 are applied to the UGSSP, FAP, and the CEA guide tubes. The dynamic responses of the tube bank assembly for the random turbulence loads are summarized in Table 3-18.

Table 3-16 Modal Analysis Results of the UGS Tube Bank

TS

Table 3-17 Maximum Stresses of the UGS Tube Bank to Pump Pulsation Loads

TS

Table 3-18 Maximum Stresses of the UGS Tube Bank to Random Turbulence Loads

TS

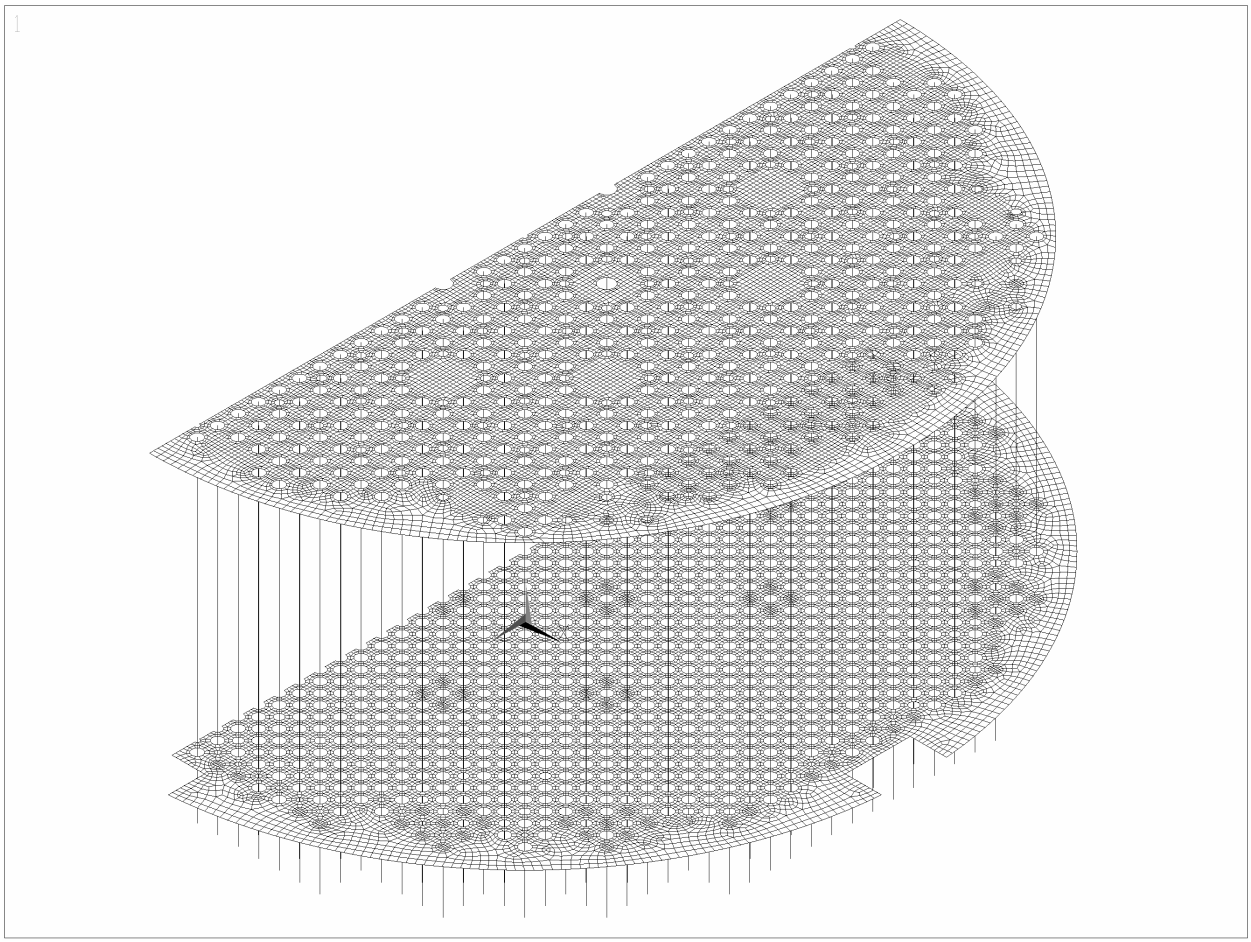

Figure 3-16 Finite Element Model of the UGS Tube Bank

3.3.4 Lower Support Structure

A half-symmetric finite element model of the lower support structure (LSS) is developed as shown in Figure 3-17. The LSS cylinder is fixed at the interface with the CSB lower flange. Hydrodynamic effects including core mass are considered by adding concentrated masses at the associated nodes. All LSS components are modeled with shell elements of the ANSYS program (Reference 5). For the bottom plates and raised bottom plates, equivalent elastic properties are used to account for hole effects described in Section III, Appendix A-8000 of Reference 10.

The modal analysis is performed to compute the natural frequencies of the LSS. The results are summarized in Table 3-19 and are used in determining dynamic responses to the pump pulsation and random turbulence loads.

The response of the LSS for pump pulsation loads (see Subsection 3.2.4) is determined by mode superposition harmonic analysis. The expansion pass of the mode superposition harmonic analysis is computed using the SRSS of in-phase and out-of-phase. The resultant stresses of the bottom plates and raised bottom plates are converted to actual stresses for the hole effects (see Section III, Appendix A-8000 of Reference 10). The maximum stress intensities and locations for pump pulsation loads are provided in Table 3-20.

The stress analyses for random turbulence loads are performed using the PSD in Figure 3-8. The maximum stress intensities and locations for random turbulence loads are provided in Table 3-20.

Table 3-19 Natural Frequencies of the LSS

TS

Table 3-20 Maximum Stress Intensities of the LSS

TS

TS

Figure 3-17 Finite Element Model of the LSS

3.3.5 In-Core Instrument Nozzle Assembly

The in-core instrumentation (ICI) nozzle assembly consists of ICI nozzles, an ICI nozzle support plate, gussets, and tripods. The ICI nozzle assembly model is developed using the ANSYS program (Reference 5) and shown in Figure 3-18. The ICI nozzles, gussets, and tripods are modeled using beam and pipe elements. The ICI nozzle support plate is modeled using shell elements with many flow holes.

Modal analyses are performed for the structure in-air and in-water conditions. The number of modes is determined to sufficiently cover the dynamic characteristics of the ICI nozzle assembly. Table 3-21 shows the first 50 natural frequencies of one horizontal direction for in-water condition, which are similar to those of the other horizontal direction.

The two types of periodic loads for the response analyses of the ICI nozzle assembly are vortex shedding and pump pulsation loads, as described in Subsection 3.2.5. The responses of the ICI nozzle assembly to the vortex shedding loads and pump pulsation loads are computed using harmonic analyses. The vortex shedding loads are applied to the nozzles at the circumferential perimeter because the hydraulic analysis results of the vortex loads show that vortex loads at inner nozzles are much lower than those at the outer nozzles. Table 3-22 summarizes the stress analysis results for the ICI nozzle assembly. The maximum stress occurs at the gusset connected to the ICI nozzles and the ICI nozzle support plate for pump pulsation loads.

The random vibration analysis for the random turbulence loads is performed using the PSD curve in Figure 3-9. The results of the responses for random turbulence loads are listed in Table 3-22.

Table 3-21 Modal Analysis Results of the ICI Nozzle Assembly

TS

Table 3-22 Maximum Stress Intensities of the ICI Nozzle Assembly

TS

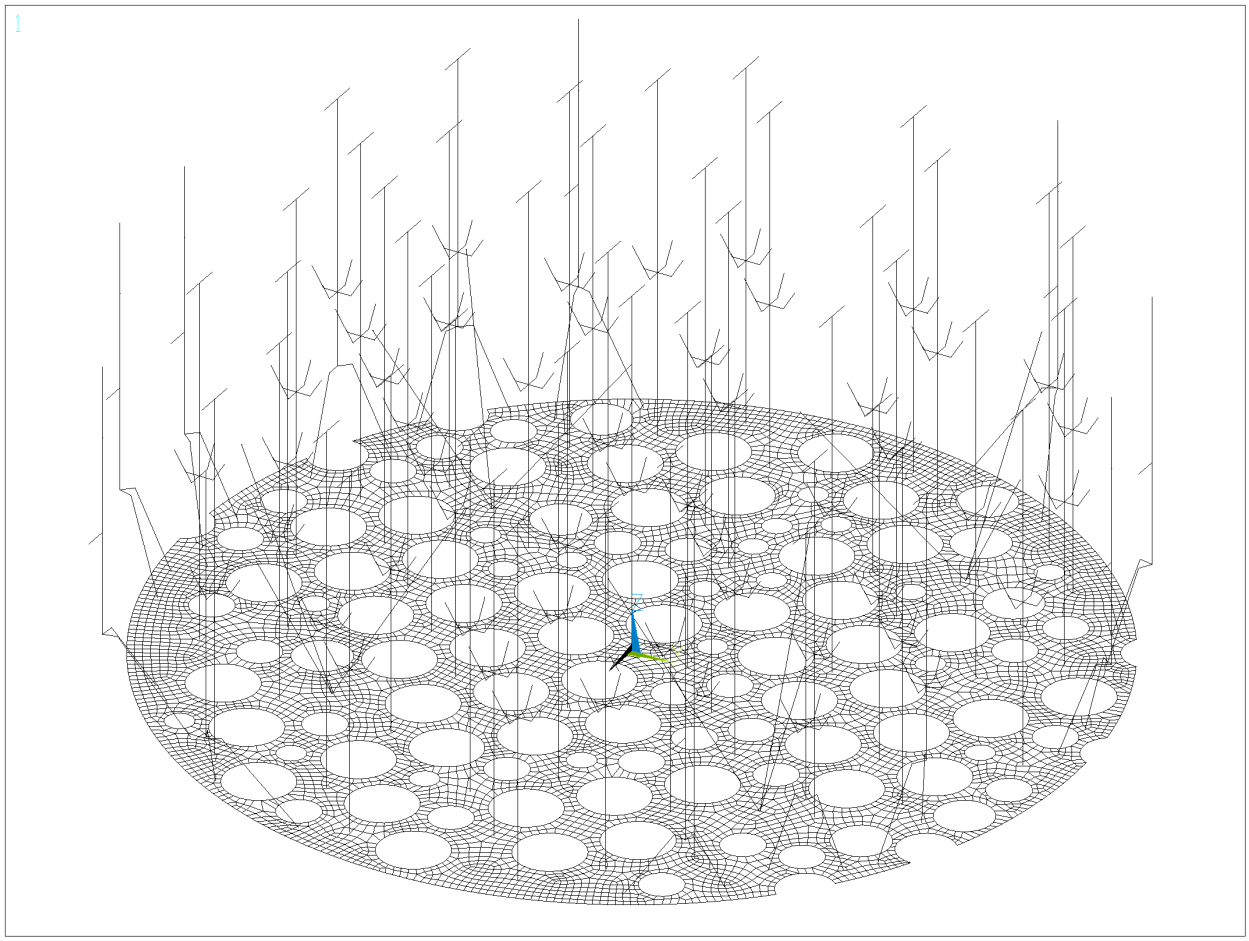

Figure 3-18 Finite Element Model of the ICI Nozzle Assembly

3.3.6 Core Shroud

The core shroud (Figure 3-19) provides an envelope for the core and consists of top and bottom plates, shroud plates, ribs, braces, and rings. The natural frequencies of the core shroud and its responses for dynamic loads are calculated by classical hand calculations using mathematical formulas.

The shroud plates and ribs can be considered as simply supported beams and plates.

The natural frequency of simply supported beam is calculated using the following formulas (Reference 9):

[ ] TS

For the conservative results, the pump pulsation loads (see Subsection 3.2.6) are simply applied to the shroud plate as a uniform load because most of the half-wave lengths are greater than the modeled plate height. The maximum bending moment occurs at the center of the beam and is calculated by the following formula:

[ ] TS

The maximum stress at the center of the shroud plate is calculated using the following formula for a simply supported beam:

TS

The natural frequency of simply supported rectangular plate is calculated by the following formulas (Reference 9):

TS

The maximum stresses at the center of shroud plate for pump pulsation and random turbulence loads are calculated using the following formula for a simply supported plate (Reference 8):

TS

The total response of the shroud plate for random turbulence loads is obtained by multiplying by 3.0 to account for the statistical uncertainties.

The maximum stress intensities for pump pulsation and random turbulence loads are summarized in Table 3-23, which occur at the center of the large shroud plate from the bottom plate to the lowest ring.

Table 3-23 Maximum Stress Intensities of the Core Shroud

TS

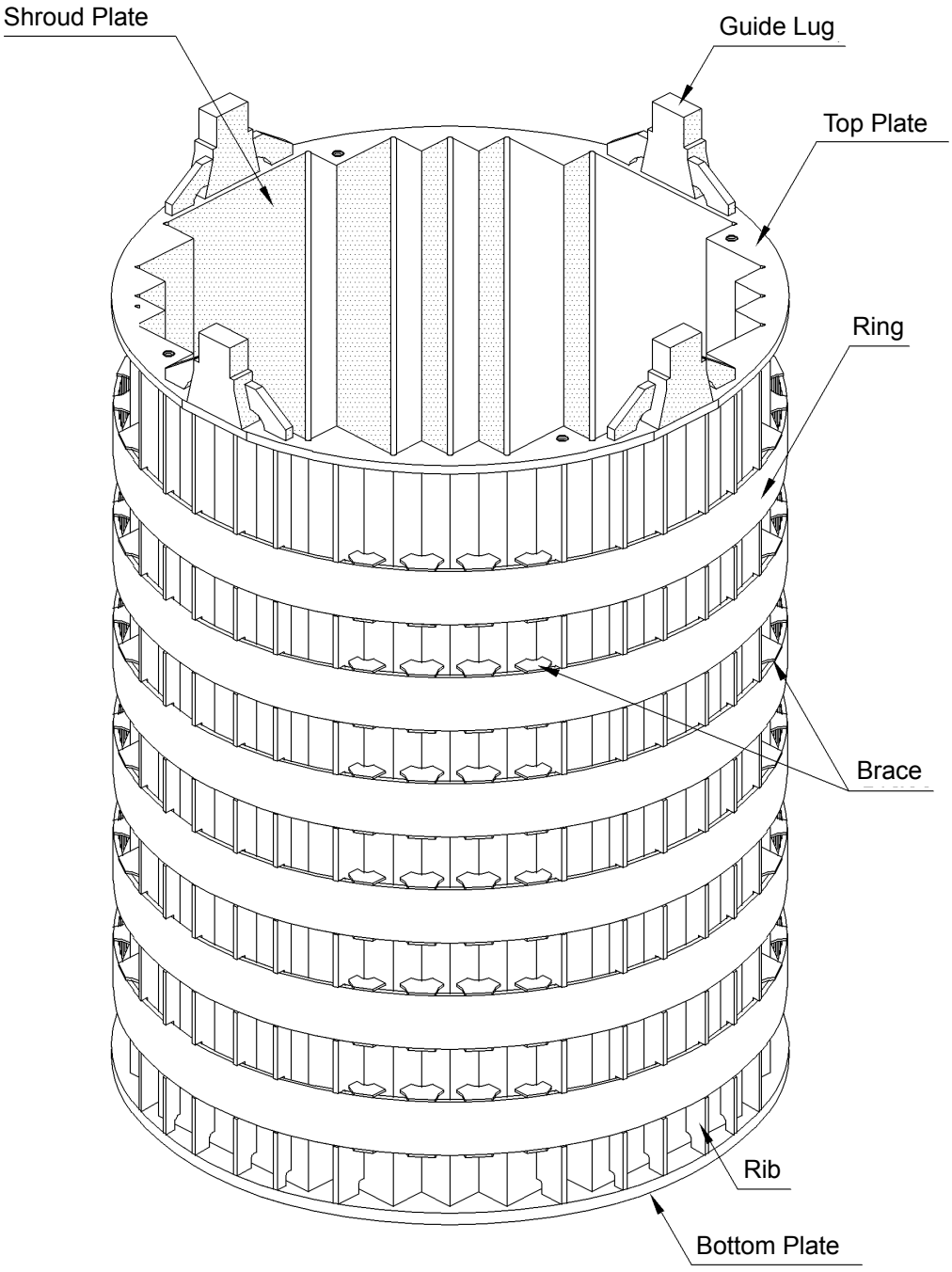

Figure 3-19 Core Shroud

3.3.7 Inner Barrel Assembly

The inner barrel assembly (IBA) consists of shroud tubes, webs, a top plate, a flange, and cylinders. The IBA flange is welded to the top of the UGS flange. The model is developed using the ANSYS code (Reference 5). The shroud tubes, webs, cylinders, and most parts of the top plate are modeled using shell elements, and the flange and the rim regions of the top plate are modeled using solid elements. Figure 3-20 shows the half-symmetric model for the IBA.

Modal analyses are performed for the structure in air and in water conditions. The number of modes is determined to sufficiently cover the dynamic characteristics of the IBA. Table 3-24 shows the first 50 natural frequencies of one of the horizontal directions analyzed for in-water conditions, which is similar to those of the other horizontal direction.

The pump pulsation loads applied to the IBA are described in Subsection 3.2.7. The stress analyses for pump pulsation loads are performed using the harmonic analysis. The vertical loads are applied to the top plate including the fingers. The horizontal loads are applied to the cylinders, tubes, and webs.

The stress analyses for random turbulence loads are performed using the PSD in Figure 3-11.

Table 3-25 summarizes the stress analysis results for the IBA and shows the membrane stresses (Pm) and membrane plus bending stresses (Pm+Pb) for each part of the IBA. The maximum stress occurs at the top plate and outer tubes.

Table 3-24 Modal Analysis Results of the IBA

TS

Table 3-25 Maximum Stress Intensities of the IBA

TS

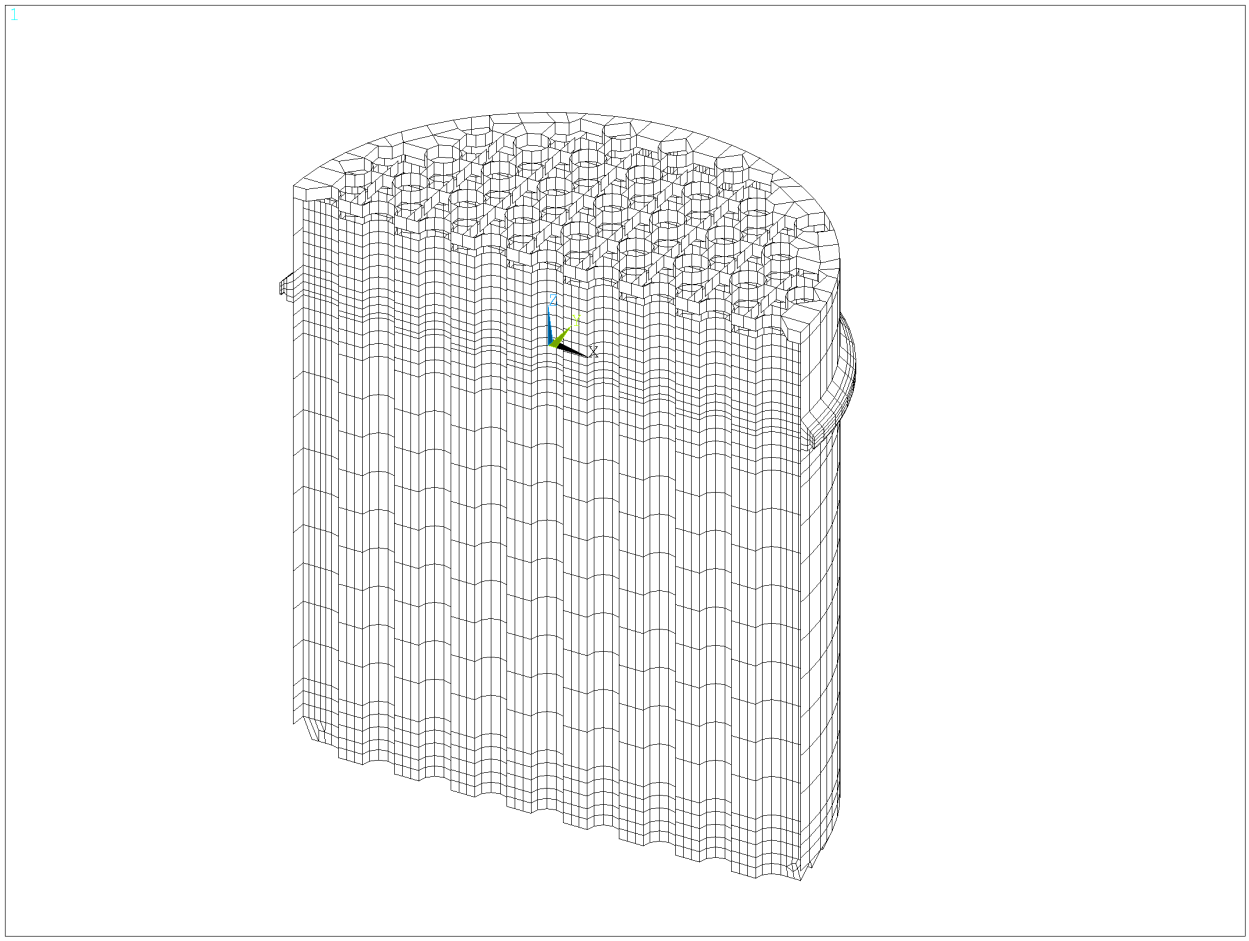

Figure 3-20 Finite Element Model of the IBA

3.4 Evaluation of the Results

The evaluation of the analysis results of the APR1400 RVI is performed. The evaluation method verifying the structural integrity of the RVI is in accordance with ASME Code Section III, Subsection NG-3000 (Reference 10). Table 3-26 shows the high cycle fatigue evaluation for the RVI, which uses only the responses to the periodic and random dynamic loads. The evaluation of the results of the APR1400 RVI CVAP shown in Table 3-26 demonstrate that the APR1400 RVI meet the required fatigue limits.

Table 3-27 shows the maximum stress intensity and fatigue usage factors of the APR1400 RVI from the design report for the Shin-Kori Nuclear Power Plant Unit 3, one of the APR1400 reactors in the ROK (Reference 11). The evaluation in Table 3-27 is based on all responses due to static and dynamic loads including thermal and flow-induced loads.

Table 3-26 High Cycle Fatigue Evaluation for Maximum Stress Regions

TS

Table 3-27 Maximum Stress Intensities and Fatigue Usage Factors

TS

3.5 Bias Errors and Uncertainties of the Analysis

The dimensions used for developing the RVI analytical models are based on the design drawings. The material properties of coolant water and structures such as density and elastic modulus are controlled by the operating temperatures, and the temperatures vary over the structures during normal operation. Thus, the material properties based on the representative temperature are used for each structure. The effects of these bias errors are can be ignored.

For the case using finite element models, some analytical models may not completely incorporate the detailed design features of the real structure. However, the dynamic characteristics of the real structures are sufficiently represented without the detailed design features. In addition, there are manufacturing tolerances of the geometry of the structures, but the analytical models use nominal dimensions to simulate the best estimate results.

For the structural analysis of the APR1400 RVI, the forcing frequencies of pump pulsation loads are extended to compensate for the bias errors and uncertainties of analysis models and loads. Although the pump overspeed conditions at the loss of load events do not last long, all of the RVI components are analyzed to the extent of [ ]^{TS} of the nominal frequency. In addition, some of the RVI components are analyzed with the extended frequency range up to the [ ]^{TS} to account for the uncertainties. Because turbulence loads have a random and statistical nature with wide spread forcing frequencies, the maximum responses are multiplied by 3.0 to account for these uncertainties. All of the hydraulic loads are applied to the RVI components with conservatism resulting in conservative responses.

3.6 Adverse Flow Effects

The hydraulic forcing functions applied to the APR1400 RVI are based on the CVAP results of the valid prototype, and the results of the evaluation show that the APR1400 RVI have the same dynamic characteristics as the valid prototype. In addition, no excessive displacement or damage was reported in the measurement and inspection programs of the valid prototype RVI.

As described in Section 1, many 1000 MWe reactors with non-prototype RVI whose valid prototype is Palo Verde Unit 1 are currently operating in the ROK. However, no adverse flow effects due to flow-induced vibration on the RVI of the reactors in the ROK, as well as on the valid prototype, have been reported.

Shin-Kori Nuclear Power Plant (SKNPP) Unit 3, one of the APR1400 reactors, recently finished its hot functional tests including CVAP without any evidence of adverse effect. The baseline CVAP inspection and post HFT inspection of the SKNPP Unit 3 RVI was conducted. The detailed inspections of the RVI revealed no evidence of loose parts, debris, abnormal corrosion products, structural distortion or displacement of parts due to the HFT. There were no deleterious effects of vibration at clamped or supporting elements.

4 INSPECTION PROGRAM

RG 1.20 (Reference 1) requires that the non-prototype RVI be subjected to at least 10^6 cycles of vibration (i.e., computed at the components minimum significant response frequency), or no less than the valid prototype, to provide reasonable assurance that sufficient visual effects are produced to properly assess the integrity of components.

The inspection and documentation for the APR1400 RVI are completed in two stages. The baseline inspection (pre-hot functional inspection) stage takes place as the RVI components are assembled for the last time after the cold hydraulic test and before the hot functional test (HFT) of the RCS. The post-hot functional inspection stage takes place after the completion of the pre-core HFT of the RVI and during the first disassembly of the RVI following the test. The baseline stage inspection compares the RVI components with the design specifications, standards, and drawings. After the post HFT inspection is completed, the data are compared with the baseline inspection data. The comparison determines the component performance and provides a basis for APR1400 RVI CVAP.

The visual inspection program consists of the inspection of all major load bearing elements, restraint elements, locking components, and contact surfaces within the RVI. The RVI are also inspected for the presence of loose parts or foreign matter.

Based on a minimum post-core natural frequency of [ ] TS for the CSB which is conservatively calculated, [ ] TS of normal operating four-pump primary flow are required as listed in Table 4-1. The pre-core HFT duration for the CVAP test is [ ] TS at four-pump normal operating conditions plus the time required for the test of part loop and other transient operating conditions as listed in Table 4-2. For verification of accomplishment of the minimum cycles of vibration, the individual and collective RCP running times are recorded during the pre-core HFT.

Table 4-1 Required Test Duration for CVAP

TS

Table 4-2 CVAP Test Conditions for the APR1400

TS

5 CONCLUSIONS

The evaluation of the analysis and inspection programs of the APR1400 CVAP, and the predictions and measurements of the valid prototype CVAP lead to the following conclusions:

- The APR1400 reactor is classified as the non-prototype Category I, with Palo Verde Unit 1, Westinghouse System 80 RVI, as the valid prototype as defined in the RG 1.20 (Reference 1) because the APR1400 RVI has substantially the same design, arrangement, size, and operating conditions as Palo Verde Unit 1, Westinghouse System 80 RVI.

- From the comparison of the analysis results of the APR1400 RVI with the corresponding measured and predicted values of the valid prototype RVI, the results show that the major components of the APR1400 RVI have almost the same dynamic characteristics as the valid prototype and that the responses to flow-induced loads are less than the values that give the adverse effect on the structural integrities for the components.

- The evaluation of analytical predictions and visual inspection verifies that the APR1400 RVI are structurally adequate and acceptable for long term operation without adverse flow effects. The methods used in the CVAP for the APR1400 RVI are valid and sufficient to meet the requirements of the RG 1.20 (Reference 1).

6 REFERENCES

1. Regulatory Guide 1.20, “Comprehensive Vibration Assessment Program for Reactor Internals during Preoperational and Initial Startup Testing,” Rev. 3, U.S. Nuclear Regulatory Commission, March 2007.

2. Penzes, L. E., “Theory of Pump Induced Pulsating Coolant Pressure in PWRs,” Nuclear Engineering and Design, Vol. 27, 1974.

3. Bowers, G. and Horvay, G., “Forced Vibration of a Shell Inside a Narrow Water Annulus,” Nuclear Engr. Design V34, 1975.

4. CEN-263-(V)-P, “A Comprehensive Vibration Assessment Program for Palo Verde Nuclear Generating Station Unit 1,” Combustion Engineering, Inc., January 1985.

5. Computer code ANSYS Release 12.0, ANSYS, Inc., 2009.

6. Ghosh, S. and Wilson, E., “Dynamic Stress Analysis of Axisymmetric Structures under Arbitrary Loading,” EERC 69-10, Berkeley: University of California, Earthquake Engineering Research Center, September 1969.

7. CEN-267(V)-P, “Interim Report on the Performance Evaluation of the Palo Verde Control Element Assembly Shroud,” Combustion Engineering, Inc., January 1984.

8. Young, W.C., “Roark’s Formulas for Stress and Strain,” Sixth Edition, New York; McGraw-Hill, 1989.

9. Blevins, R. D., “Formulas for Natural Frequency and Mode Shape,” New York: Van Nostrand Reinhold, 1979.

10. ASME Boiler and Pressure Vessel Code, American Society of Mechanical Engineers, 2007 Edition with 2008 Addenda.

11. HC-121AR-101, “Design Report for Reactor Vessel Core Support and Internal Structures for Shin-Kori Nuclear Power Plant Units 3 & 4,” Rev.2, Doosan Heavy Industries & Construction, October 2013.

APPENDIX A:
VIBRATION ASSESSMENT
FOR THE STEAM GENERATOR INTERNALS

A.1 INTRODUCTION

The purpose of this appendix is to provide a comprehensive vibration assessment program (CVAP) for the APR1400 steam generator (SG) upper internals. The potential adverse effects from pressure fluctuations and vibrations were evaluated to verify the structural integrity of the SG upper internals for flow-induced vibrations prior to commercial operation. This appendix presents the vibration and stress analysis program performed in accordance with the Nuclear Regulatory Commission Regulatory Guide (RG) 1.20 (Reference A-1).

A.2 GENERAL ARRANGEMENT AND FLOW CONDITION

A.2.1 General Arrangement

The SG upper internals consist of the moisture separator assembly and the steam dryer assembly. The general arrangement of the SG upper internals is shown in Figure A.2-1.

The moisture separator assembly is located above the tube bundle. The moisture separator assembly consists of the moisture separators, separator support plate, drain trap pipes, shroud, and bottom ribs. The [ ]^{TS} moisture separators are arranged in a triangular array and are welded to the separator support plate. The [ ]^{TS} spinner blades, which cause centrifugal acceleration of the steam flow, are located in the lower part of the moisture separator. The cylindrical shell of the moisture separator is perforated to allow the water to flow out of the moisture separator. The cover plate of the moisture separator is also perforated to provide the flow path for the steam and water mixture. The mesh wires are located in the upper part of the moisture separator. The moisture separator assembly is shown in Figure A.2-2.

The steam dryer assembly is located above the moisture separator assembly. The steam dryer assembly consists of the dryer banks, dryer vanes, support rods, dryer support plate, support lugs, support beams, seal plate, and drain pipes. The steam dryer assembly is supported by the support lugs, which are welded to the upper shell of the SG. There are [ ]^{TS} dryer bank assemblies, which contain a number of dryer vanes. The center of the bank assembly is open to permit steam flow through the dryer vanes. The drain pipes run from the bottom of the bank assemblies to the drain trap pipes on the separator support plate. The drain pipes carry away the saturated water separated out by the dryer vanes. The steam dryer assembly is shown in Figure A.2-3.

A.2.2 Flow Condition

The basic function of the SG is to transfer heat from the primary side fluid through the U-tube bundle to the secondary side fluid. The feedwater entering the SG through economizer feedwater nozzles flows upward along the tube bundle. As it flows upward, the fluid on the secondary side is heated by the primary side fluid through the tube wall. The secondary side fluid boils and becomes a mixture of saturated liquid and steam. The saturated mixture continues to flow upward into the moisture separator assembly.

The two-phase flow leaving the tube bundle enters the moisture separator assembly with spinner blades. The liquid in the two-phase flow is separated out from the mixture due to the centrifugal forces caused by the spinner blades. The two-phase flow then travels upward to the entrance of the steam dryer assembly. The multiple changes in flow direction take place in the dryer vanes of the steam dryer assembly, and the remaining liquid in the two-phase flow is separated out. The steam flow exits the steam dryer assembly

and then leaves the SG through the steam outlet nozzles. The saturated water that has been separated from the two-phase flow is returned to the SG downcomer region and mixes with feedwater entering the SG through the downcomer feedwater nozzle. This water flows down the annulus between the shroud and shell and enters the tube bundle region through the opening of the shroud. The flow path of the secondary side fluid in the SG is shown in Figure A.2-4.

TS

Figure A.2-1 Steam Generator Upper Internals

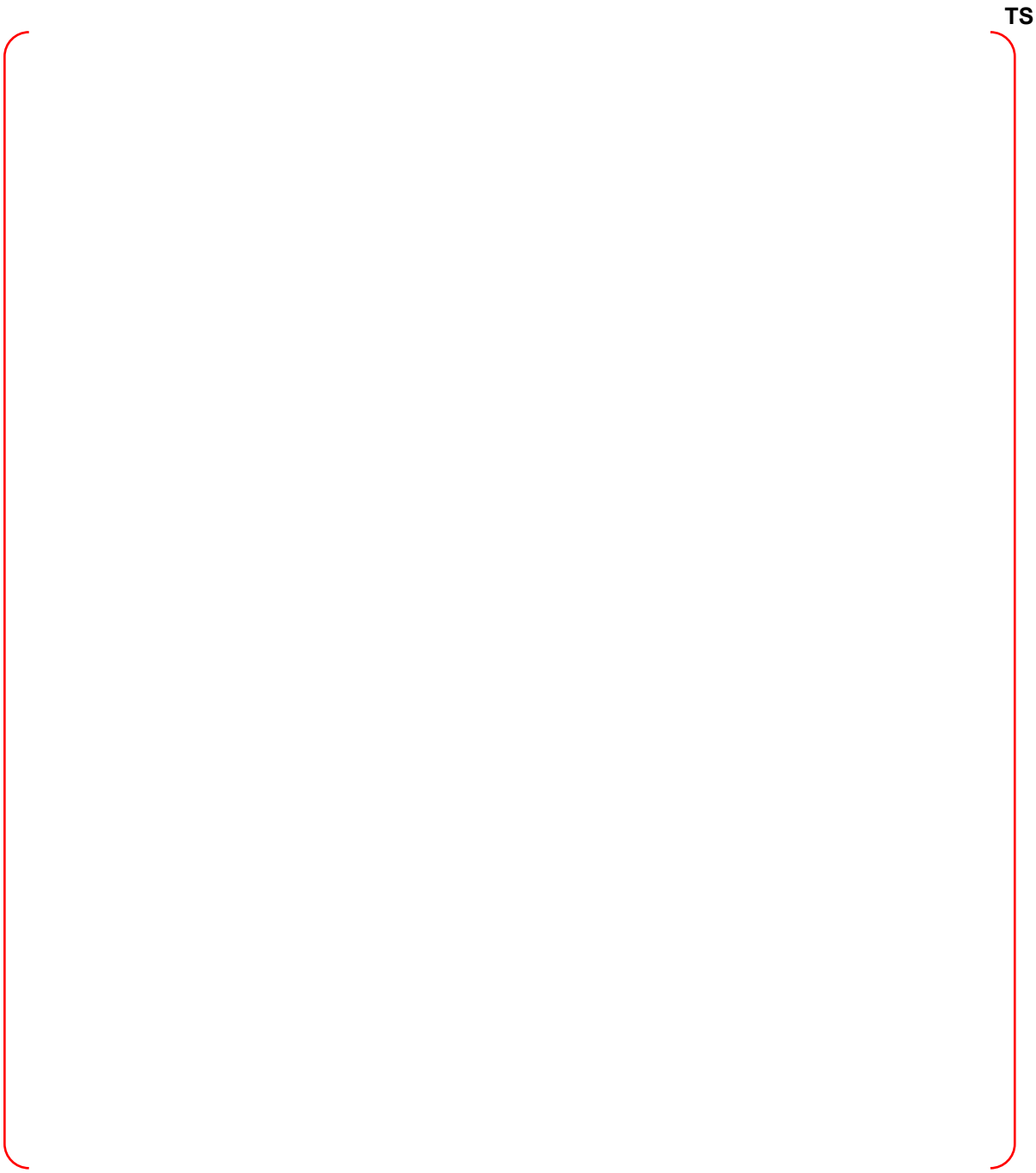

Figure A.2-2 Moisture Separator Assembly

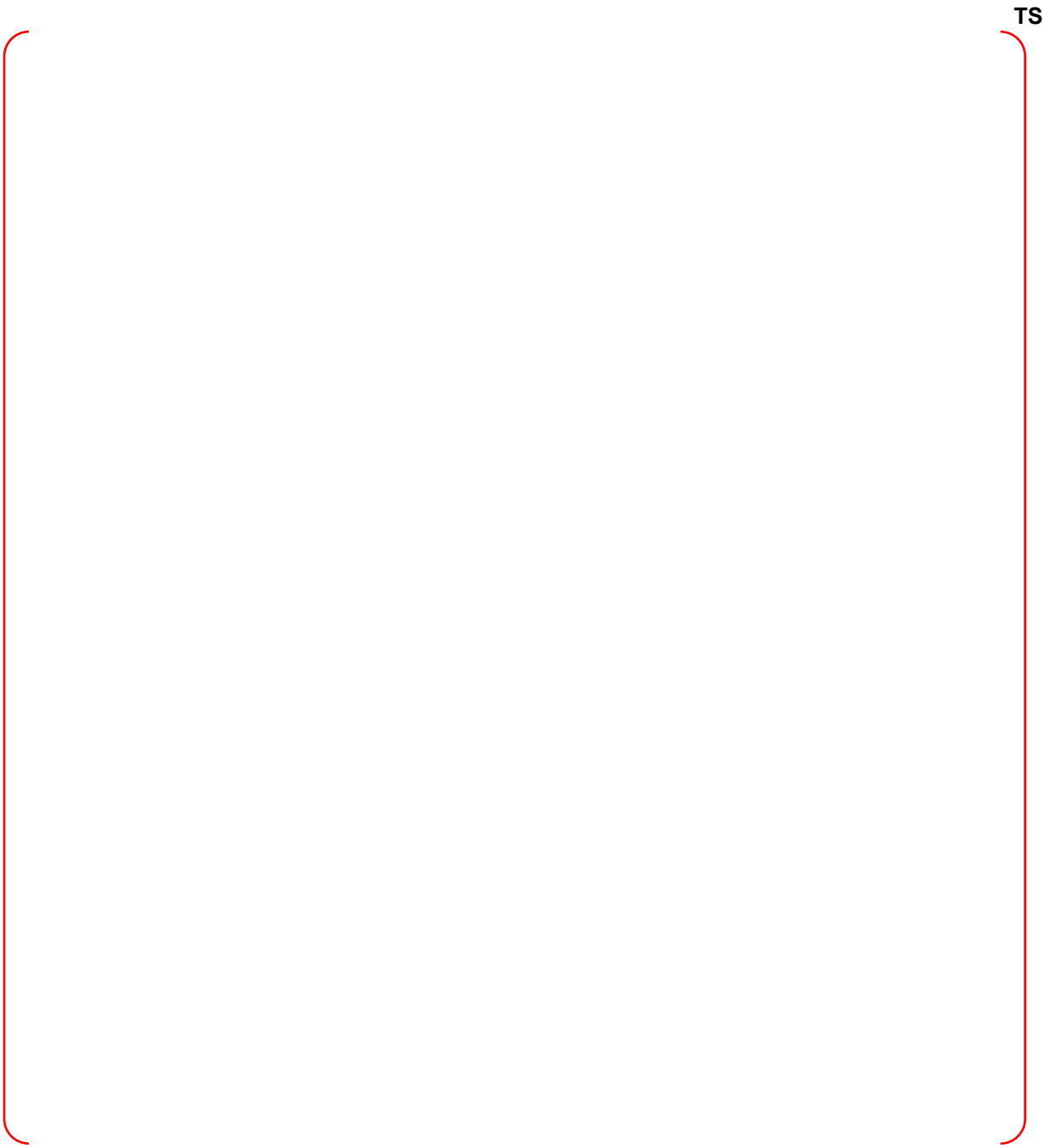

Figure A.2-3 Steam Dryer Assembly

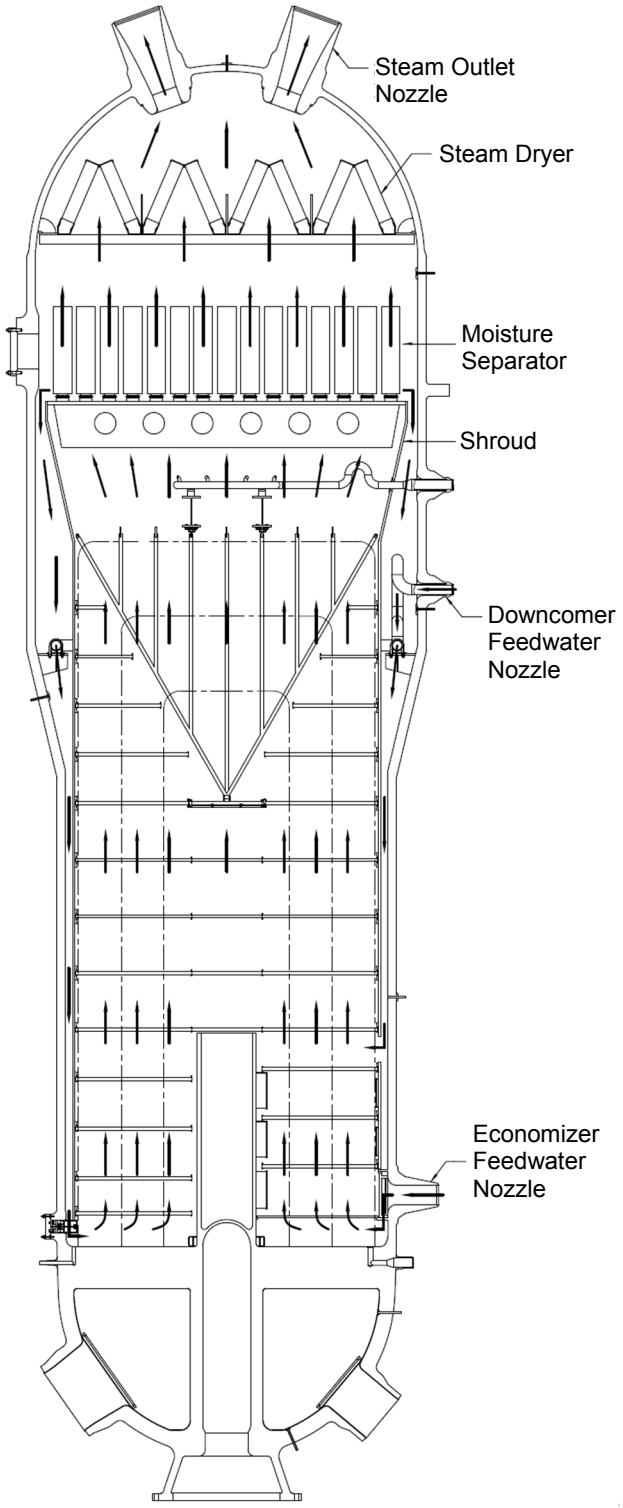

Figure A.2-4 Flow Paths of Secondary Side Fluid in the Steam Generator

A.3 VIBRATION AND STRESS ANALYSIS PROGRAM

This section describes the vibration and stress analysis program performed in accordance with RG 1.20. The potential adverse effects from pressure fluctuations and vibrations were evaluated to verify the structural integrity of the moisture separator assembly and the steam dryer assembly. The general methodology used in the analysis of the SG upper internals is identical to that used in the RVI analysis.

A.3.1 Hydrodynamic Load Analysis

The moisture separator assembly and the steam dryer assembly are subjected to the turbulent flow that causes the hydrodynamic loads acting directly on the structures during plant operations. The hydrodynamic loads are classified as random vibrations and cause the pressure fluctuations, vibrations, and resultant cyclic stresses that should be evaluated in the vibration and stress analysis program.

The most important fluid mechanical parameter that characterizes the turbulent forcing function is the pressure power spectral density (PSD), which is a measure of the magnitude of the forcing function as a function of frequency. In this section, the PSDs for the turbulent flow during steady-state full-power operations are derived to analyze the hydrodynamic loads. The thermal-hydraulic design data for steady-state full-power operations are listed in Table A.3-1.

A.3.1.1 Pressure PSD for the Inside of the Moisture Separator

The dynamic pressure of the confined annular flow was measured in a dynamic scale flow model (Reference A-5). Based on data from a scale model test, M. K. Au-Yang (Reference A-4) derived the empirical normalized PSD equations for turbulent flow without cavitation as follows:

$$\frac{G_p(f)}{\rho^2 V^3 R_H} = 0.155e^{-3.0F} \quad \text{for } 0 < F < 1.0$$

$$= 0.027e^{-1.26F} \quad \text{for } 1.0 \leq F \leq 5.0$$

Where:

- $G_p(f)$ = Pressure PSD
- F = Dimensionless Frequency (= f R_H / V)
- f = Frequency
- R_H = Hydraulic Diameter / 2
- V = Fluid Velocity
- ρ = Fluid Density

Since the flow was allowed to impinge upon the flow channels perpendicularly before it flowed down the annular flow channel in scale model test, Au-Yang's data generally show much higher turbulence intensity for the same velocity.

Figure A.3-1 compares the normalized random pressure PSD, computed with the empirical equations, and field test data (Reference A-4). As shown in Figure A.3-1, the empirical equation agrees reasonably well with field test data. The upper bound curve is above the field data points except those corresponding to the signal noise or far-field acoustic noise. The mean curve is close to the mean field data points.

The pressure PSD for the inside of the moisture separator was calculated with the empirical equations for the upper bound curve. Since the pressure PSD calculated with the equations is conservative and is normalized to allow the use in the analysis for design, it is applicable to the analysis of the moisture separator. The inside radius of moisture separator (R_H), steam density (ρ), and steam velocity (V) were used in the calculation of the pressure PSD. The calculated PSD is shown in Figure A.3-2.

A.3.1.2 Pressure PSD for the Moisture Separator Assembly and the Steam Dryer Assembly

The pressure PSDs for the moisture separator assembly and the steam dryer assembly were calculated from the computational fluid dynamics (CFD) analysis performed using the commercial fluid dynamics program, ANSYS CFX (Reference A-6).

The three dimensional CFD model of the SG upper internals was developed for the CFD analysis and is shown in Figure A.3-3. The model consists of the moisture separators, steam dryer assembly, steam outlet nozzles, and steam lines. The steam line has the inside diameter of 72.66 cm (28.607 in) and the total length of the steam line included in the model is 32 m (1260 in). The dryer vanes were modeled as porous media.

[

]TS. The steam properties were obtained from ASME steam tables (Reference A-7).

The pressure PSDs for the moisture separator assembly and the steam dryer assembly are shown in Figures A.3-4 and A.3-5, respectively.

Table A.3-1 Thermal-Hydraulic Design Data for Steady-State Full-Power Operations

Design Data	APR1400
Primary Side Flow Rate per SG, kg/hr (lb/hr)	37.78E6 (83.3E6)
Primary Side Inlet Temperature, ^{o}C (^{o}F)	323.9 (615)
Primary Side Outlet Temperature, ^{o}C (^{o}F)	290.6 (555)
Primary Side Operating Pressure, kg/cm^{2}A (psia)	158.2 (2,250)
Feedwater Temperature, ^{o}C (^{o}F)	232.2 (450)
Saturated Steam Pressure at Steam Dome Region, kg/cm^{2}A (psia)	70.3 (1,000)
Steam Flow Rate per SG, kg/hr (lb/hr)	4.070E6 (8.975E6)

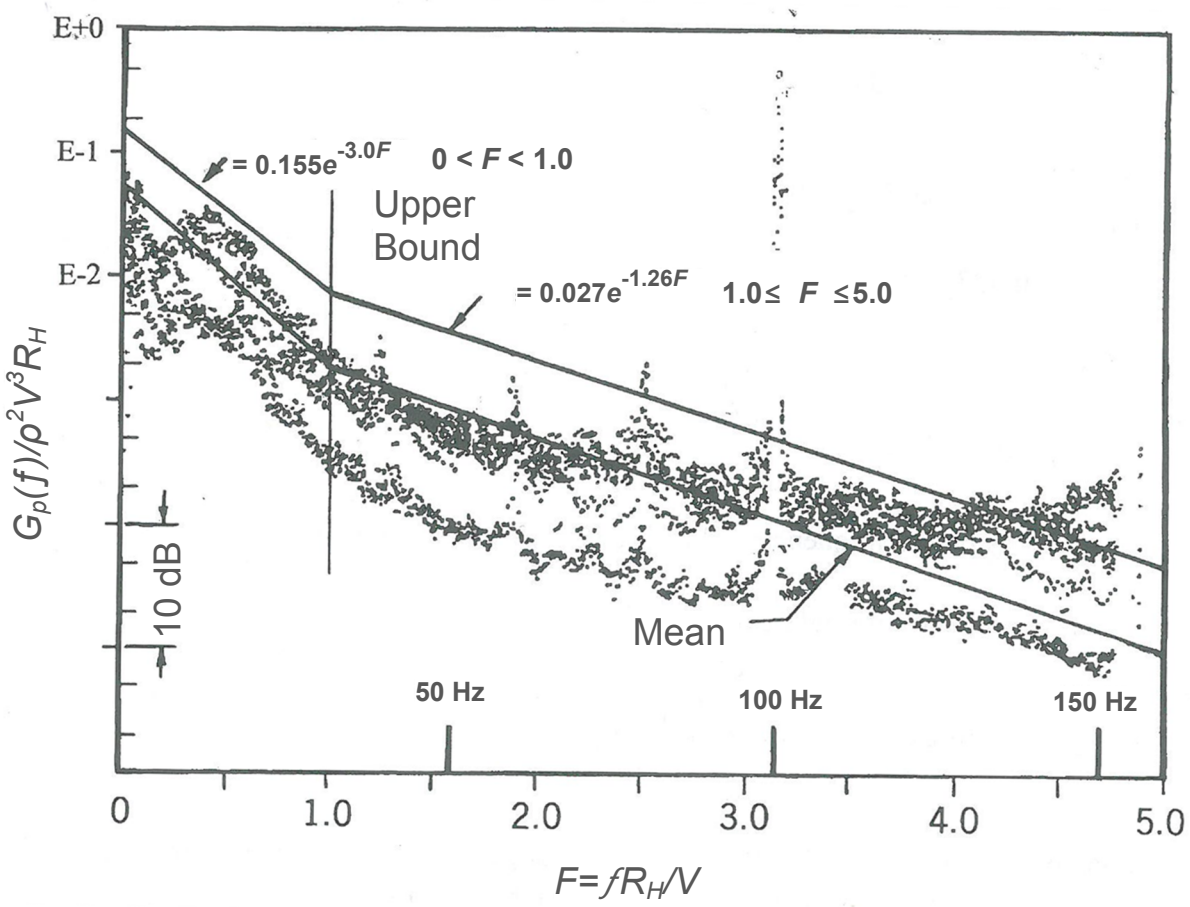

Figure A.3-1 Comparison of Empirical Normalized PSD Equation with Field-Measured Data

Figure A.3-2 Pressure PSD for the Inside of the Moisture Separator

TS

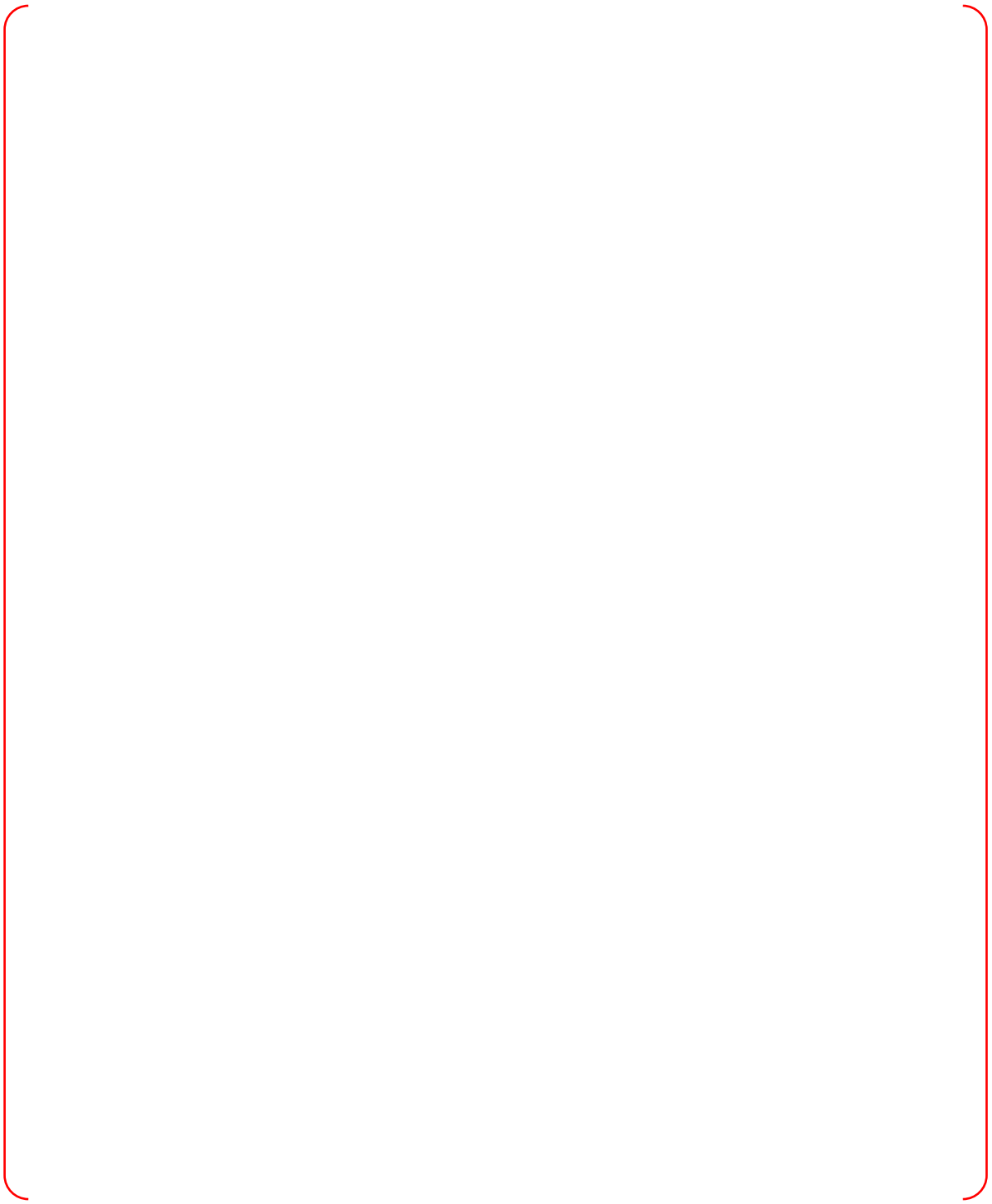

Figure A.3-3 CFD Model of the Steam Generator Upper Internals

Figure A.3-4 Pressure PSD for the Moisture Separator Assembly

Figure A.3-5 Pressure PSD for the Steam Dryer Assembly

A.3.2 Structural Response Analysis

The structural response analyses of the moisture separator assembly and the steam dryer assembly were performed using the finite element method. The materials used in the analyses are listed in Table A.3-2. The material properties were obtained from Section II of ASME Boiler and Pressure Vessel Code (Reference A-3).

A.3.2.1 Modal Analysis

Moisture Separator Assembly

The three dimensional finite element model of the moisture separator assembly was developed using the finite element analysis program, ANSYS (Reference A-6). The model consists of the moisture separators, separator support plate, shroud, and bottom ribs. Shell elements were used to model the moisture separator assembly. Geometrically complicated parts of the moisture separator, such as the spinner blades and perforated plates, are simplified in the model. The perforated plates are replaced by equivalent solid plates and the spinner blades are modeled as additional mass. The hydrodynamic mass of the shroud was calculated in accordance with Section III of the ASME Code (Reference A-2) and added to the structural mass in the model. The finite element model of the moisture separator assembly is shown in Figure A.3-6.

The modal analysis was performed using the finite element model. The [ ]^{TS} was applied to extract eigenvalues. The natural frequencies and mode shapes of the moisture separator assembly are shown in Figures A.3-7 and A.3-8.

Steam Dryer Assembly

The three dimensional finite element model of the steam dryer assembly was developed using the finite element analysis program, ANSYS (Reference A-6). The model consists of the dryer banks, support rods, dryer support plate, support lugs, and support beams. Shell elements were used to model the dryer bank, dryer support plate, support lugs, and support beams, and beam elements were used to model the support rods. The dryer vanes are appropriately modeled as lumped mass in the vibration system. The finite element model of the steam dryer assembly is shown in Figure A.3-9.

The modal analysis was performed using the finite element model. The [ ]^{TS} was applied to extract eigenvalues. The natural frequencies and mode shapes of the steam dryer assembly are shown in Figures A.3-10 and A.3-11.

Table A.3-2 Materials of Moisture Separator Assembly and Steam Dryer Assembly

TS

TS

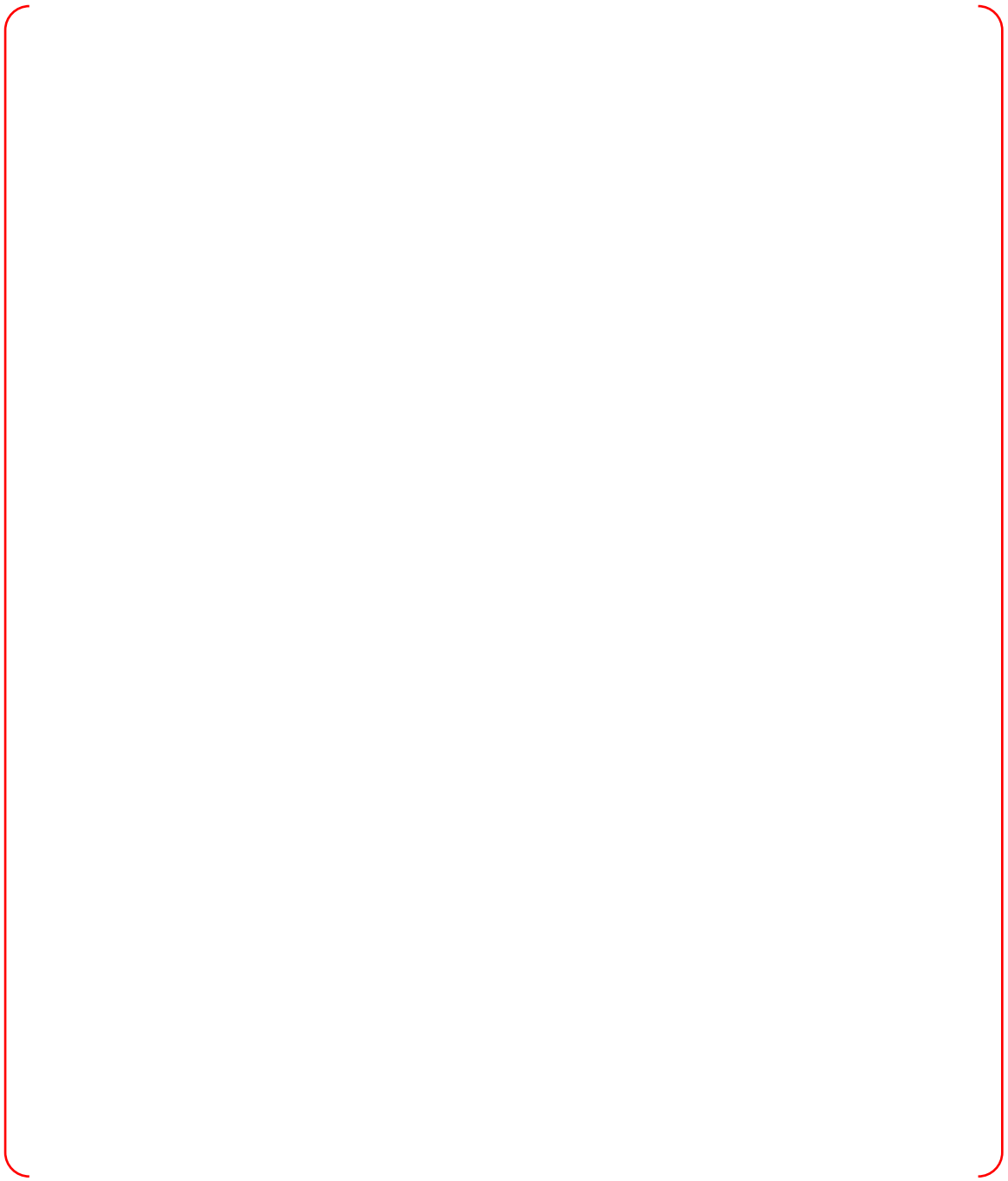

Figure A.3-6 Finite Element Model of the Moisture Separator Assembly

TS

Figure A.3-7 Natural Frequencies of the Moisture Separator Assembly

TS

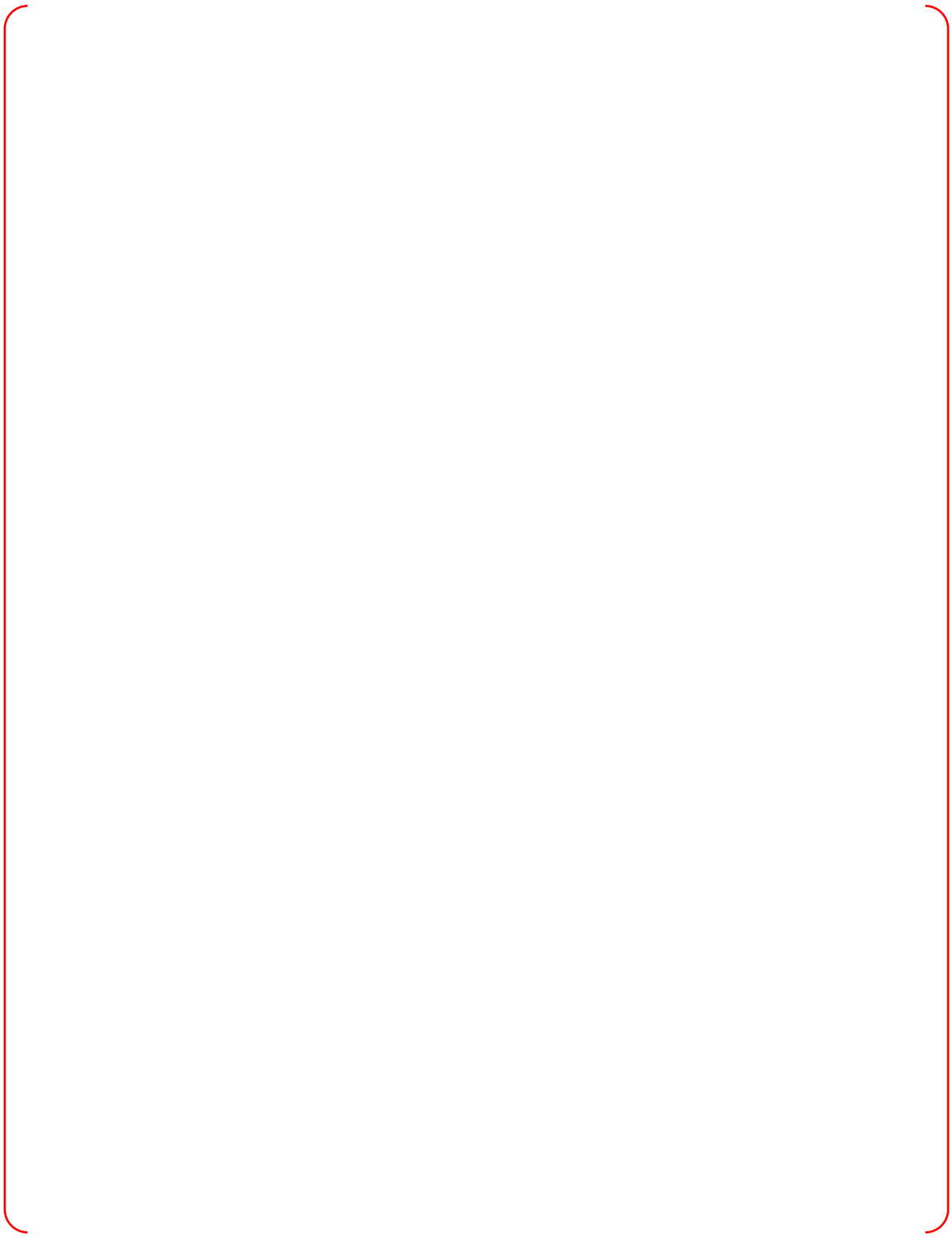

Figure A.3-8 Mode Shapes of the Moisture Separator Assembly

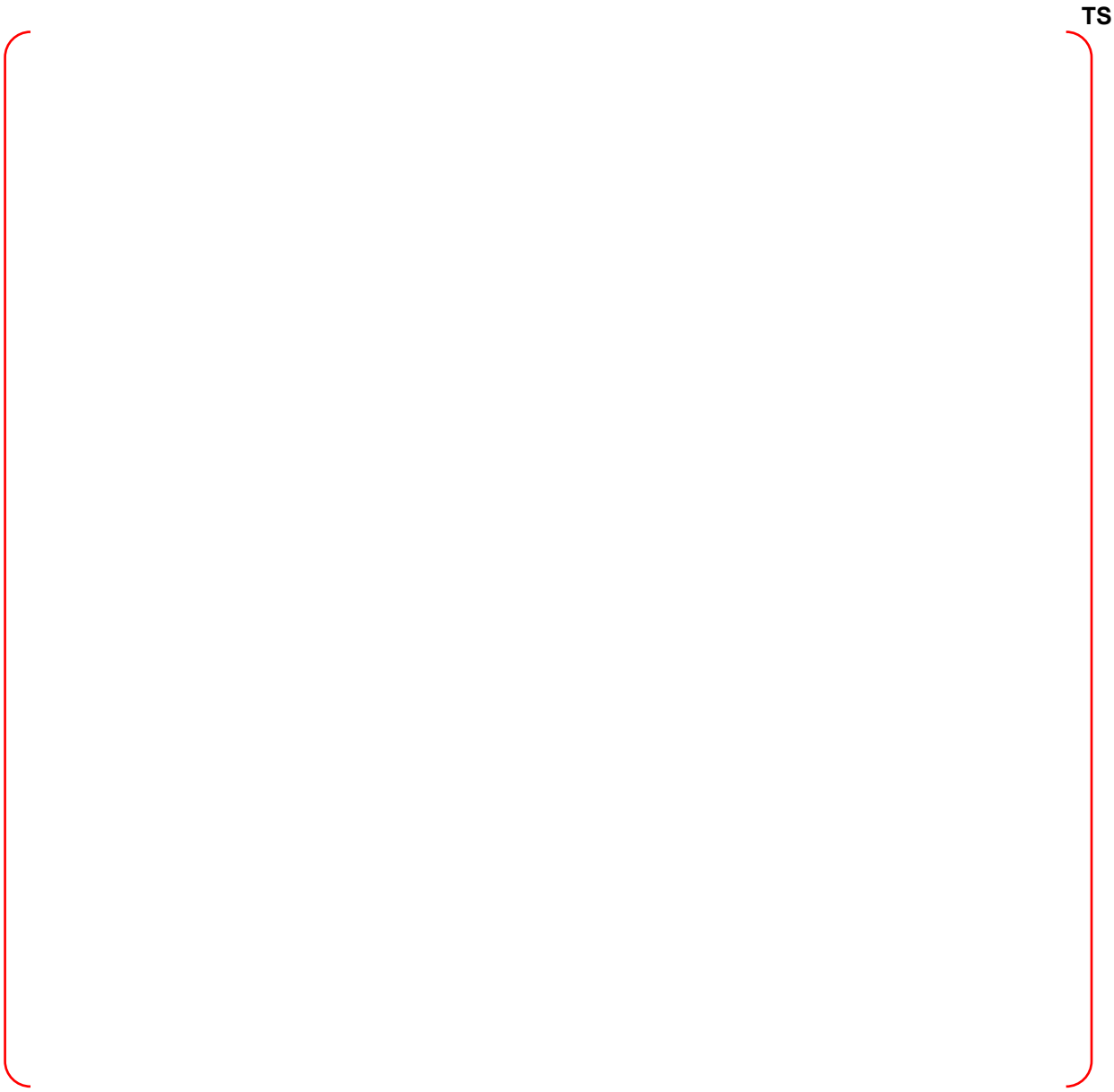

Figure A.3-9 Finite Element Model of the Steam Dryer Assembly

TS

Figure A.3-10 Natural Frequencies of the Steam Dryer Assembly

Figure A.3-11 Mode Shapes of the Steam Dryer Assembly

A.3.2.2 Power Spectral Density Analysis

The PSD analyses were performed using the finite element models of the moisture separator assembly and the steam dryer assembly. The PSDs calculated from the hydrodynamic analyses were applied to the models. The structural damping coefficient of [ ]^{TS} is used in the PSD analyses.

The structural responses were determined from the PSD analyses. The three sigma values of the responses, which statistically include expected output values for 99.7 percent of the time, were used in the evaluation.

A.3.2.3 Acceptance Criteria

The calculated stresses of the moisture separator assembly and the steam dryer assembly should comply with the fatigue stress limits set forth in Section III of the ASME Code. Although the moisture separators and the steam dryers are not code components, the ASME Code limits were conservatively used in the evaluation.

A.3.2.4 Summary of Results

The summary of the vibration and stress analyses are listed in Table A.3-3.

A.3.2.5 Bias Errors and Uncertainties

The dimensions used for developing the analytical models of the SG upper internals were determined based on the design drawings. The bias errors and uncertainties associated with the tolerances or alignments are not incorporated in the models.

Since the modal analysis results and the forcing functions obtained from analyses have uncertainties associated with the frequencies of the response peaks attributable to resonant modes, the vibration and stress analyses should address those uncertainties. In addition, uncertainties associated with CFD analysis should be addressed.

To account for all associated bias errors and uncertainties, the responses obtained from PSD analyses are multiplied by a factor of 3.0.

Table A.3-3 Summary of the Vibration and Stress Analyses

TS

A.4 CONCLUSION

A CVAP for the APR1400 SG upper internals has been developed and implemented in accordance with RG 1.20. The vibration and stress analysis was performed to evaluate the potential adverse effects from pressure fluctuations and vibrations for the SG upper internals. The stresses and displacements of the moisture separator assembly and the steam dryer assembly were calculated from the analysis and compared with the acceptance criteria. All of the stresses are satisfactory and meet the relevant requirements of Section III of the ASME Code. In addition, no excessive displacements were found in the analysis results of the moisture separator assembly and the steam dryer assembly.

Therefore, the structural integrity of the SG upper internals has been justified for the flow-induced vibration. In conclusion, the SG upper internals are adequately designed to accommodate steady-state and transient vibratory loads throughout the service life of the SG.

A.5 REFERENCES

A-1. Regulatory Guide 1.20, “Comprehensive Vibration Assessment Program for Reactor Internals during preoperational and initial startup testing”, Rev. 3, U.S. Nuclear Regulatory Commission, March 2007.

A-2. ASME Boiler and Pressure Vessel Code, Section III, “Rules for Construction of Nuclear Facility Components”, American Society of Mechanical Engineers, 2007 Edition with 2008 Addenda.

A-3. ASME Boiler and Pressure Vessel Code, Section II, “Materials”, American Society of Mechanical Engineers, 2007 Edition with 2008 Addenda.

A-4. Au-Yang, M.K., Flow-Induced Vibration of Power and Process Plant Components, New York: ASME Press, 2001.

A-5. Au-Yang, M.K. and Jordan, K.B., “Dynamic Pressure Inside a PWR - A Study based on Laboratory and Field Test Data”, Nuclear Engineering and Design 58 (1980), 113-125.

A-6. ANSYS Advanced Analysis Guide, Release 14.5, ANSYS Inc., 2012.

A-7. ASME International Steam Tables for Industrial Use, William Parry, 2000.

APPENDIX B:
VIBRATION ASSESSMENT FOR THE REACTOR COOLANT SYSTEM PIPING AND THE PIPING ATTACHED TO THE STEAM GENERATOR

B.1 SCOPE

The vibration assessment program consists of a vibration and stress analysis program, and a flow-excited acoustic resonance measuring and inspection program for the following system piping in conformance with U.S. Nuclear Regulatory Commission Regulatory Guide (RG) 1.20 (Reference B-1) and NUREG-0800 Section 3.9.2. (Reference B-3).

- Reactor coolant system (RCS) piping
- Main steam system (MS) piping
- Feedwater system (FW) piping
- Condensate system (CD) piping

B.2 VIBRATION AND STRESS ANALYSIS PROGRAM

The strategy for mitigation of adverse flow effects that could be generated by various excitation mechanisms, both flow-excited acoustic resonance and flow-induced vibration, is achieved by:

- Preventing Sources of Excitation: Screening analyses to avert the occurrence of potentially detrimental pulse sources by design changes (e.g., use of shorter standpipes in dead-leg piping)
- Preventing Consequences of Unavoidable Excitation Sources: Analyze pressure pulsations having dominant excitation frequencies (such as from pump rotations or control valve throttling flow), to determine if design changes should be made for components that could be unacceptably excited by those dominant frequencies (e.g., by changing distance between pipe supports or thickness of piping).
- Instrumentation and vibration testing plan to verify that acceptable and bounded levels of vibration are experienced in the plant.

B.2.1 Approach for Screening Flow-Excited Acoustics

The screening methodology, described in this section, in the design of piping and valve components is implemented to prevent the occurrence of acoustic resonance, as discussed in Reference B-6. The approach for screening requires an evaluation of critical points in the system that exhibit a potential for an acoustic wave to be generated. For branch piping with the potential for acoustic resonance, design measures for avoidance of the acoustic resonance will be taken.

B.2.1.1 Screening Approach for Flow Past Standoff Pipe

The focus of this screening technique is on resonance caused by flow-induced oscillations that may develop in valve cavities or flow past a standoff pipe (side branch). Shear wave resonance of cavities occurs when the standing acoustic wave in the cavity couples with the vortices shedding off of the leading edge of the cavity's opening, as depicted in Figure B.2-1.

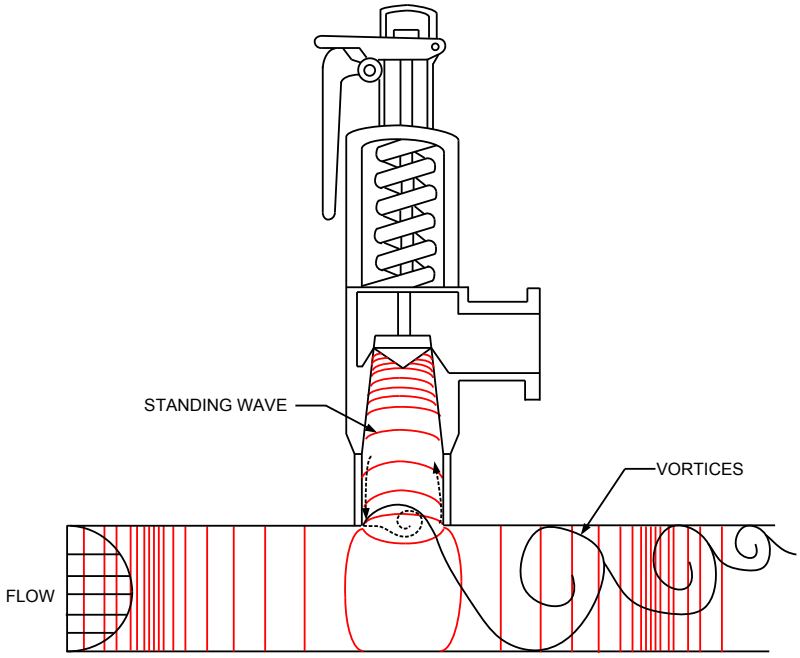

Figure B.2-1 Acoustic Resonance for Flow Past Standoff Pipe

When the vortex shedding frequency becomes close, or equal, to the acoustic frequency of the cavity, increased pressure fluctuations occur. The resulting resonance pressure-flow oscillation can travel through the affected piping system with little attenuation. The oscillating pressure amplitudes inside the cavity can be much greater than the main piping dynamic pressure. Experience from Safety Relief Valves (SRVs) in BWR power plants indicates that the vibration and noise occur during normal plant operation when the SRV is not blowing down, and the pulsation and vibration exist at a dominant frequency or tone.

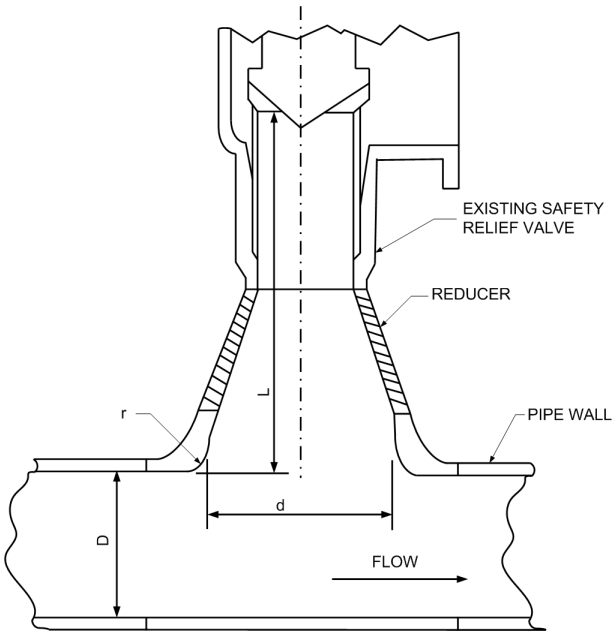

Figure B.2-2 Flow Past a Closed Side Branch

The flow-induced oscillations for the onset of resonance are characterized in terms of a non-dimensional frequency, namely the Strouhal number. The following equation defines the Strouhal number:

$$f = SU/d \quad \text{Equation 2-1}$$

Where:

f = frequency (Hz)

S = Strouhal Number

U = Pipe free stream velocity

d = Insider diameter of side branch entrance.

D, L, d and r are depicted in Figure B.2-2.

The unsteady flows into and out of the cavity produce a compression of the vertical column and excite the acoustic depth modes with a frequency of the following form:

$$f = NC/(4L) \quad \text{Equation 2-2}$$

Where:

N = mode number, e.g., 1, 3, 5...

C = acoustic velocity in the flow stream

L = branch stub length (or standpipe height for safety relief valve)

When the vortex shedding excitation frequency (Strouhal instability), and the first modal frequency of the cavity coincide (N = 1), an acoustic resonance condition is created which appears as a loud noise. For the resonant situation, Equation 2-1 and 2-2 are used to determine the Strouhal number:

$$S\,U/d = C/(4L)$$

$$\rightarrow S = Cd/(4LU) \quad \text{Equation 2-3}$$

These pulsations can be further amplified if the standpipe acoustic mode is coupled with an acoustic mode of the main piping, with velocity anti-node near the side branch entrance. In that case, the acoustic impedances will match and the side branch resonance will couple with the main pipe resonance. Conversely, if the side branch is located near a main piping velocity node (pressure maximum), an impedance mismatch occurs and the stub standing wave will attenuate.

The data and analysis provided in Reference B-6 concludes that the lowest Strouhal number for which no coupling should occur is about 0.60. The experimental investigations in Reference B-7 indicated that no coupling should occur for a Strouhal number of 0.62 and above. The apparent discrepancy in the two studies is due to the type and number of side branches investigated. The evaluations in Reference B-6 focused on single side branches on a pipe, while Reference B-7 extended the scope to cover the interactions between a small set of piping components (single, tandem and coaxial arrangements of closed side-branches). Furthermore, Reference B-7 examined the effect of a 90˚-elbow in the pipe upstream of the side branch. The results of Reference B-10 demonstrate that the value for the Strouhal number at the initiation of resonance varies over a wide range ($0.35 < S < 0.62$) depending on the ratio d/D, where D is the main pipe diameter. Hence, for conservatism a value of $S_{crit} = 0.63$ is used to mark

the critical flow velocity that leads to resonance. The maximum velocity of the installation should be less than the critical velocity to avoid the occurrence of resonance ($U < U_{crit}$ for safe design) or, for a given velocity in the system, the length of the standpipe should be shorter than a critical length ($L < L_{crit}$).

The Mach number, M, is defined as the ratio of flow speed to speed of sound, U/C. Thus, substituting M in Equation 2-3 with the critical value of the Strouhal number yields:

$$\frac{d}{L} = 4SM \quad \text{Equation 2-4}$$

And the critical ratio of d/L when S= 0.63 is given by:

$$(\frac{d}{L})_{crit} = 2.52M \quad \text{Equation 2-5}$$

So, by design, d/L must be shown to be greater than 2.52 M to avoid resonance for full proposed operating conditions. The minimum allowable diameter-to-length ratio of the cavity is governed by the Mach number of the flow past the opening of the side branch.

If the pipe branch sizes and system velocities are already established, then check to see if the length (L) of a given size standpipe (d) will be acceptable (for avoiding resonances) in a given flow stream, the following screening criterion will be used:

$$L < \frac{d}{2.52M} \quad \text{Equation 2-6}$$

If the criterion in Equation 2-6 is not satisfied, design modifications will be adopted to either enlarge the branch diameter at the junction with the main pipe, or shorten the length of the closed standpipe.

Another feature of the branch connection design that can mitigate the ratio of d/L is the use of rounded or chamfered branch penetrations. When the corners of the branch mouth are rounded with a radius of curvature ' r ', the critical flow velocity scales with the blend radius + standpipe inside diameter. The modified diameter (d+r) is used as an equivalent diameter and substituted in the formula for the vortex shedding frequency in Equation 2-1:

$$f = \frac{su}{(d+r)} \quad \text{Equation 2-7}$$

$$L < \frac{(d+r)}{2.52M} \quad \text{Equation 2-8}$$

The evaluation of standoff pipes in the piping system and the cavities for safety and relief valves that have a potential to generate pressure pulses under the range of possible plant operating power levels and flow rates will be performed as part of the design process to ensure that acoustic resonance does not occur.

B.2.1.2 Control Valve and Operator Resonance

Flow control valves (e.g., regulating valves, throttle valves) generate strong flow vortices which can create fluctuations in pressures that can cause pulsations in the downstream piping and possibly result in pipe fatigue failure. In addition, the vibrating pipe surfaces generate airborne noise that may exceed noise levels mandated to provide a safe working environment in the overall plant.

The frequency at which the energy content of the pressure pulsations flowing past the constrictive opening of a control valve and is greatest can be correlated with the non-dimensional parameter, the Strouhal number and is called the peak response frequency.

$$S = f\frac{D_{jet}}{U_{vc}}$$ Equation 2-9

Where:

D_{jet}= effective diameter of the restricted flow path past the throttling element (i.e., sometimes called the “plug” in the control valve, and often of proprietary design)

U_{vc}= velocity of the fluid through the vena contracta of the restriction

The Strouhal number is approximately 0.2 over a wide range of pipe Reynolds numbers based on empirical data, as shown in References B-14 and B-15. This approach is used for water and other nearly incompressible fluids.

The piping will be designed so that there is the peak response frequency of the valve not to possibly excite a mechanical resonance in a pipe segment or corrected by adding a pipe support, if necessary.

Higher frequency pulsations from the valve flow will travel transversely and interact with the pipe wall. The pipe walls will respond to the excitation by a localized flexing in radial shell modes. The magnitude of the response depends on the pipe diameter and wall thickness. If the circumferential radial natural frequencies correspond to the frequencies generated by the valve, stress waves will be generated that travel the circumference of the pipe. The stress waves generate undesirable piping deflections that are usually first experienced by high levels of airborne noise. The vibration level of the piping in these modes has been correlated to sound pressure level (SPL) measurements made one inch from the outer surface of the pipe (Reference B-16). A C-weighted (i.e., targeted at human health ranges) SPL measurement of 136 dB indicates excessive pipe vibration that likely will lead to fatigue failure.

Only a small portion of the energy of the jet at the vena contracta of the control valve is available to excite acoustic resonances in the downstream piping (Reference B-17). However, with certain combinations of acoustic velocity and pipe length, the reflected wave from the end of the pipe run can add constructively to the pulsations leaving the valve. This is an acoustic standing wave resonance.

The resonant acoustic frequency of a pipe of length L closed at its end is:

$$f_n = \frac{(2n-1)}{4}\frac{c}{L}$$ Equation 2-10

Where:

c = the acoustic velocity in the pipe

n = 1, 2, 3…

Thus, the odd harmonics of a quarter wavelength are in resonance.

If the pipe has an open end condition, then the resonant acoustic frequencies are:

$$f_n = \frac{n}{2}\frac{c}{L+0.6\,a}$$ Equation 2-11

Where:

a = the pipe radius.

The acoustic resonance would occur if the pipe length matched an integral number of half-wave lengths

associated with the excitation frequency.

The length of the piping will also be checked to ensure that there will not be an acoustic resonance at the excitation frequency.

The acoustic velocity used in the calculations above for the resonant acoustic frequency of the piping run will consider the distensibility (capacity of being distended, extended or dilated) of the pipe wall. This additional flexibility lowers the effective speed of sound in the piping.

For infinitely rigid pipe walls, the speed of sound of the fluid is:

$$c = \sqrt{\frac{K}{\rho}}$$ Equation 2-12

Where:

K = bulk modulus of the fluid

ρ = fluid density

Accounting for the finite stiffness of the walls requires (References B-16 and B-18):

$$c = \sqrt{\frac{K'}{\rho}}$$ Equation 2-13

Where:

K' = the mean diameter of the pipe

$$\frac{1}{K'} = \frac{1}{K} + \frac{d}{t*E}$$ Equation 2-14

d = the mean diameter of the pipe

t = is the pipe thickness

E = Young's modulus of the pipe

B.2.1.3 Pump Induced Vibration

Pump induced pressure pulsations are potential sources of piping steady-state vibration. Pulsations originate at the pump and travel throughout the entire discharge piping. The effects of pressure pulsations can be more severe when they coincide with the natural frequency of the piping system downstream of the pumps. Eliminating the pulsations may involve modifying the pump or changing the piping acoustical frequency. For example, piping acoustical properties can be changed through the addition of a pulsation damper and suction stabilizer.

When pressure pulsations travel through the piping at any instant in time, the pressure on one elbow may not equal the pressure on the other elbow of the piping leg, resulting in an unbalanced force in the pipe leg. Also experienced were several support failures, vibration failures of attached instrumentation and other small-branch piping, as well as excessive vibrations in the suction piping.

Pump-induced pressure pulsations occur at distinct frequencies, which are multiples of the pump speed and of the number of pump plungers, blades, volutes, or diffuser vanes. The potential pulsation

frequencies are defined by the following equation:

$$f = \frac{n*X}{60} \ or \ \frac{n*X*Y}{60}$$ Equation 2-15

Where:

f = frequency of pressure pulsation, cycles/sec. (Hz)

n = 1, 2, 3, and so on

X = pump rotating speed, rpm

Y = dependent on pump type: number of pump plungers, blades, volutes, or diffuser vanes

The appropriate action placed on the design of the piping system to mitigate pump-induced acoustic resonance is to ensure a thorough design review of the pump characteristics and the natural frequency of the piping system downstream of the pumps to be tuned away from the pump produced pulsation frequencies.

B.3 FLOW-EXCITED ACOUSTIC RESONANCE MEASURING AND INSPECTION PROGRAM

Vibration monitoring and testing of piping systems involves assessing the operating vibration of in situ piping systems. The goal of monitoring is to qualify a piping system for the vibration it actually experiences and determine with sufficient accuracy that the magnitude of the vibration-related stresses are not large enough to cause a failure over the design life of the power plant. Monitoring is performed to determine the response of the piping to forcing resulting from the operation of the system. The cause of the vibration (i.e., the forcing function) becomes important when one attempts to control and reduce excessive vibrations and also when one correlates analytical and experimental results. Vibration testing is performed to quantify system parameters such as frequencies, damping, and mode shapes. Experimental parameters obtained by means of testing can then be used to improve and verify analytical models.

B.3.1 Identification of Acoustic Resonance by Testing

The conventional methods used to identify and diagnose these sources of acoustic vibration are provided. During pre-operational testing of the power plant, acoustic vibration sources will be identified using the distinguishing characteristics and if acoustic resonance is identified in a piping system, then measures will be taken to mitigate resonance.

B.3.1.1 Acoustic Resonance Caused by Flow Past Standpipes

Acoustic resonance from flow past a standpipe, a side branch attached to the main piping, or a dead leg is well-understood and, as experience indicates, its occurrence at a power plant is accompanied by pure-tone, single frequency, high amplitude excitation. The noise generated from such an event is an identifying characteristic of a problem due to flow-induced instability where pulsations are generally in excess of 100 Hz. In addition, the vibration and noise tend to increase significantly as the load is increased, with the amplitude changing rapidly with flow rate as the critical flow rate is approached from above or below.

B.3.1.2 Acoustic Resonance Caused by Control Valve and Operator

A potential source of high-frequency vibration is vortex shedding and high-frequency pressure fluctuations caused by throttling at control valves. The dynamic coupling effects between valve and fluid system may intensify the amplitude of vibration as discussed in Reference B-8. The approach for mitigating valve-

induced resonance will verify that the natural frequency of the control valve is not near an acoustic resonance frequency of the downstream piping either by design, or by providing damping. Another best practice for the arrangement of control valves is to avoid the use of back-to-back fittings, such as an elbow immediately downstream of a valve, which can increase flow turbulence and vibration.

B.3.1.3 Acoustic Resonance Caused by Pumps

A certain level of pressure fluctuations arising out of the pump is unavoidable and has no detrimental effects. Excessive pressure fluctuations, however, can excite pump and pipe vibrations and might even cause damage when the pulse frequency corresponds to an acoustic resonance frequency or structural frequency of the piping. Consequently, actual pulsating wave amplitudes can be considerably higher than the induced level. The accentuating factors at resonance may be between 50 to a 100 times higher than the originating pulses.

B.3.2 Acoustic Resonance Detection Methods

The portions of representative piping trains that are most likely to develop acoustic resonance are monitored. The detailed analysis for acoustic resonance specified in Section B.2.1 is used to determine acoustic resonance for these trains. Acoustic resonances are detectable by monitoring the magnitude and frequencies of dynamic pressure pulsations in the fluid upstream or downstream of the source of resonance excitation.

Monitoring is not required for other piping trains that are sufficiently similar. Piping trains are considered to be sufficiently similar if they have the same diameter (main and branch piping), same components, and if the pipe routing, including branch piping, and run length are within construction tolerances typical of piping classes. This will ensure that the acoustic characteristics of the piping trains are reasonably close. Also, flow conditions should be similar (within two percent at design conditions).

Use of Strain Gauges for Dynamic Pressure Monitoring

Strain gauges are relatively simple and reliable to install. They have a distinct advantage of being non-intrusive to the pressure boundary but they will require careful preparation of the surfaces and the availability of an appropriate access to the desired locations. They have the capability to sense rapid transients up to 100,000 Hz (Reference B-9).

A monitoring system will be established that uses strain gauges to measure dynamic changes in pressure inside the pipe. The system will measure frequencies up to 300 Hz. The strain gauges will be oriented such that they measure hoop strain in the pipe. At a given longitudinal (axial) location, four gauges will be placed around the circumference of the pipe every 90°.

Two stations of four strain gauges will be placed at two axial locations along a run of straight pipe. The axial distance between these stations will be less than half the wavelength of the upper limit frequency, as recommended in Reference B-10 and calculated by the following equation:

$$D_{sp} = \frac{c}{2f} \qquad \text{Equation 2-16}$$

Where*:*

D_{sp}= maximum allowable distance from the companion set of strain gauges

c = speed of sound inside the pipe

f = frequency upper limit (300 Hz)

The strain reading from the strain gauge stations are calibrated for the particular geometry of the pipe section as described in the equation below. The pressure signals occur at a higher frequency than temperature fluctuations. Bending stresses in the pipe due to vibration will be canceled out by the circumferential setup of the strain gauges. When the pipe is in bending, any tension that is experienced by one gauge due to bending will be experienced as compression by the opposite gauge 180° away. Therefore, the average measured stress will be zero. The strain oscillation reading, for a predetermined period (typically a few seconds), is caused by acoustic pressure waves only and is transformed into pressure amplitudes by the following equation, which follows from the definition of the Poisson ratio:

$$\epsilon_h = \frac{\sigma_h - \upsilon\sigma_l}{E} \qquad \text{Equation 2-17}$$

where:

ϵ_h = strain due to lateral and longitudinal stress

σ_h = hoop stress in the pipe

σ_l = longitudinal stress in the pipe

υ = Poisson's ratio

From Reference B-11, the longitudinal stress in the pipe is:

$$\sigma_l = \frac{Pr_i^2}{r_0^2 - r_i^2} \qquad \text{Equation 2-18}$$

From Reference B-11, hoop stress as a function of the radius, r is:

$$\sigma_h(r) = \frac{Pr_i^2(r_o^2 + r^2)}{r^2(r_0^2 - r_i^2)} \qquad \text{Equation 2-19}$$

where:

P = internal pressure

r_i = inner radius

r_o = outer radius

Therefore, the hoop stress at the outside radius of the pipe, where strain gauges will measure strain, is:

$$\sigma_h(r_0) = \frac{Pr_i^2(r_o^2 + r_0^2)}{r^2(r_0^2 - r_i^2)} = \frac{2Pr_i^2}{(r_0^2 - r_i^2)} \qquad \text{Equation 2-20}$$

Substituting the formulas for longitudinal and hoop stress into Equation 2-18 yields the following equation for strain oscillation reading:

$$\epsilon_h = \frac{P}{E}\left(\frac{2r_i^2}{r_0^2 - r_i^2} - \frac{vr_i^2}{r_0^2 - r_i^2}\right) = \frac{P}{E}\left(\frac{(2-v)r_i^2}{r_0^2 - r_i^2}\right) \qquad \text{Equation 2-21}$$

Therefore, the pressure oscillations in the pipe can be calculated from the strain oscillation reading as follows:

$$P = \left(\frac{E\epsilon_h(r_0^2 - r_i^2)}{(2-\nu)r_i^2}\right)$$ Equation 2-22

The signal registered by the strain gauges is converted into pressure and its frequency content is computed. To determine magnitudes of interfering waves, a decomposition of the received signal is necessary to reconstruct the incident and reflected waves as a resultant wave with pressure *P(x)*. Wave attenuation/reflection effects are considered negligible in this arrangement due to the relatively short distance between the two stations.

From Reference B-12, the general wave solution for wave travelling in both directions inside a duct is given by:

$$P(x) = (Ae^{-jkx} + Be^{jkx})$$ Equation 2-23

In this instance, A and B are arbitrary complex magnitude of the sound wave traveling in the positive and negative direction of x. A and B can be calculated in terms of the pressure determined by the strain measurements at the two strain gauge station locations:

$$A = \frac{p_2 - p_1 e^{jk\triangle x}}{e^{-jk\triangle x} - e^{jk\triangle x}}$$ Equation 2-24

$$B = \frac{p_2 - p_1 e^{-jk\triangle x}}{e^{-jk\triangle x} - e^{jk\triangle x}}$$ Equation 2-25

where:

p_1 = sound pressure values determined by strain measurements at location 1

p_2 = sound pressure values determined by strain measurements at location 2

Δx = distance between strain gauge stations

k = wave number (number of wavelengths per unit distance or 1/λ)

x = location of wave decomposition

j = 1, 2, 3, …

B.3.3 Uncertainties and Bias Associated with the Acoustic Screening Criteria

For a robust screening approach, an evaluation of uncertainties and bias associated with the frequency of the cavity is performed. The uncertainties of parameters in the screening methodology provided in Section B.2.1.1 which are not included in the derivation of the Strouhal number analysis are:

- The acoustic frequency of the cavity
- The free stream velocity (U) of the flow in the main pipe, or the local velocity at the cavity entrance, which may be higher than the free stream velocity
- The diameter of the side branch (d)

The variability of the above three parameters must be considered when applying the empirical correlation of Equation 2-1 to ensure that a lower bound value of the Strouhal frequency is calculated with the screening acceptance criteria of S_{crit} = 0.63. The uncertainty evaluation provides additional safety margin

which confirms that acoustic resonance in the piping systems is avoided for a range of plant operating conditions.

B.3.3.1 Uncertainties and Bias Associated with the Acoustic Frequency of the Cavity

Equation 2-2 with N=1 provides the acoustic frequency for the first mode of vibration of the cavity with a narrow opening:

$$f = C/(4L) \qquad \text{Equation 2-26}$$

The above relationship indicates that the acoustic frequency is proportional to the speed of sound(C) in the moving fluid. The speed of sound is a function of the temperature, pressure, and quality of the pipe flow (dissolved material or entrained particulates). Uncertainties in the plant measurement of temperature and pressure in the piping system could lead to imprecise values for the density of the fluid, and thus misrepresent the actual speed of sound in the system. To conservatively obtain a lower-bound value for the speed of sound, the operating pressure and the design temperature of the piping system are used. This procedure eliminates uncertainties associated with the speed of sound.

The cavity length ' L ' in Equation 2-26 represents the physical length of the cavity; however, due to the natural mode of vibration, this length may be slightly shifted from elastic deformation. The acoustic frequency of the cavity can be conservatively determined by considering the effective depth of the cavity through the following formula:

$$L_{eff} = L + 0.3\ (d) \qquad \text{Equation 2–27}$$

Where:

d = diameter of the opening of the cavity

In the event that non-standard geometry (i.e., shapes that are different than standpipe or stub) is used for a closed branch or cavity, the effective length will be determined and the acoustic frequency will be assessed by detailed analysis.

B.3.3.2 Uncertainties and Bias Associated with the Free Stream Velocity

There are several factors that could result in a higher local velocity at the opening of the acoustic cavity than the free stream velocity in the main pipe. For instance, the elbows in the piping system lead to flow swirl and increase flow speed on the outer edge of the bend radius. If an acoustic cavity is located downstream and is in close proximity to the elbow, the local velocity of the flow over the opening of the cavity is higher than the free stream velocity in the main pipe, which creates a higher vortex shedding frequency than that predicted by using the free stream velocity. Another factor that affects the local velocity is the variation in the pipe internal diameter or cross-sectional flow area. In addition, the uncertainty associated with instruments that measure the temperature and pressure of the system influences the mean flow velocity. Uncertainty in the velocity computed from the mass flow rate is propagated due to uncertainty in estimating the fluid density as a function of temperature and pressure in the system.

To account for these uncertainties in the local velocity near the opening of the acoustic cavity, a 10 percent increase in the mass flow rate at full power, normal operating conditions, and transient conditions will be used to provide an upper bound limiting velocity for which the Mach number will be evaluated and then compared to the screening acceptance criteria.

B.3.3.3 Uncertainties and Bias Associated with the Branch Opening Diameter

As discussed earlier, the blend radius for the mouth of the cavity, if present, is also used to determine the effective value for the branch opening diameter. Hence, the uncertainty that arises for this physical parameter stems from the fabrication and installation procedures for the piping and control of pipe wall thickness. The tolerance values for welds and assembly of piping components are used to determine the lower-bound combination of (d+r), to result in a higher calculation for the vortex shedding frequency than would be predicted by using average values

B.3.4 Vibration Measurement

B.3.4.1 Instrument Types

The majority of piping vibration response occurs at frequencies lower than 10 Hz. Therefore, instrumentation capable of low-frequency measurements are required (Reference B-5).

Acceleration, velocity, and displacement can be measured with the use of accelerometers. Accelerometers measure absolute acceleration and therefore do not need to be tied back or attached to any plant structure. Accelerometers are, however, subject to noise caused by high accelerations at high frequencies, such as from sudden shocks caused by looseness in the accelerometer bracket; integration of these signals, moreover, can distort the results at low frequencies.

Hand held vibration measurement equipment is also useful as an indicator of piping vibration, in that the personnel using such equipment can identify the locations of high vibration by moving along the piping.

The lowest frequency computed for most piping system will be evaluated in the choice of vibration measurement equipment for the practical application.

B.3.4.2 Choice of Locations for Vibration Instrumentation

It is a design goal to prevent the formation of strong acoustic pressure pulsations, and one of the purposes for monitoring is to ensure that strong acoustic signals are not in fact created over the range of operating flow conditions being tested in the RG 1.68 (Reference B-2).

Mechanical vibration testing for system piping will be performed in accordance with ASME OM-S/G-2007, Part 3 and the piping systems are designated VMG-2 based on no past experience of problems with shell mode vibration for the piping in the piping systems, and because of a lack of any known source of high frequency pulsations necessary to excite the shell mode vibrations in these VMG 2 subsystems.

Preliminary locations selected for measurement of the RCS are shown in Figure B.3-1.

Because some of the resonance pulsations may be damped as the fluid moves through certain components or system features, such as heater tube bundles and fluid control valves in the feedwater system and through expansions and contractions in steam headers and piping distribution branches in the main steam system, the acoustic resonance detectors will be placed in piping that is relatively close to the steam generator, so that greatest probability exists to identify any pulsations that could affect the steam generator.

For the main steam system, a set of hoop strain gauges is planned for each of the four steam headers upstream of the MSIVs. Each pair of twin strain gauge sets (4 strain gauges each at two adjacent axial locations on a straight run of pipe) should be monitored for pressure pulsation. The strain gauge set will pick up any significant acoustic signals from the safety valve standpipes or other MS sources that could be passed to the steam generator. This location will also be sensitive to any significant acoustic signals that might have an effect on the MSIV integrity. One accelerometer is placed on each of the main steam

isolation valves to detect any vibrations of the valves.

For the feedwater system, a set of hoop strain gauges is planned in the feedwater headers between the regulating valves and the first downstream check valve for the economizer nozzles on each steam generator. This monitoring location would cover potential noise generated by the control valves and numerous standpipes in an area of high feedwater velocities. Also, this location would provide the most sensitivity to detect input acoustic signals that could be passed to the steam generators and to detect any acoustic signals which possibly could affect the integrity of the FW containment isolation.

Because the FW header to the economizer carries 90% of the flow to the steam generator and the FW header to the downcomer carries 10% and the velocities in the downcomer header are about half those of the economizer header, the goal is to put pressure pulsation instruments only in the economizer headers for both steam generators.

One accelerometer is placed on each of the four flow control valves (two for downcomer header flow control valves and two for economizer header flow control valves). These accelerometers will be able to detect any vibrations of the flow control valves.

The precise location of each strain gauge sets are flexible and should take into account the final construction with regard to practical locations for installation.

With regards to instrumenting the condensate system, accelerations at discreet locations in condensate system will be measured during start-up testing using hand-held vibration monitors. That can accomplish effective estimates of the severity of piping vibration.

B.3.5 Acceptance Criteria

The acceptance criteria that is appropriate to be applied for the piping system vibrational test program, particularly with regard to mechanical piping vibration, is identified in ASME-OM (Reference B-4) and depends, in part, on what VMG designation, as defined in ASME-OM, has been established for the piping being tested. As defined in ASME-OM, the measured dominant frequencies are compared to allowable velocities, which are determined by beam analysis for the boundary conditions and basic shape of a piping routing.

The structural vibration modes of small-branch piping are often excited by the structural vibrations of the header piping. Also, pressure pulsations in the header piping or vortex shedding at the branch connection can excite acoustic resonances in the branch piping.

Small bore piping will be evaluated using the methods and acceptance criteria of VMG 3. However, the VMG-3 methods involve being able to access the piping of interest to perform visual or hands on measurement checks, so the question remains on what to do if the pipes cannot be accessed.

Where vibrations cannot be determined to be acceptable using VMG 3 because of lack of accessibility, then the methods, devices and acceptance criteria of VMG 2 will be used.

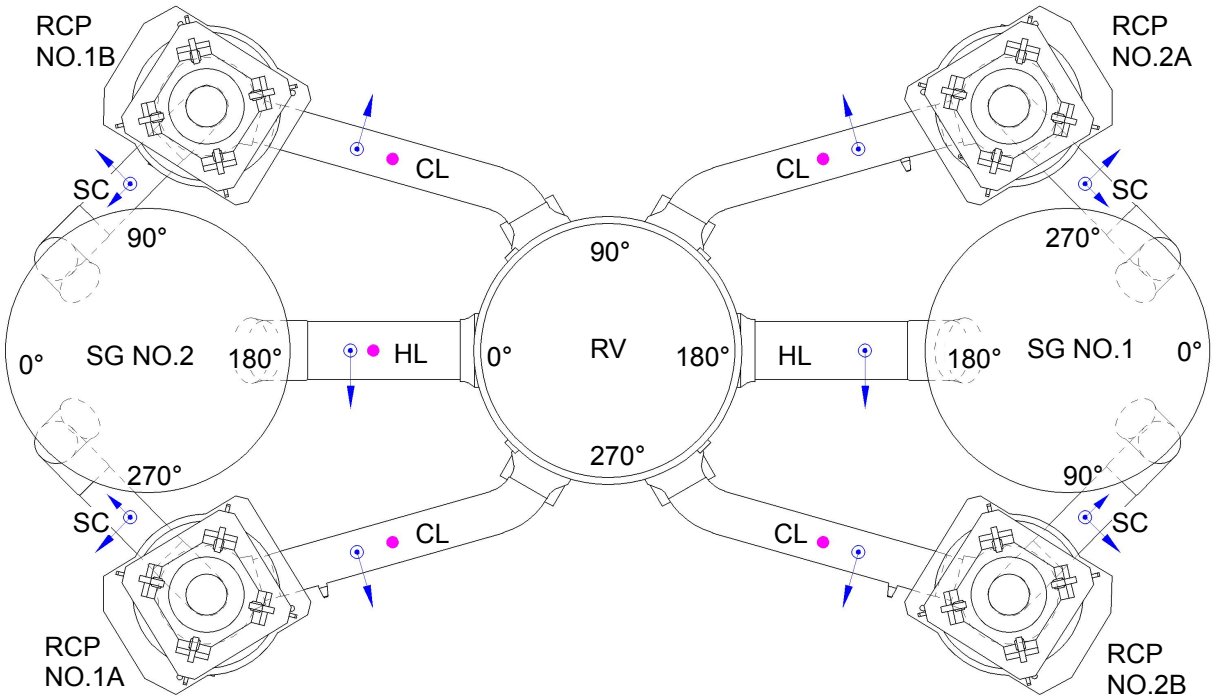

Note)
1. Legends.
   : Relative displacement loop/building (horizontal)
   : Relative displacement loop/building (vertical)
   : Pressure fluctuation
2. Abbreviations are as follows;
   RV : Reactor Vessel, SG : Steam Generator
   RCP : Reactor Coolant Pump, HL : Hot Leg Piping
   CL : Discharge Leg Piping, SC : Suction Leg Piping

Figure B.3-1 Locations of RCS Acoustic Instrumentation

B.4 REFERENCES

B-1. Regulatory Guide 1.20, "Comprehensive Vibration Assessment Program for Reactor Vessel Internals during Preoperational and Initial Startup Testing," Rev. 3, U.S. Nuclear Regulatory Commission, March 2007.

B-2. Regulatory Guide 1.68, "Initial Test Programs for Water Cooled Nuclear Power Plants," Rev.4, U.S. Nuclear Regulatory Commission, June 2013.

B-3. Standard Review Plan 3.9.2, "Dynamic Testing and Analysis of Systems, Structures and Components," Rev. 3, U.S. Nuclear Regulatory Commission, March 2007.

B-4. ASME OM S/G, “ASME Standards and Guides for Operation and Maintenance of Nuclear power Plants,” American Society of Mechanical Engineers, 2007.

B-5. Olson, David E., "Pipe Vibration, Testing and Analysis," Chapter 37 of Companion Guide to the ASME Boiler & Pressure Vessel Code, Vol. II 2nd Ed., 2006.

B-6. Baldwin, R.M. and Simmons, H.R., "Flow Induced Vibration in Safety Relief Valves," ASME Journal of Pressure Vessel Technology, Vol. 108, pp. 267-272, 1986.

B-7. Ziada, S. and Shine, S., "Strouhal Numbers of Flow Excited Acoustic Resonance of Closed Side Branches," Journal of Fluids and Structures, Vol. 13, pp. 127-142, 1999.

B-8. Wachel J. C. and Smith D. R., "Vibration Troubleshooting of Existing Piping Systems", Engineering Dynamics Incorporated, 1991.

B-9. Harris, C. M. and Piersol, A. G., "Harris' Shock and Vibration Handbook," 5th Edition, McGraw Hill, New York, 2002.

B-10. Pedrosa, A. M., Denia, F. D., Fuenmayor, F. J. and Abom, M., "Experimental Determination of Acoustic Properties by a Two Source Method with Simultaneous Excitation," 18th International Congress on Sound and Vibration, July, 2011.

B-11. Young, W. C., "Roark"s Formula for Stress and Strain," 7th Edition, McGraw Hill, Inc., New York, 2002.

B-12. Norambueno, M., Jakob, A., Moser, M., "A Wave Decomposition Method for the Active Control of Sound Absorption: Theory and First Experimental Results," Institut fur Stromungsmechanik und Technische Akustik, T U Berlin, DAGA, 2007.

B-13. Endevco, "Minimizing Measurement Uncertainty in Calibration and Use of Accelerometers," Tecnical Paper 299, URL :< https://www.endevco.com/news/archivednews/2010/2010_01/TP-299.pdf>, 2010.

B-14. IEC Standard 534-8-3, "Aerodynamic Noise Prediction Standard", 1995.

B-15. Singleton, E.W., ”Understanding IEC 534-8-3 in Control Valve Aerodynamic Noise Prediction”.

B-16. Wachel, J.C., Morton, S., Atkins, K., "Piping Vibration Analysis", Proceedings of the Nineteenth Turbomachinery Symposium, 1990.

B-17. Lighthill, M.J., "On Sound Generated Aerodynamically", The Royal Society, London, 1952.

B-18. Fox, J.A., "Hydraulic Analysis of Unsteady Flow in Pipe Networks", Halstead Press, John Wiley & Sons, 1977.